EUROPEAN ORGANIZATION FOR NUCLEAR RESEARCH

CERN–PH-EP/2007-026

12 July 2007

Measurement of the Mass and Width of the W Boson in e^+e^- Collisions at $\sqrt{s} = 161 - 209$ GeV

DELPHI Collaboration

Abstract

A measurement of the W boson mass and width has been performed by the DELPHI collaboration using the data collected during the full LEP2 programme (1996-2000). The data sample has an integrated luminosity of 660 pb^{-1} and was collected over a range of centre-of-mass energies from 161 to 209 GeV. Results are obtained by applying the method of direct reconstruction of the mass of the W from its decay products in both the $\mathrm{W^+W^-} \rightarrow \ell\overline{\nu}_\ell \mathrm{q\bar{q}'}$ and $\mathrm{W^+W^-} \rightarrow \mathrm{q\bar{q}'\bar{q}q'}$ channels. The W mass result for the combined data set is

$$\mathrm{M_W} \;=\; 80.336 \pm 0.055(\mathrm{Stat.}) \pm 0.028(\mathrm{Syst.}) \pm 0.025(\mathrm{FSI}) \pm 0.009(\mathrm{LEP})\ \mathrm{GeV}/c^2,$$

where FSI represents the uncertainty due to final state interaction effects in the $\mathrm{q\bar{q}'\bar{q}q'}$ channel, and LEP represents that arising from the knowledge of the collision energy of the accelerator. The combined value for the W width is

$$\Gamma_\mathrm{W} \;=\; 2.404 \pm 0.140(\mathrm{Stat.}) \pm 0.077(\mathrm{Syst.}) \pm 0.065(\mathrm{FSI})\ \mathrm{GeV}/c^2.$$

These results supersede all values previously published by the DELPHI collaboration.

This paper is dedicated to the memory of Carlo Caso.

(Accepted by Eur. Phys. J. C)

J.Abdallah[26], P.Abreu[23], W.Adam[55], P.Adzic[12], T.Albrecht[18], R.Alemany-Fernandez[9], T.Allmendinger[18], P.P.Allport[24], U.Amaldi[30], N.Amapane[48], S.Amato[52], E.Anashkin[37], A.Andreazza[29], S.Andringa[23], N.Anjos[23], P.Antilogus[26], W-D.Apel[18], Y.Arnoud[15], S.Ask[9], B.Asman[47], J.E.Augustin[26], A.Augustinus[9], P.Baillon[9], A.Ballestrero[49], P.Bambade[21], R.Barbier[28], D.Bardin[17], G.J.Barker[57], A.Baroncelli[40], M.Battaglia[9], M.Baubillier[26], K-H.Becks[58], M.Begalli[7], A.Behrmann[58], E.Ben-Haim[21], N.Benekos[33], A.Benvenuti[5], C.Berat[15], M.Berggren[26], D.Bertrand[2], M.Besancon[41], N.Besson[41], D.Bloch[10], M.Blom[32], M.Bluj[56], M.Bonesini[30], M.Boonekamp[41], P.S.L.Booth[†24], G.Borisov[22], O.Botner[53], B.Bouquet[21], T.J.V.Bowcock[24], I.Boyko[17], M.Bracko[44], R.Brenner[53], E.Brodet[36], P.Bruckman[19], J.M.Brunet[8], B.Buschbeck[55], P.Buschmann[58], M.Calvi[30], T.Camporesi[9], V.Canale[39], F.Carena[9], N.Castro[23], F.Cavallo[5], M.Chapkin[43], Ph.Charpentier[9], P.Checchia[37], R.Chierici[9], P.Chliapnikov[43], J.Chudoba[9], S.U.Chung[9], K.Cieslik[19], P.Collins[9], R.Contri[14], G.Cosme[21], F.Cossutti[50], M.J.Costa[54], D.Crennell[38], J.Cuevas[35], J.D'Hondt[2], T.da Silva[52], W.Da Silva[26], G.Della Ricca[50], A.De Angelis[51], W.De Boer[18], C.De Clercq[2], B.De Lotto[51], N.De Maria[48], A.De Min[37], L.de Paula[52], L.Di Ciaccio[39], A.Di Simone[40], K.Doroba[56], J.Drees[58,9], A.Duperrin[28], G.Eigen[4], T.Ekelof[53], M.Ellert[53], M.Elsing[9], M.C.Espirito Santo[23], G.Fanourakis[12], D.Fassouliotis[12,3], M.Feindt[18], J.Fernandez[42], A.Ferrer[54], F.Ferro[14], U.Flagmeyer[58], H.Foeth[9], E.Fokitis[33], F.Fulda-Quenzer[21], J.Fuster[54], M.Gandelman[52], C.Garcia[54], Ph.Gavillet[9], E.Gazis[33], R.Gokieli[9,56], B.Golob[44,46], G.Gomez-Ceballos[42], P.Goncalves[23], E.Graziani[40], G.Grosdidier[21], K.Grzelak[56], J.Guy[38], C.Haag[18], A.Hallgren[53], K.Hamacher[58], K.Hamilton[36], S.Haug[34], F.Hauler[18], V.Hedberg[27], M.Hennecke[18], J.Hoffman[56], S-O.Holmgren[47], P.J.Holt[9], M.A.Houlden[24], J.N.Jackson[24], G.Jarlskog[27], P.Jarry[41], D.Jeans[36], E.K.Johansson[47], P.Jonsson[28], C.Joram[9], L.Jungermann[18], F.Kapusta[26], S.Katsanevas[28], E.Katsoufis[33], G.Kernel[44], B.P.Kersevan[44,46], U.Kerzel[18], B.T.King[24], N.J.Kjaer[9], P.Kluit[32], P.Kokkinias[12], C.Kourkoumelis[3], O.Kouznetsov[17], Z.Krumstein[17], M.Kucharczyk[19], J.Lamsa[1], G.Leder[55], F.Ledroit[15], L.Leinonen[47], R.Leitner[31], J.Lemonne[2], V.Lepeltier[21], T.Lesiak[19], W.Liebig[58], D.Liko[55], A.Lipniacka[47], J.H.Lopes[52], J.M.Lopez[35], D.Loukas[12], P.Lutz[41], L.Lyons[36], J.MacNaughton[55], A.Malek[58], S.Maltezos[33], F.Mandl[55], J.Marco[42], R.Marco[42], B.Marechal[52], M.Margoni[37], J-C.Marin[9], C.Mariotti[9], A.Markou[12], C.Martinez-Rivero[42], J.Masik[13], N.Mastroyiannopoulos[12], F.Matorras[42], C.Matteuzzi[30], F.Mazzucato[37], M.Mazzucato[37], R.Mc Nulty[24], C.Meroni[29], E.Migliore[48], W.Mitaroff[55], U.Mjoernmark[27], T.Moa[47], M.Moch[18], K.Moenig[9,11], R.Monge[14], J.Montenegro[32], D.Moraes[52], S.Moreno[23], P.Morettini[14], U.Mueller[58], K.Muenich[58], M.Mulders[32], L.Mundim[7], W.Murray[38], B.Muryn[20], G.Myatt[36], T.Myklebust[34], M.Nassiakou[12], F.Navarria[5], K.Nawrocki[56], R.Nicolaidou[41], M.Nikolenko[17,10], A.Oblakowska-Mucha[20], V.Obraztsov[43], A.Olshevski[17], A.Onofre[23], R.Orava[16], K.Osterberg[16], A.Ouraou[41], A.Oyanguren[54], M.Paganoni[30], S.Paiano[5], J.P.Palacios[24], H.Palka[19], Th.D.Papadopoulou[33], L.Pape[9], C.Parkes[25], F.Parodi[14], U.Parzefall[9], A.Passeri[40], O.Passon[58], L.Peralta[23], V.Perepelitsa[54], A.Perrotta[5], A.Petrolini[14], J.Piedra[42], L.Pieri[40], F.Pierre[41], M.Pimenta[23], E.Piotto[9], T.Podobnik[44,46], V.Poireau[9], M.E.Pol[6], G.Polok[19], V.Pozdniakov[17], N.Pukhaeva[17], A.Pullia[30], D.Radojicic[36], J.Rames[13], A.Read[34], P.Rebecchi[9], J.Rehn[18], D.Reid[32], R.Reinhardt[58], P.Renton[36], F.Richard[21], J.Ridky[13], M.Rivero[42], D.Rodriguez[42], A.Romero[48], P.Ronchese[37], P.Roudeau[21], T.Rovelli[5], V.Ruhlmann-Kleider[41], D.Ryabtchikov[43], A.Sadovsky[17], L.Salmi[16], J.Salt[54], C.Sander[18], A.Savoy-Navarro[26], U.Schwickerath[9], R.Sekulin[38], M.Siebel[58], L.Simard[41], A.Sisakian[17], G.Smadja[28], O.Smirnova[27], A.Sokolov[43], A.Sopczak[22], R.Sosnowski[56], T.Spassov[9], M.Stanitzki[18], A.Stocchi[21], J.Strauss[55], B.Stugu[4], M.Szczekowski[56], M.Szeptycka[56], T.Szumlak[20], T.Tabarelli[30], F.Tegenfeldt[53], J.Thomas[36], J.Timmermans[32], L.Tkatchev[17], M.Tobin[24], S.Todorovova[13], B.Tome[23], A.Tonazzo[30], P.Tortosa[54], P.Travnicek[13], D.Treille[9], G.Tristram[8], M.Trochimczuk[56], C.Troncon[29], M-L.Turluer[41], I.A.Tyapkin[17], P.Tyapkin[17], S.Tzamarias[12], V.Uvarov[43], G.Valenti[5], P.Van Dam[32], J.Van Eldik[9], N.van Remortel[16], I.Van Vulpen[9], G.Vegni[29], F.Veloso[23], W.Venus[38], P.Verdier[28], V.Verzi[39], D.Vilanova[41], L.Vitale[50], V.Vrba[13], H.Wahlen[58], A.J.Washbrook[24], C.Weiser[18], D.Wicke[9], J.Wickens[2], G.Wilkinson[36], M.Winter[10], M.Witek[19], O.Yushchenko[43], A.Zalewska[19], P.Zalewski[56], D.Zavrtanik[45], V.Zhuravlov[17], N.I.Zimin[17], A.Zintchenko[17], M.Zupan[12]

[1]Department of Physics and Astronomy, Iowa State University, Ames IA 50011-3160, USA
[2]IIHE, ULB-VUB, Pleinlaan 2, B-1050 Brussels, Belgium
[3]Physics Laboratory, University of Athens, Solonos Str. 104, GR-10680 Athens, Greece
[4]Department of Physics, University of Bergen, Allégaten 55, NO-5007 Bergen, Norway
[5]Dipartimento di Fisica, Università di Bologna and INFN, Via Irnerio 46, IT-40126 Bologna, Italy
[6]Centro Brasileiro de Pesquisas Físicas, rua Xavier Sigaud 150, BR-22290 Rio de Janeiro, Brazil
[7]Inst. de Física, Univ. Estadual do Rio de Janeiro, rua São Francisco Xavier 524, Rio de Janeiro, Brazil
[8]Collège de France, Lab. de Physique Corpusculaire, IN2P3-CNRS, FR-75231 Paris Cedex 05, France
[9]CERN, CH-1211 Geneva 23, Switzerland
[10]Institut de Recherches Subatomiques, IN2P3 - CNRS/ULP - BP20, FR-67037 Strasbourg Cedex, France
[11]Now at DESY-Zeuthen, Platanenallee 6, D-15735 Zeuthen, Germany
[12]Institute of Nuclear Physics, N.C.S.R. Demokritos, P.O. Box 60228, GR-15310 Athens, Greece
[13]FZU, Inst. of Phys. of the C.A.S. High Energy Physics Division, Na Slovance 2, CZ-182 21, Praha 8, Czech Republic
[14]Dipartimento di Fisica, Università di Genova and INFN, Via Dodecaneso 33, IT-16146 Genova, Italy
[15]Institut des Sciences Nucléaires, IN2P3-CNRS, Université de Grenoble 1, FR-38026 Grenoble Cedex, France
[16]Helsinki Institute of Physics and Department of Physical Sciences, P.O. Box 64, FIN-00014 University of Helsinki, Finland
[17]Joint Institute for Nuclear Research, Dubna, Head Post Office, P.O. Box 79, RU-101 000 Moscow, Russian Federation
[18]Institut für Experimentelle Kernphysik, Universität Karlsruhe, Postfach 6980, DE-76128 Karlsruhe, Germany
[19]Institute of Nuclear Physics PAN,Ul. Radzikowskiego 152, PL-31142 Krakow, Poland
[20]Faculty of Physics and Nuclear Techniques, University of Mining and Metallurgy, PL-30055 Krakow, Poland
[21]Université de Paris-Sud, Lab. de l'Accélérateur Linéaire, IN2P3-CNRS, Bât. 200, FR-91405 Orsay Cedex, France
[22]School of Physics and Chemistry, University of Lancaster, Lancaster LA1 4YB, UK
[23]LIP, IST, FCUL - Av. Elias Garcia, 14-1^o, PT-1000 Lisboa Codex, Portugal
[24]Department of Physics, University of Liverpool, P.O. Box 147, Liverpool L69 3BX, UK
[25]Dept. of Physics and Astronomy, Kelvin Building, University of Glasgow, Glasgow G12 8QQ, UK
[26]LPNHE, IN2P3-CNRS, Univ. Paris VI et VII, Tour 33 (RdC), 4 place Jussieu, FR-75252 Paris Cedex 05, France
[27]Department of Physics, University of Lund, Sölvegatan 14, SE-223 63 Lund, Sweden
[28]Université Claude Bernard de Lyon, IPNL, IN2P3-CNRS, FR-69622 Villeurbanne Cedex, France
[29]Dipartimento di Fisica, Università di Milano and INFN-MILANO, Via Celoria 16, IT-20133 Milan, Italy
[30]Dipartimento di Fisica, Univ. di Milano-Bicocca and INFN-MILANO, Piazza della Scienza 3, IT-20126 Milan, Italy
[31]IPNP of MFF, Charles Univ., Areal MFF, V Holesovickach 2, CZ-180 00, Praha 8, Czech Republic
[32]NIKHEF, Postbus 41882, NL-1009 DB Amsterdam, The Netherlands
[33]National Technical University, Physics Department, Zografou Campus, GR-15773 Athens, Greece
[34]Physics Department, University of Oslo, Blindern, NO-0316 Oslo, Norway
[35]Dpto. Fisica, Univ. Oviedo, Avda. Calvo Sotelo s/n, ES-33007 Oviedo, Spain
[36]Department of Physics, University of Oxford, Keble Road, Oxford OX1 3RH, UK
[37]Dipartimento di Fisica, Università di Padova and INFN, Via Marzolo 8, IT-35131 Padua, Italy
[38]Rutherford Appleton Laboratory, Chilton, Didcot OX11 OQX, UK
[39]Dipartimento di Fisica, Università di Roma II and INFN, Tor Vergata, IT-00173 Rome, Italy
[40]Dipartimento di Fisica, Università di Roma III and INFN, Via della Vasca Navale 84, IT-00146 Rome, Italy
[41]DAPNIA/Service de Physique des Particules, CEA-Saclay, FR-91191 Gif-sur-Yvette Cedex, France
[42]Instituto de Fisica de Cantabria (CSIC-UC), Avda. los Castros s/n, ES-39006 Santander, Spain
[43]Inst. for High Energy Physics, Serpukov P.O. Box 35, Protvino, (Moscow Region), Russian Federation
[44]J. Stefan Institute, Jamova 39, SI-1000 Ljubljana, Slovenia
[45]Laboratory for Astroparticle Physics, University of Nova Gorica, Kostanjeviska 16a, SI-5000 Nova Gorica, Slovenia
[46]Department of Physics, University of Ljubljana, SI-1000 Ljubljana, Slovenia
[47]Fysikum, Stockholm University, Box 6730, SE-113 85 Stockholm, Sweden
[48]Dipartimento di Fisica Sperimentale, Università di Torino and INFN, Via P. Giuria 1, IT-10125 Turin, Italy
[49]INFN,Sezione di Torino and Dipartimento di Fisica Teorica, Università di Torino, Via Giuria 1, IT-10125 Turin, Italy
[50]Dipartimento di Fisica, Università di Trieste and INFN, Via A. Valerio 2, IT-34127 Trieste, Italy
[51]Istituto di Fisica, Università di Udine and INFN, IT-33100 Udine, Italy
[52]Univ. Federal do Rio de Janeiro, C.P. 68528 Cidade Univ., Ilha do Fundão BR-21945-970 Rio de Janeiro, Brazil
[53]Department of Radiation Sciences, University of Uppsala, P.O. Box 535, SE-751 21 Uppsala, Sweden
[54]IFIC, Valencia-CSIC, and D.F.A.M.N., U. de Valencia, Avda. Dr. Moliner 50, ES-46100 Burjassot (Valencia), Spain
[55]Institut für Hochenergiephysik, Österr. Akad. d. Wissensch., Nikolsdorfergasse 18, AT-1050 Vienna, Austria
[56]Inst. Nuclear Studies and University of Warsaw, Ul. Hoza 69, PL-00681 Warsaw, Poland
[57]Now at University of Warwick, Coventry CV4 7AL, UK
[58]Fachbereich Physik, University of Wuppertal, Postfach 100 127, DE-42097 Wuppertal, Germany
[†] deceased

1 Introduction

The measurement of the W boson mass can be used, in combination with other electroweak data, to test the validity of the Standard Model and obtain estimates of its fundamental parameters. In particular the measurement is sensitive, through loop corrections, to the masses of the top quark and the Higgs boson.

The W boson mass and width results presented in this paper are obtained from data recorded by the DELPHI experiment during the 1996-2000 operation of the LEP Collider, known as the LEP2 period. This corresponds to a total of 660 pb^{-1} collected over a range of centre-of-mass energies: $\sqrt{s} = 161 - 209$ GeV.

Initially, data were recorded close to the $\mathrm{W}^+\mathrm{W}^-$ pair production threshold. At this energy the $\mathrm{W}^+\mathrm{W}^-$ cross-section is sensitive to the W boson mass, $\mathrm{M_W}$. Subsequently, LEP operated at higher centre-of-mass energies, where the $e^+e^- \rightarrow \mathrm{W}^+\mathrm{W}^-$ cross-section has little sensitivity to $\mathrm{M_W}$. For these data, which constitute the bulk of the DELPHI data sample, $\mathrm{M_W}$ and the W boson width, Γ_W, are measured through the direct reconstruction of the W boson's invariant mass from the observed jets and leptons. The analysis is performed on the final states in which both W bosons in the event decay hadronically ($\mathrm{W}^+\mathrm{W}^- \rightarrow \mathrm{q\bar{q}'\bar{q}q'}$ or fully-hadronic) and in which one W boson decays hadronically while the other decays leptonically ($\mathrm{W}^+\mathrm{W}^- \rightarrow \ell\overline{\nu}_\ell \mathrm{q\bar{q}'}$ or semi-leptonic).

The $\mathrm{M_W}$ analyses of the relatively small quantity of data ($\sim 20\ \mathrm{pb}^{-1}$) collected during 1996 at centre-of-mass energies of 161 and 172 GeV were published in [1,2]. These data are not reanalysed in this paper but are discussed in sections 7.1.1 and 7.1.2 and included in the final $\mathrm{M_W}$ combination.

The data recorded during 1997 and 1998 at $\sqrt{s} = 183$ and 189 GeV have also been the subject of previous DELPHI publications [3,4]. These data have been reprocessed and are reanalysed in this paper; the results given here supersede those in the previous publications. Results on the data collected during the final two years of LEP operation are published here for the first time. The data quality, simulation samples and analysis techniques have all been improved with respect to those used in previous DELPHI publications. The W mass and width have also been determined by the other LEP collaborations [5] and at hadron colliders [6].

The results on the W mass, $\mathrm{M_W}$, and width, Γ_W, presented below correspond to a definition based on a Breit-Wigner denominator with an s-dependent width, $|(s - \mathrm{M_W}^2) + is\Gamma_\mathrm{W}/\mathrm{M_W}|$.

After these introductory remarks, the paper starts in section 2 by describing the LEP accelerator and the determination of its collison energy. A brief description of the DELPHI detector is provided as section 3. This is followed by section 4 which presents the properties of the data sample and of the Monte Carlo simulation samples used in the analysis.

The analysis method is presented in section 5, first for $\mathrm{W}^+\mathrm{W}^- \rightarrow \ell\overline{\nu}_\ell \mathrm{q\bar{q}'}$ events, then for $\mathrm{W}^+\mathrm{W}^- \rightarrow \mathrm{q\bar{q}'\bar{q}q'}$ events. The text describes how the events are selected and the mass and width estimated from $\mathrm{M_W}$- and Γ_W-dependent likelihood functions. The potential sources of systematic uncertainty are considered in section 6. These include: inaccuracies in the modelling of the detector; uncertainties on the background; uncertainties on the effects of radiative corrections; understanding of the hadronisation of the W boson jets; possible cross-talk between two hadronically decaying W bosons, the effects of which the $\mathrm{q\bar{q}'\bar{q}q'}$ $\mathrm{M_W}$ analysis has been specifically designed to minimise; and uncertainty on the LEP centre-of-mass energy determination. The paper concludes in section 7 with a presentation of the results and their combination.

2 LEP Characteristics

2.1 Accelerator Operation

The LEP2 programme began in 1996 when the collision energy of the beams was first ramped to the W^+W^- production threshold of 161 GeV and approximately 10 pb^{-1} of integrated luminosity was collected by each experiment. Later in that year LEP was run at 172 GeV and a dataset of similar size was accumulated. In each of the four subsequent years of operation the collision energy was raised to successively higher values, and the accelerator performance improved such that almost half the integrated luminosity was delivered at nominal collision energies of 200 GeV and above. The main motivation for this programme was to improve the sensitivity of the search for the Higgs boson and other new particles. The step-by-step nature of the energy increase was dictated by the evolving capabilities of the radio frequency (RF) accelerating system.

During normal operation the machine would be filled with 4 electron and 4 positron bunches at $E_{beam} \approx 22$ GeV, and the beams then ramped to physics energy, at which point they would be steered into collision and experimental data taking begun. The *fill* would last until the beam currents fell below a useful level, or an RF cavity trip precipitated loss of beam. The mean fill lengths ranged from 5 hours in 1996 to 2 hours in 1999. After de-Gaussing the magnets the cycle would be repeated.

In 2000, the operation was modified in order to optimise still further the high energy reach of LEP. Fills were started at a beam energy safely within the capabilities of the RF system. When the beam currents had decayed significantly, typically after an hour, the dipoles were ramped and luminosity delivered at a higher energy. This procedure was repeated until the energy was at the limit of the RF, and data taken until the beam was lost through a klystron trip. These *mini-ramps* lasted less than a minute, and varied in step size with a mean value of 600 MeV. The luminosity in 2000 therefore was delivered through a near-continuum of collision energies between 201 and 209 GeV.

In addition to the high energy running, a number of fills each year were performed at the Z resonance. This was to provide calibration data for the experiments. Finally, several fills were devoted to energy calibration activities, most notably resonant depolarisation (RDP), spectrometer and Q_s measurements (see below for further details).

The machine optics which were used for physics operation and for RDP measurements evolved throughout the programme in order to optimise the luminosity at each energy point. Certain optics enhanced the build-up of polarisation, and thus were favoured for RDP measurements. The optics influence E_{beam} in several ways, and are accounted for in the energy model, full details of which are available in [7].

2.2 The LEP Energy Model

A precise measurement of the LEP beam energy, and thus the centre-of-mass energy, is a crucial ingredient in the determination of the W mass as it sets the overall energy scale. The absolute energy scale of LEP is set by the technique of RDP, which is accurate to better than 1 MeV. This technique allowed very precise measurements of the mass and width of the Z boson to be made at LEP1. However, this technique is only possible for beam energies between about 41 and 61 GeV. The LEP2 energy scale is set mainly by the nuclear magnetic resonance (NMR) model. This makes use of 16 NMR probes, positioned in selected dipoles, which were used to obtain local measurements of the bending field. These probes thus sample the total bending field, which is the primary component in determining the beam energy. Onto this must be added time-dependent corrections coming from other sources. These include effects from earth tides, beam orbit corrections, changes in the RF frequency, and other smaller effects. Details of all these can be found in [7]. Using this LEP Energy Model, the LEP Energy group provided DELPHI with an estimate of the centre-of-mass energy at the start of each fill and thereafter in intervals of 15 minutes. For the year 2000 the values before and after the mini-ramps were also supplied. No data are used which are taken during the mini-ramps, as the energy is not accurately known during these periods.

The main assumption which is made in the LEP Energy Model is that the beam energy scales linearly with the readings of the NMR probes. This assumption of linearity has been tested by three different methods:

1) *Flux Loop.* Each dipole magnet of LEP is equipped with a single-turn flux loop. Measurements are made for a series of dipole magnet currents, which correspond roughly to the operating beam energies of LEP2. This allows the change in flux over almost the entire LEP dipole field to be measured as the machine is ramped in dedicated experiments. This change in flux can be compared with the local bending field measurements of the NMR probes. The Flux Loop is calibrated against the LEP energy model in the range 41-61 GeV, using the NMR coefficients determined from RDP. The measurements from the Flux Loop in the high energy regime (up to 106 GeV beam energy) are then compared to those from the LEP Energy Model. The Flux Loop measurements were made in all years of LEP2 running.

2) *Spectrometer Magnet.* In 1999 a special steel Spectrometer Magnet, equipped with three beam position monitors to measure the beam position both on entry and exit from the magnet, was installed in the LEP ring. The magnetic field of this magnet was carefully mapped before and after installation in the LEP ring. All these measurements were very compatible. The beam energy is determined by measuring the bending angle of the beam in passing through the dipole magnet. The device was calibrated against RDP in the 41-61 GeV region and the Spectrometer results were compared to the LEP Energy Model at beam energies of 70 and 92 GeV.

3) *Q_s versus V_{RF}.* The synchrotron tune Q_s can be expressed as a function of the beam energy and the total RF voltage, V_{RF}, plus some additional small corrections. By measuring Q_s as a function of the total RF voltage the beam energy can be determined. These measurements were performed in 1998-2000, at beam energies from 80 to 91 GeV. Again the measurements were normalised against RDP in the region 41-61 GeV, and compared to the LEP Energy Model at LEP2 energies.

The three methods are in good agreement, both with each other and the LEP Energy Model. Based on these comparisons a small energy offset compared to the LEP Energy Model was supplied for each of the 10 beam energies used in LEP2. This offset is always smaller than 2 MeV. The estimated centre-of-mass energy uncertainties range between 20 and 40 MeV and are discussed further in section 6.8 .

The LEP centre-of-mass energy has also been determined by the LEP collaborations using LEP2 events containing on-shell Z bosons and photons (radiative return to the Z events) [8,9]. The DELPHI analysis measured the average difference between the centre-of-mass energy from radiative return events in the $e^+e^-\to\mu^+\mu^-(\gamma)$ and $e^+e^-\to q\bar{q}(\gamma)$ channels and the energy reported by the LEP Energy working group,

$$\Delta E_{cm} \;=\; +0.073 \pm 0.094(Stat.) \pm 0.065(Syst.)\ \mathrm{GeV}.$$

Thus the DELPHI result, relying on similar reconstruction procedures to those described in this paper, is in agreement with the values reported by the LEP Energy working group.

3 Detector Description

The DELPHI detector [10] was upgraded for LEP2. Changes were made to the subdetectors, the trigger system, the run control and the algorithms used in the offline reconstruction of tracks, which improved the performance compared to the earlier LEP1 period.

The major change was the inclusion of the Very Forward Tracker (VFT) [11], which extended the coverage of the innermost silicon tracker out to $11° < \theta < 169°$[1]. Together with improved tracking algorithms and alignment and calibration procedures optimised for LEP2, these changes led to an improved track reconstruction efficiency in the forward regions of DELPHI.

Changes were made to the electronics of the trigger and timing system which improved the stability of the running during data taking. The trigger conditions were optimised for LEP2 running, to give high efficiency for Standard Model two- and four-fermion processes and also to give sensitivity for events which may be signatures of new physics. In addition, improvements were made to the operation of the detector during the LEP cycle, to prepare the detector for data taking at the very start of stable collisions of the e^+e^- beams, and to respond to adverse background from LEP were they to arise. These changes led to an overall improvement of $\sim 10\%$ in the efficiency for collecting the delivered luminosity from $\sim 85\%$ in 1995, before the start of LEP2, to $\sim 95\%$ at the end in 2000.

During the operation of the DELPHI detector in 2000 one of the 12 sectors of the central tracking chamber, the TPC, failed. After the 1st September 2000 it was not possible to detect the tracks left by charged particles inside the broken sector. The data affected correspond to $\sim 1/4$ of the total dataset of the year 2000. Nevertheless, the redundancy of the tracking system of DELPHI meant that tracks passing through the sector could still be reconstructed from signals in any of the other tracking detectors. A modified track reconstruction algorithm was used in this sector, which included space points reconstructed in the Barrel RICH detector. As a result, the track reconstruction efficiency was only slightly reduced in the region covered by the broken sector, but the track parameter resolutions were degraded compared with the data taken prior to the failure of this sector.

4 Data and Simulation Samples

4.1 Data

The W mass and width are measured in this paper with the data samples collected during the 1996-2000 operation of the LEP Collider. A summary of the available data samples is reported in table 1, where the luminosity-weighted centre-of-mass energies and the amount of data collected at each energy are shown. The luminosity is determined from Bhabha scattering measurements making use of the very forward electromagnetic calorimetry [12]. The total integrated luminosity for the LEP2 period corresponds to

[1] The DELPHI coordinate system is right-handed with the z-axis collinear with the incoming electron beam, and the x axis pointing to the centre of the LEP accelerator. The radius in the xy plane is denoted R and θ is used to represent the polar angle to the z axis.

approximately 660 pb^{-1}. The integrated luminosities used for the different selections correspond to those data for which all elements of the detector essential to each specific analysis were fully functional. The additional requirements on, for example, the status of the calorimetry and the muon chambers mean that the integrated luminosity of the semi-leptonic analysis is slightly less that that of the hadronic dataset.

All the data taken from the year 1997 onwards have been reprocessed with an improved reconstruction code, and the analyses on these data are updated with respect to the previously published ones and supersede them. The data taken in 1996 have not been reanalysed; the results from this year are taken from the previous publications with minor revisions as reported in section 7.

In addition to these data taken above the $\mathrm{W}^+\mathrm{W}^-$-pair production threshold, data were also recorded during this period at the Z peak. These samples, containing a total of over 0.5 million collected Z decays, were taken each year typically at the start and end of the data taking periods. These Z peak samples were used extensively in the alignment and calibration of the detector and are used in many of the systematic uncertainty studies reported in section 6.

Year	$\mathcal{L}$-weighted $\sqrt{s}$ (GeV)	Hadronic Int. $\mathcal{L}$ (pb^{-1})	Leptonic Int. $\mathcal{L}$ (pb^{-1})
1996	161.31	10.1	10.1
	172.14	10.1	10.1
1997	182.65	52.5	51.8
1998	188.63	154.4	152.5
1999	191.58	25.2	24.4
	195.51	76.1	74.6
	199.51	82.8	81.6
	201.64	40.3	40.2
2000	205.86	218.4	215.9

Table 1: Luminosity-weighted centre-of-mass energies and integrated luminosities in the LEP2 data taking period. The hadronic integrated luminosity is used for the fully-hadronic channel, the leptonic one is used for the semi-leptonic channels.

4.2 Simulation

The response of the detector to various physical processes was described using the simulation program `DELSIM` [10], which includes modelling of the resolution, granularity and efficiency of the detector components. In addition, detector correction factors, described in section 6, were included to improve the description of jets, electrons and muons. To allow use of the data taken after the 1st September in 2000, samples of events were simulated dropping information from the broken sector of the TPC. A variety of event generators were used to describe all the physics processes relevant for the analysis. $\mathrm{W}^+\mathrm{W}^-$ events and all other four-fermion processes were simulated with the program described in [13], based on the `WPHACT` 2.0 generator [14] interfaced with `PYTHIA` 6.156 [15] to describe quark hadronisation and `TAUOLA` 2.6 [16] to model τ leptons decays. The most recent $\mathcal{O}(\alpha)$ electroweak radiative corrections in the so-called Double Pole Approximation (DPA) were included in the generation of the signal via weights computed by `YFSWW` 3.1.16 [17], and the treatment of initial state radiation (ISR) of this calculation was adopted. The photon radiation from final state leptons was computed with `PHOTOS` 2.5 [18]. For systematic studies the alternative hadronisation descriptions implemented in `ARIADNE` 4.08 [19] and `HERWIG` 6.2 [20] were also used. All the hadronisation models were tuned on the DELPHI Z peak data [21].

The background process $e^+e^- \to q\bar{q}(\gamma)$ was simulated with `KK` 4.14 [22] interfaced with `PYTHIA` 6.156 for the hadronisation description. The two-photon events giving rise to those $e^+e^-q\bar{q}$ final states not described in the four-fermion generation above were produced with `PYTHIA` 6.143 as discussed in [13]. The contribution from all other background processes was negligible.

The simulated integrated luminosity used for the analysis was about a factor 350 higher than for the real data collected for 4-fermion processes, about a factor 60 higher for 2-fermion final states and about 3.5 times greater for $e^+e^-q\bar{q}$ two-photon final states (those not already included in the 4-fermion simulation).

5 Analysis Method

The measurement of $\mathrm{M_W}$ and of Γ_W are performed on samples of $\mathrm{W^+W^-} \to \ell\overline{\nu}_\ell \mathrm{q\bar{q}'}$ and $\mathrm{W^+W^-} \to \mathrm{q\bar{q}'\bar{q}q'}$ events; these two channels are discussed in turn below. The reconstruction of events where both Ws decay leptonically has very limited sensitivity to the W mass and width, as they contain at least two undetected neutrinos, and hence are not used in this analysis.

The first stage in the analysis is to select events from these decay channels, using either a neural network or a sequential cut-based approach. In some channels, after preliminary cuts, the probability is assessed for each event of how $\mathrm{W^+W^-}$-like it is and a corresponding weight is applied in the analysis.

The resolution of the kinematic information extracted from the observed particles in the event can be improved by applying energy and momentum conservation constraints to the event; this is discussed in section 5.1. In the fully-hadronic channel the jet directions used as the input to the kinematic fit are also assessed excluding particles from the inter-jet regions. This alternative approach reduces the sensitivity of the W mass analysis to final state interaction systematics and is discussed in section 5.3.2.

The next stage in the analysis is to produce a likelihood function expressing the relative probability of observing an event as a function of $\mathrm{M_W}$ and Γ_W. The likelihood functions used below depend not only on the reconstructed W mass of the event but make use of other event characteristics to assess the relative weight and resolution of each event. These likelihood functions are then calibrated against simulated events.

The W mass and width are then extracted by maximising the combined likelihood function of the full observed dataset.

5.1 Application of Kinematic Constraints to Event Reconstruction

The event-by-event uncertainty on the centre-of-mass energy, *i.e.* the energy spread, at LEP is typically 0.1%, while the overall momentum and energy resolution of the observed final state is about 10%. Hence, the precise knowledge of the kinematics in the initial state can be used to significantly improve the reconstructed kinematic information obtained from the clustered jets and observed leptons in the final state. This is accomplished by means of a χ^2 fit based on the four constraints from the conservation laws of energy and momentum.

The reconstructed jets and leptons of the event may be associated with one of the two hypothesised W bosons in the event. A fifth constraint may then be applied to the event by assigning equal masses to these W boson candidates. As the decay width of the $W^{\pm}$ bosons is finite, this constraint is non-physical. However, as the event mass resolution and 2 GeV/c^2 W width are of comparable magnitude in practice this constraint provides a useful approximation. It is of particular use in the semi-leptonic decay channels where, after applying the four-constraints, the event mass resolution is still larger than the W width and, due to the unseen neutrino, the two fitted masses are strongly anticorrelated. However, in the fully-hadronic decay channel the mass resolution after the four-constraint fit is better and the correlation is less; hence more information is available in the two four-constraint masses than the combined five-constraint event mass.

Parameterisation of Jets and Leptons

Each fitted object, jet or lepton, is described by three parameters. Muons are described by their measured momenta and their polar and azimuthal angles. The uncertainties on these parameters are obtained directly from the track fit. Electrons are characterized by their measured energies and their detected angular position in the electromagnetic calorimeters. The energy uncertainties are obtained from parameterisations of the responses of the electromagnetic calorimeters, which were tuned to the responses found in Bhabha and Compton scattering events. The angular uncertainties were determined from the detector granularity and were significant only for the forward electromagnetic calorimeter. In semi-leptonic events, the neutrino momentum vector is considered as unknown, which leads to a reduction by three in the number of effective constraints in the kinematic fit.

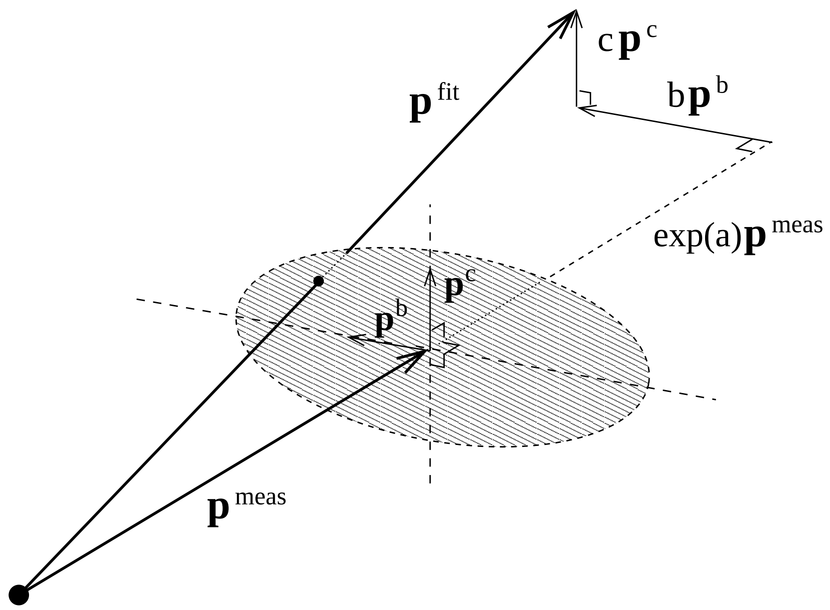

Figure 1: Parameterisation used for jets in the constrained fit, as explained in the text and equation 1.

Each fitted jet momentum $\vec{p}_j^{\,f}$ is projected onto a set of axes with one component parallel to the measured jet momentum $\vec{p}_j^{\,m}$ and two transverse components, $\vec{p}_j^{\,b}$ and $\vec{p}_j^{\,c}$, each normalized in magnitude to 1 GeV/c. In this coordinate system $\vec{p}_j^{\,f}$ can be described by three parameters a_j, b_j and c_j:

$$\vec{p}_j^{\,f} = e^{a_j}\vec{p}_j^{\,m} + b_j\vec{p}_j^{\,b} + c_j\vec{p}_j^{\,c}, \tag{1}$$

where each component is shown in figure 1. The measured jet energy $E_j^{\,m}$ is rescaled with the same factor e^{a_j} as the jet momentum. The exponential parameterisation e^{a_j} of the factor in front of $\vec{p}_j^{\,m}$ makes the fit more stable and results in uncertainties which have a more Gaussian distribution. The values of the parameters are determined by performing a constrained fit, while the transverse directions are given by the eigenvectors of the momentum tensor described below.

Form of χ^2

The algorithm minimizes a χ^2, defined for fully-hadronic events as:

$$\chi^2 = \sum_{j=1}^{jets} \frac{(a_j - a_0)^2}{\sigma_{a_j}^2} + \frac{{b_j}^2}{\sigma_{b_j}^2} + \frac{{c_j}^2}{\sigma_{c_j}^2}, \tag{2}$$

while forcing the fitted event to obey the constraints. The appropriate terms are included in the χ^2 for events with a leptonic W decay. The expected energy loss parameter a_0 and the energy spread parameter σ_{a_j}, together with the parameters σ_{b_j} and σ_{c_j}, are parameterised as functions of the jet polar angles.

Jet Error Parameterisation

The jet error parameters, a_0, σ_{a_j}, σ_{b_j} and σ_{c_j} were obtained from a study of hadronic Z events. Hadronic Z events with a two-jet topology were selected from the Z calibration run data or from the corresponding Monte Carlo simulation. The reconstructed jet energies were compared with the beam energy. In general an energy loss of around 10% was observed for jets in the barrel region of the detector while this increased to 15% in the forward regions. A good agreement between the data and simulation was found. The energy loss increases if the event jet topology becomes less two-jet like, resulting in energy losses of around 15% for the barrel region and up to 35% in the forwards regions.

The uncertainties on the jet parameters for the first stage of the fit were determined from this study as a function of the polar angle of the jet. However, a dependence of these parameters on the properties of the individual jets has also been observed.

Jet Breadth

The dependence of the uncertainties on the individual jet properties is included in a second stage of the fit, where the parameterisation of the transverse momentum uncertainties depends upon the breadth of the jet. This breadth is calculated by projecting the momenta of all particles in the jet on to the plane transverse to the jet axis. From these projections a two dimensional momentum tensor $\mathcal{T}_{\beta\gamma}$ is created:

$$\mathcal{T}_{\beta\gamma} = \sum_k p^k_\beta p^k_\gamma, \tag{3}$$

where p^k_β and p^k_γ are the two components of the projection of the momentum of particle k in the transverse plane. The normalized eigenvectors of the tensor, $\vec{p}_j^{\,b}$ and $\vec{p}_j^{\,c}$, reflect the directions where the jet is broadest and slimmest. The corresponding eigenvalues are

B_b and B_c. By comparing the resulting jet energies from the first stage of the fit with the measured ones, an estimate is made of how much energy remained undetected in the jet, referred to as $E_{j,miss}$. The uncertainties on the jet breadths were then parametrised as a function of the eigenvalues, the measured jet energy and the missing energy $E_{j,miss}$.

Use of χ^2

The χ^2 of the resulting fit is a function of the collection of jet parameters (a_j, b_j, c_j) and lepton parameters. The jets and leptons are paired appropriately to each W boson decay and constraints applied. The total χ^2 is then minimized by an iterative procedure using Lagrange multipliers for the constraints.

Events for which the χ^2 of the fit is larger than the number of degrees of freedom for the fit, NDF, had their errors scaled by a factor of $\sqrt{\chi^2/NDF}$ in order to take non-Gaussian resolution effects into account.

In the semi-leptonic analysis described in section 5.2.3 the value of the best fit mass from the χ^2 minimum and the error on this mass is used for each event. In the fully-hadronic analysis described in section 5.3.3 each event uses the χ^2 distribution as a function of the masses of the two W bosons in the event.

5.2 Semi-Leptonic Decay Channel

The $\mathrm{W^+W^-} \to \ell\overline{\nu}_\ell \mathrm{q\bar{q}'}$ events constitute 44% of all $\mathrm{W^+W^-}$ decays. The $\mathrm{W^+W^-}$ event candidates are classified according to their leptons and their selection is performed using a neural network. An event W mass is reconstructed in a kinematic fit, by imposing momentum conservation, the measured centre-of-mass energy and equality of the leptonic and hadronic decay W masses. An estimate of the mass resolution in each individual event is also obtained from the kinematic fit and an estimate of the event purity is obtained from the neural network output; these quantities are both used in producing the likelihood function from which $\mathrm{M_W}$ and Γ_W are determined.

5.2.1 Event Selection

Events are selected from the recorded data sample requiring that all detectors essential for this measurement were fully efficient: these comprise the central tracking detectors and the electromagnetic calorimeters. The data recorded during the period with a damaged sector of the TPC are also used with matching simulation samples produced. The corresponding integrated luminosities, at each centre-of-mass energy, are given in table 1.

Events containing at least three charged particle tracks and with a visible mass greater than 20 GeV/c^2 are considered for analysis. Events containing lepton candidates are then identified in this sample, either by direct lepton identification (electrons and muons), or by clustering the events into a three-jet configuration and selecting the jet with the lowest charged multiplicity as the tau candidate. At this stage, events can be considered as candidates in multiple channels.

Electron and Muon Identification

Charged particles are identified as muons if they are associated with a hit in the muon chambers, or have an energy deposit in the hadron calorimeter that is consistent with a minimum ionising particle. Muon identification is performed in the polar angle range between 10° and 170°. Muons with an unambiguous association [10] with the hits in the muon chambers, or with a loose association in addition to a good pattern in the hadron calorimeter are classified as good candidates, with the remainder being classified as possible candidates.

Electron identification is performed in the polar angle range between 15° and 165° by selecting charged particles with a characteristic energy deposition in the electromagnetic calorimeters. In the central region of the detector, covered by the HPC electromagnetic calorimeter, the electron selection followed the criteria described in [10] for candidates below 30 GeV. This selection is based on a neural network using the electron energy to momentum ratio (E/p), the spatial matching between the extrapolated track and the shower, the shower shape and the track energy loss per unit path length in the TPC (dE/dx) as the discriminating variables. Above 30 GeV, a simplified selection is adopted, the main deposit associated with a charged particle track is identified and the surrounding electromagnetic showers are clustered into this electron candidate. Only candidates with E/p greater than 0.5 are used. In the polar angle region corresponding to the forward electromagnetic calorimeter acceptance, below 36° and above 144°, electron candidates are selected from among the calorimetric shower clusters. Only clusters with an energy above 8 GeV and which could be geometrically associated to extrapolated charged particle tracks are used. The electron candidates are separated into categories of good and possible candidates based on the quality of the track associated with the electron. The association of vertex detector hits to the track is a primary criterion used in assessing the track quality.

Tau reconstruction

As mentioned above, tau candidate events are clustered into a three-jet configuration using the `LUCLUS` [23] algorithm. Tracks at large angle (more than 40° from the nearest jet axis) or which contribute a large mass to the jet they belong to (ΔM bigger than 3.5 GeV/c^2) are removed from the tau candidate. As the tau lepton predominantly decays into a final state with one or three charged particles, with few neutrals, a pseudo-multiplicity defined as the sum of the charged multiplicity and one quarter of the neutral multiplicity is used and the jet with the lowest pseudo-multiplicity is chosen as the tau candidate. Then a further cleaning is applied on this tau candidate : tracks at more than 20° from the tau axis, or which contribute a large mass (ΔM bigger than 2.5 GeV/c^2) are removed from the tau candidate. Only tau candidates containing between one and four charged particle tracks after this cleaning, and with a polar angle between 15° and 165° are kept. Two classes of events are then defined, those with only one charged particle track, and all others.

Event Reconstruction and Pre-selection

After the lepton identification is performed, the events are reconstructed as the lepton and a two or three jet system. Pre-selection cuts are then applied.

All tracks not associated to the lepton are clustered using the `LUCLUS` algorithm. These jet tracks in semi-leptonic electron and muon decay channel events are clustered with $d_{\text{join}} = 7.5$ GeV/c,where d_{join} is a measure of the clusterisation scale used inside `LUCLUS`. If more than three jets are obtained the tracks are forced into a three-jet configuration. This procedure correctly treats events with hard gluon radiation (the proportion of three-jet events is about 20%). In semi-leptonic tau decay events the tracks not associated to the tau candidate are forced into a two-jet configuration.

A set of pre-selection cuts is then applied. First, a common set of criteria is applied to the system of jets:

- visible mass greater than 30 GeV/c^2;

- at least five charged particle tracks, with at least two with momentum transverse to the beam greater than 1.5 GeV/c and compatible with the primary vertex (impact parameter in $R\ <0.15$ cm and in $z\ <0.4$ cm);
- no electromagnetic cluster with an energy bigger than 50 GeV.

Then, for electron and muon semi-leptonic decay channel events, the following additional cuts are used:

- energy of the lepton bigger than 20 GeV;
- if there is another isolated lepton of the same flavour and opposite charge, the event acollinearity should be bigger than 25°. The acollinearity used here is that between the two 'jets' when forcing the event into a two-jet (including the lepton) configuration.

Further cuts are made for electron decay channel events:

- missing transverse momentum should be greater than 8 GeV/c;
- the cut on missing transverse momentum is increased to 12 GeV/c for electron candidates in the 'possible' class;
- angle between the lepton and the nearest jet greater than 15°.

The cuts specific to the muon decay channel events are:

- angle between the lepton and the nearest jet greater than 15° in the case of 'possible' class muons;
- angle between the missing momentum and the beam axis greater than 10° for muon candidates in the 'possible' class.

While for tau decay channel events, the cuts applied are:

- visible hadronic mass smaller than 130 GeV/c^2;
- energy of the tau greater than 5 GeV;
- fraction of energy of the tau associated to charged tracks greater than 5%;
- at least one of the charged particle tracks from the tau must have a vertex detector hit;
- angle between the tau and the nearest jet greater than 15°;
- angle between the tau and the nearest charged particle greater than 10°;
- missing transverse momentum greater than 8 GeV/c;
- the cut on missing transverse momentum is increased to 12 GeV/c in the case of tau candidates with several charged particles.

The semi-leptonic electron and muon events are then reconstructed using a constrained fit imposing conservation of four-momentum and equality of the two W masses in the event. As the energy of the tau lepton is unknown, due to the emission of at least one neutrino in its decay, the mass in the $\tau\overline{\nu}_\tau \mathrm{q\bar{q}'}$ channel is entirely determined by the jet system and no improvement can be made from applying a constrained fit.

Selection

The event selection is based upon a multi-layer perceptron neural network [24]. The network has been optimised separately for the six classes of events (good and possible $\mathrm{e}\overline{\nu}_\mathrm{e}\mathrm{q\bar{q}'}$, good and possible $\mu\overline{\nu}_\mu\mathrm{q\bar{q}'}$, and $\tau\overline{\nu}_\tau\mathrm{q\bar{q}'}$ candidates containing either only one or several charged particles).

The choice of the variables used in the neural networks is a compromise between their independence from the W mass and their discriminant power. The number of

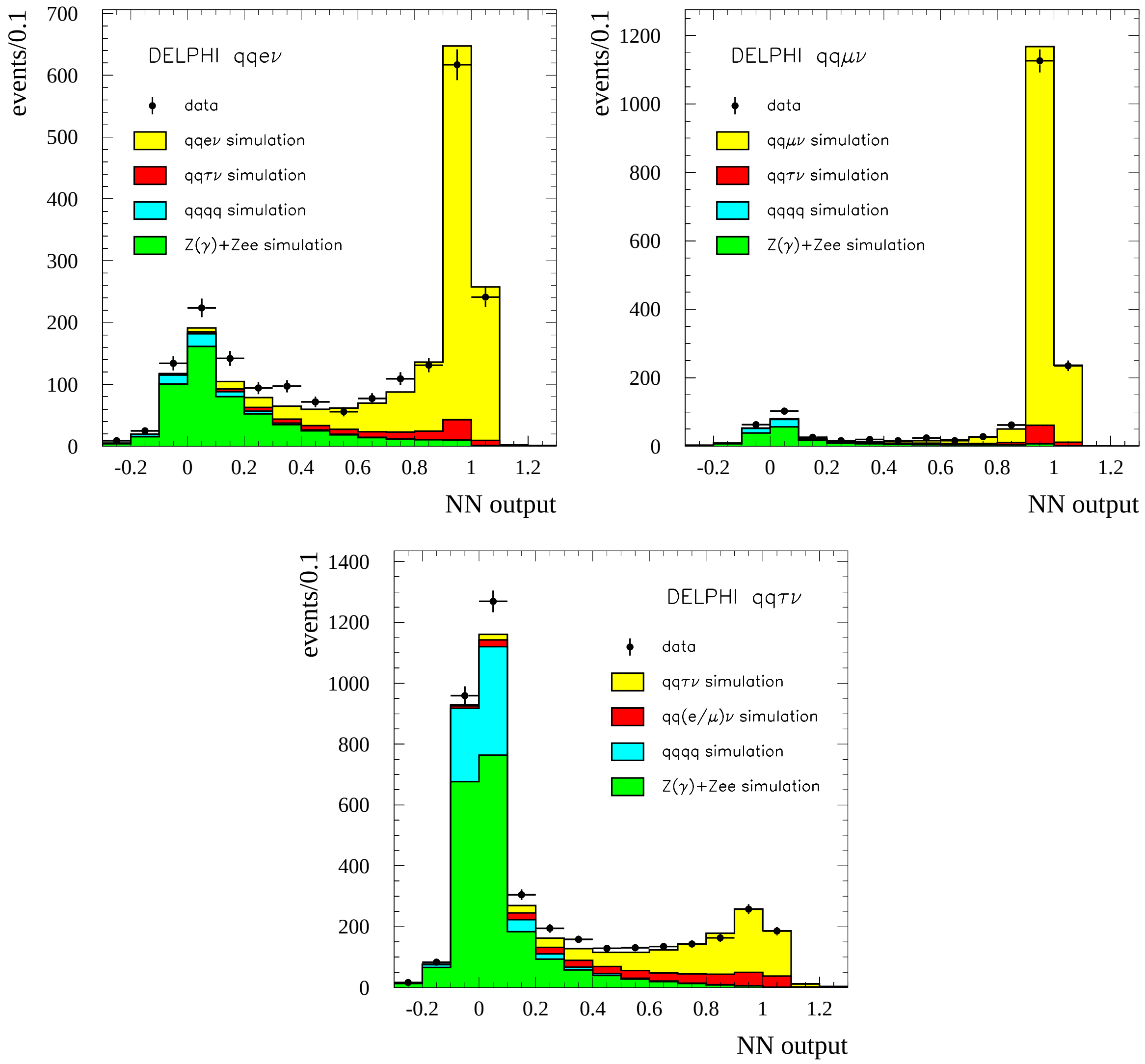

Figure 2: The output of the neural network used for the selection of the semi-leptonic channels for the data sample recorded at $\sqrt{s} = 183 - 209$ GeV. The data are indicated by the data points with error bars. The histograms show the signal and background simulation contributions normalised to the integrated luminosity of the data sample.

input-hidden-output nodes were 12-8-1, 11-7-1 and 17-12-1 for the e, μ and τ channels respectively. The detailed list of variables is given below. The network has been tuned on samples of signal and background simulation events, and examples of the distribution of the neural network output value are shown in figure 2. The applied selection cut is at 0.40, 0.50 and 0.35 for the e, μ and τ channels respectively, independent of the centre-of-mass energy. Any discrepancy in the background rate between data and simulation is accounted for in the systematic uncertainty applied.

The event selection procedure ensures that the events are only selected in one of the channels: events that pass the chosen cut in the muon channel are selected, the remaining events are considered as electron channel candidates and, if they are again rejected, are then analysed under the tau channel hypothesis. This ordering follows the hierarchy of purities in these channels (and is not dependent on the good or possible lepton classes). After applying the cut on the network output the selection performance is as shown in table 2. As an example, the global efficiencies for `CC03` events are 79.8%, 89.8% and 59.3% respectively for the $\mathrm{e}\overline{\nu}_{\mathrm{e}}\mathrm{q}\bar{\mathrm{q}}'$, $\mu\overline{\nu}_{\mu}\mathrm{q}\bar{\mathrm{q}}'$ and $\tau\overline{\nu}_{\tau}\mathrm{q}\bar{\mathrm{q}}'$ events in the data taken at $\sqrt{s} = 189$ GeV. These numbers are integrated over all event selections as there is a non-negligible cross-contamination of events in the event selections (*e.g.* $\mathrm{e}\overline{\nu}_{\mathrm{e}}\mathrm{q}\bar{\mathrm{q}}'$ event selected by the $\tau\overline{\nu}_{\tau}\mathrm{q}\bar{\mathrm{q}}'$ selection) which still add useful information in the W mass and width fits. Here `CC03` refers to the three charged current processes producing the $\mathrm{W}^+\mathrm{W}^-$ state for which this analysis is intended: s-channel photon or Z production and t-channel ν_e exchange.

	Simulation						
1998, 189 GeV	(Primary-l)$\overline{\nu}_\ell\mathrm{q}\bar{\mathrm{q}}'$	(Other-l)$\overline{\nu}_\ell\mathrm{q}\bar{\mathrm{q}}'$	$\mathrm{q}\bar{\mathrm{q}}'\bar{\mathrm{q}}\mathrm{q}'$	$q\bar{q}(\gamma)$	Other 4f	Total	Data
$\mathrm{e}\overline{\nu}_{\mathrm{e}}\mathrm{q}\bar{\mathrm{q}}'$	257.5	10.5	0.7	9.3	6.5	284.5	256
$\mu\overline{\nu}_{\mu}\mathrm{q}\bar{\mathrm{q}}'$	321.2	10.2	0.4	1.1	2.2	335.1	320
$\tau\overline{\nu}_{\tau}\mathrm{q}\bar{\mathrm{q}}'$	198.2	56.6	3.5	18.6	10.9	287.9	294
$\mathrm{q}\bar{\mathrm{q}}'\bar{\mathrm{q}}\mathrm{q}'$	–	34.0	1029.9	341.6	50.8	1456.3	1506
2000, 206 GeV							
$\mathrm{e}\overline{\nu}_{\mathrm{e}}\mathrm{q}\bar{\mathrm{q}}'$	373.9	16.9	1.0	13.6	11.4	416.8	395
$\mu\overline{\nu}_{\mu}\mathrm{q}\bar{\mathrm{q}}'$	457.0	14.8	0.6	1.7	4.1	478.2	467
$\tau\overline{\nu}_{\tau}\mathrm{q}\bar{\mathrm{q}}'$	290.2	87.6	5.7	22.3	21.4	427.2	426
$\mathrm{q}\bar{\mathrm{q}}'\bar{\mathrm{q}}\mathrm{q}'$	–	40.6	1514.5	460.9	107.8	2123.8	2134
1997-2000 183-206 GeV							
$\mathrm{e}\overline{\nu}_{\mathrm{e}}\mathrm{q}\bar{\mathrm{q}}'$	1091.5	47.7	2.9	39.9	30.7	1212.7	1182
$\mu\overline{\nu}_{\mu}\mathrm{q}\bar{\mathrm{q}}'$	1356.7	43.3	1.7	15.2	11.0	1417.8	1402
$\tau\overline{\nu}_{\tau}\mathrm{q}\bar{\mathrm{q}}'$	849.3	248.6	16.0	72.2	55.6	1241.6	1270
$\mathrm{q}\bar{\mathrm{q}}'\bar{\mathrm{q}}\mathrm{q}'$	–	131.6	4421.0	1399.5	269.8	6222.0	6446

Table 2: Number of selected events in the decay channel event selections from the 1998 and 2000 data samples and the combined 1997-2000 data sample, and the corresponding number of expected events from the simulation. The table is split into rows giving the results of each of the event selection routines. The primary-l and other-l $\overline{\nu}_\ell\mathrm{q}\bar{\mathrm{q}}'$ columns relate to the nature of the semi-leptonic event selections *e.g.* for the $\mathrm{e}\overline{\nu}_{\mathrm{e}}\mathrm{q}\bar{\mathrm{q}}'$ selection the results are for the $\mathrm{e}\overline{\nu}_{\mathrm{e}}\mathrm{q}\bar{\mathrm{q}}'$ and $(\mu\overline{\nu}_{\mu}\mathrm{q}\bar{\mathrm{q}}' + \tau\overline{\nu}_{\tau}\mathrm{q}\bar{\mathrm{q}}')$ channels respectively.

For each of the six classes of events, the fraction of semi-leptonic $\mathrm{W}^+\mathrm{W}^-$ events in the sample has been extracted from simulation as a function of the neural network output:

this is referred to below as the event purity P_e. This feature is particularly useful for the tau selection, where the proportion of background events is highest.

5.2.2 Variables used in the Selection Neural Networks

Common Variables for all Leptonic Channels

- Polar angle of the leptonic W (after applying the constrained fit);
- angle of the charged lepton with respect to the direction of the leptonic W (in the W rest frame, and after the constrained fit);
- polar angle of the lepton;
- polar angle of the missing momentum vector;
- angle between the lepton and the nearest jet;
- angle between the lepton and the nearest charged hadron track (of energy greater than 1 GeV);
- missing transverse momentum;
- the invariant mass of the measured system of particles $\sqrt{s'}$ [25] - this is measured using planar kinematics, by forcing the event into 2 jets (using all particles in the event including the lepton) and assuming a photon is emitted down the beam pipe;
- aplanarity (cosine of the angle between the lepton and the normal to the plane formed by the jets[2]);
- acollinearity (complement of the angle between the two "jets" when forcing the event into a two-jet configuration);
- the minimum $\mathrm{d_{join}}$ distance in the `LUCLUS` jet clusterisation algorithm between two jets in the final configuration, where the whole event (hadronic and leptonic system) is forced into three jets. This is known as $\mathrm{d_{j3all}}$.

Additional Variable for the Electron Channel Only

- Angle between the missing momentum and the nearest jet.

Additional Variables for the Tau Channel Only

- Angle between the missing momentum and the nearest jet;
- fraction of the tau energy coming from charged particle tracks;
- missing energy;
- reconstructed tau energy;
- reconstructed tau mass;
- $\mathrm{d_{j4all}}$, as $\mathrm{d_{j3all}}$ (see above) but with the final event configuration forced into four jets.

5.2.3 Likelihood Function

A likelihood function, $\mathcal{L}_e(\mathrm{M_W}, \Gamma_\mathrm{W})$, is evaluated for each selected event with a reconstructed mass in a defined range. The range was 67-91 GeV/c^2 for the data collected in 1997, 67-93 GeV/c^2 for 1998, 67-95 GeV/c^2 for 1999, and 67-97 GeV/c^2 for 2000. The increase in range with rising centre-of-mass energy is to account for the increasing ISR tail. The likelihood function is defined as follows:

$$\mathcal{L}_e(\mathrm{M_W}, \Gamma_\mathrm{W}) = P_e \cdot S''(m^{fit}, \sigma^{fit}, \mathrm{M_W}, \Gamma_\mathrm{W}) + (1 - P_e) \cdot B(m^{fit}),$$

where P_e is the event purity, discussed above, S'' is the signal function that describes the reconstructed mass distribution of the semi-leptonic W decays, and B is used to describe

[2] for three-jets events in the electron and muon channels, the jets-plane is the plane formed by the most energetic jet and the sum of the two others.

background processes. The reconstructed event mass m^{fit} and its estimated error σ^{fit} are both obtained from the constrained fit. The distribution of background events is extracted from simulation as a function of m^{fit}.

The signal function S'' is defined in terms of S and S' as discussed below. The function S relies on the convolution of three components, using x and m as the dummy integration variables:

$$S(m^{fit},\sigma^{fit}|\mathrm{M_W},\Gamma_\mathrm{W}) = \int_0^{E_{\mathrm{BEAM}}} dm\; G[m^{fit}-m,\sigma^{fit}] \int_0^1 dx\; PS(m(1-x))\; BW[m(1-x)|\mathrm{M_W},\Gamma_\mathrm{W}]\; R_{ISR}(x). \tag{4}$$

BW is a relativistic Breit-Wigner distribution representing the W mass distribution,

$$BW(m|\mathrm{M_W},\Gamma_\mathrm{W}) = \frac{1}{\pi}\frac{\Gamma_\mathrm{W}}{\mathrm{M_W}}\frac{m^2}{(m^2-\mathrm{M_W}^2)^2+\left(m^2\frac{\Gamma_\mathrm{W}}{\mathrm{M_W}}\right)^2}, \tag{5}$$

and PS is a phase-space correction factor

$$PS(m) = \sqrt{1-\frac{4m^2}{s}}.$$

The convolution with the Gaussian function G describes the detector resolution. The width of the Gaussian depends upon the reconstructed mass error obtained in the constrained fit for that event.

The ISR spectrum is parameterised as

$$R_{ISR}(x_\gamma) = \beta x_\gamma^{(\beta-1)},$$

where x_γ is the ratio of the photon energy to the centre-of-mass energy and β is calculated from the electromagnetic coupling constant (α), the centre-of-mass energy squared (s) and the electron mass (m_e):

$$\beta = \frac{2\alpha}{\pi}[\ln(s/m_e^2)-1].$$

Due to the constrained fit, a W produced at mass m will be reconstructed to a good approximation as $m/(1-x_\gamma)$ in the presence of an undetected ISR photon, giving a tail at high mass in the measured spectrum. This tail is well described by the integration on the photon spectrum in equation 4.

The event selection contains a significant fraction of $\tau\overline{\nu}_\tau\mathrm{q\bar{q}'}$ events in the electron and muon channel samples, and of $\mathrm{e}\overline{\nu}_\mathrm{e}\mathrm{q\bar{q}'}$ events in the tau sample (see table 2). In the tau channel the mass of the event is determined from the jet system. The behaviour of true $\tau\overline{\nu}_\tau\mathrm{q\bar{q}'}$ and $\mathrm{e}\overline{\nu}_\mathrm{e}\mathrm{q\bar{q}'}$ events in this fit are found to be similar, and $S''=S$ in this channel. However, in the electron and muon channel samples the behaviour of the $\tau\overline{\nu}_\tau\mathrm{q\bar{q}'}$ events is somewhat different to that of the $\mathrm{e}\overline{\nu}_\mathrm{e}\mathrm{q\bar{q}'}$, $\mu\overline{\nu}_\mu\mathrm{q\bar{q}'}$ events. The $\tau\overline{\nu}_\tau\mathrm{q\bar{q}'}$ events have a worse mass resolution and introduce a small negative offset on the mass. The fraction of tau events, which have been wrongly classified and are contained in the electron and muon channel samples, has been parameterised in bins of the lepton energy and the measured missing mass. This fraction $P\tau_e$ is then taken into account in the likelihood function for the electron and muon samples, by defining the signal function S'' as

$$S'' = (1-P\tau_e)\cdot S + P\tau_e\cdot S',$$

where S' is analogous to S, but with the width of the Gaussian resolution function increased according to a factor determined from simulation studies. All remaining biases in the analysis due to using this approximate likelihood description are corrected for in the calibration procedure as described in section 5.4.

5.3 Fully-Hadronic Decay Channel

The $W^+W^- \rightarrow q\bar{q}'\bar{q}q'$ events constitute 46% of all W^+W^- decays. The event masses can be reconstructed from the observed set of jets. The kinematics of the jets can be significantly over-constrained in a kinematic fit, improving the event mass resolution, by imposing momentum conservation and the measured centre-of-mass energy. The influence of the many ambiguities in the event reconstruction, which dilute the statistical information, is minimised by optimally weighting the different hypotheses in the likelihood fit of M_W or Γ_W.

The dominant systematic error is due to the possible influence of final state interference effects between particles from the two decaying Ws. Reconstructing the jet directions using only the particles from the core of the jet reduces the possible effects of these final state interference effects. This technique and the mass estimator based on all observed particles are both discussed in section 5.3.2.

5.3.1 Event Selection

As in the semi-leptonic analysis, appropriate criteria were imposed on the functionality of the detector when selecting the data sample for analysis. The corresponding integrated luminosities, at each centre-of-mass energy, are given in table 1.

The event selection can be separated into three stages. First a pre-selection is performed to reduce the data sample to events with a high multiplicity and high visible energy. In the second stage events with a four or five jet topology are retained. The observables on which the selection is made are chosen to be, to a good approximation, independent of the centre-of-mass energy $\sqrt{s}$: the same selection criteria are used for all energies for the pre-selection and jet topology selection. The final stage of the event selection is to use the inter-jet angles and jet momenta to estimate the probability that this was a $W^+W^- \rightarrow q\bar{q}'\bar{q}q'$ event.

The pre-selection cuts applied are:

- the charged particle multiplicity should be larger than 13;
- the total visible energy of the event must exceed 1.15 $\frac{\sqrt{s}}{2}$;
- the scaled effective centre-of-mass energy $\frac{\sqrt{s'}}{\sqrt{s}}$ [25] is required to be equal to or larger than 0.8;
- rejection of events tagged as likely to be containing b quarks [26].

The last criterion removes 7% of the remaining $Z \rightarrow q\bar{q}(\gamma)$ and 18% of the remaining ZZ events, while changing the signal selection efficiency by less than 1%. The distributions of data and simulation events for the scaled effective centre-of-mass energy and combined b-tag variable are shown in figure 3; the cut on the combined b-tag variable retains all events below 2.

The remaining events are then clustered using the `DURHAM` [27] jet clustering algorithm with a fixed y_{cut} of 0.002. The jets obtained are required to have an invariant mass of greater than 1 GeV/c^2 and contain at least three particles. If the jets do not meet these criteria or more than five jets are obtained, the clustering is continued to higher values of y_{cut}. Events which cannot be clustered into either four or five jets that fulfill these criteria are rejected. The initial y_{cut} value of this procedure was optimised for maximal sensitivity to M_W and results in a sample of approximately 50% four and 50% five jet events.

The jets obtained from this procedure are then used in a constrained fit, described in section 5.1, where momentum conservation and the measured centre-of-mass energy are

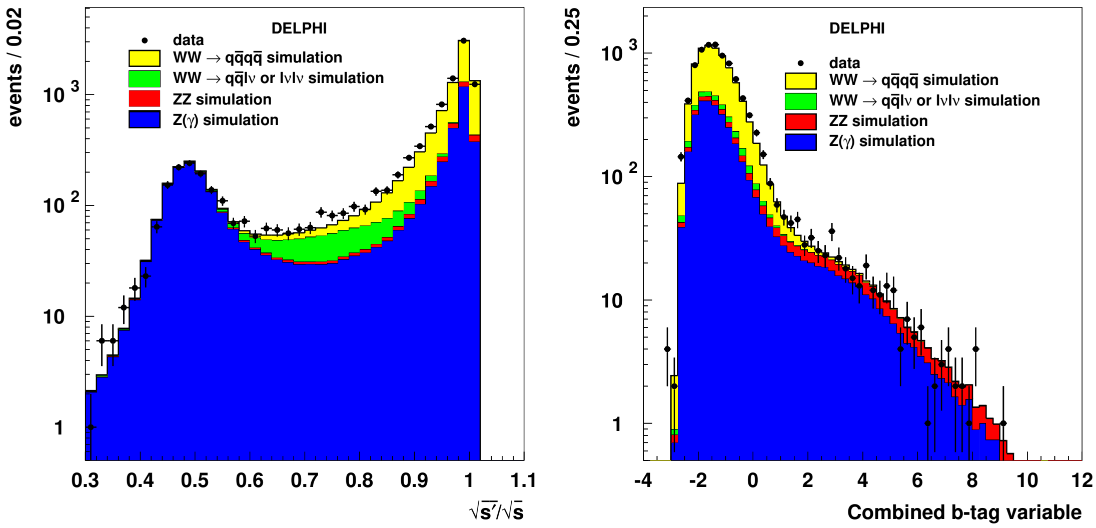

Figure 3: The distribution of two event selection variables for candidate $q\bar{q}'\bar{q}q'$ events from the full LEP2 data sample and the corresponding simulation samples. The left hand plot shows the scaled effective centre-of-mass energy, the right hand plot the combined b-tag variable. The distributions are shown after the cuts on all other pre-selection variables have been applied.

enforced. From the fitted jets a topological observable, D_{pur}, was formed to discriminate between signal events and $Z \to q\bar{q}$ events with hard gluon radiation:

$$D_{pur} = \theta^{fit} \cdot E^{fit} \cdot \sqrt{\tilde{\theta}^{fit} \cdot \tilde{E}^{fit}}$$

where E_j^{fit} and $\tilde{E}_j^{fit}$ are the smallest and second smallest fitted jet energies and θ_{ij}^{fit} and $\tilde{\theta}_{ij}^{fit}$ are the smallest and second smallest fitted inter-jet angles. The expected fraction of $q\bar{q}'\bar{q}q'$ events (W^+W^- or ZZ) in the selected sample, the event purity P^{4f}, is parameterised as a function of this variable. This fraction of $q\bar{q}'\bar{q}q'$ events, *i.e.* doubly-resonant events rather than just W^+W^- events, is used in the theoretical distribution function described below. Events with an estimated purity below 25% are rejected. The distribution of the D_{pur} observable is shown in figure 4 for both the 4 and 5 jet topology events, and the numbers of selected events are given in table 2. An excess of data events over the expected number of simulation events was observed.

5.3.2 Cone Jet Reconstruction

The largest contribution to the systematic uncertainty in the fully-hadronic decay channel arises from the hypothesis, used throughout the likelihood construction, that the fragmentation of the partons from both W bosons happens independently. However, Bose-Einstein Correlations (section 6.11) and colour reconnection (section 6.12) effects may result in cross-talk between the two W systems. A jet reconstruction technique is presented here which has been designed to have reduced sensitivity to colour reconnection effects.

Conventionally, as used for the jets in the semi-leptonic analysis, the particles in the event are clustered into jets using a jet clustering algorithm and the energy, magnitude of the momentum and direction of the jet are reconstructed from the clustered particles. The jet momentum and energy are then used as the input to the kinematic fit. This

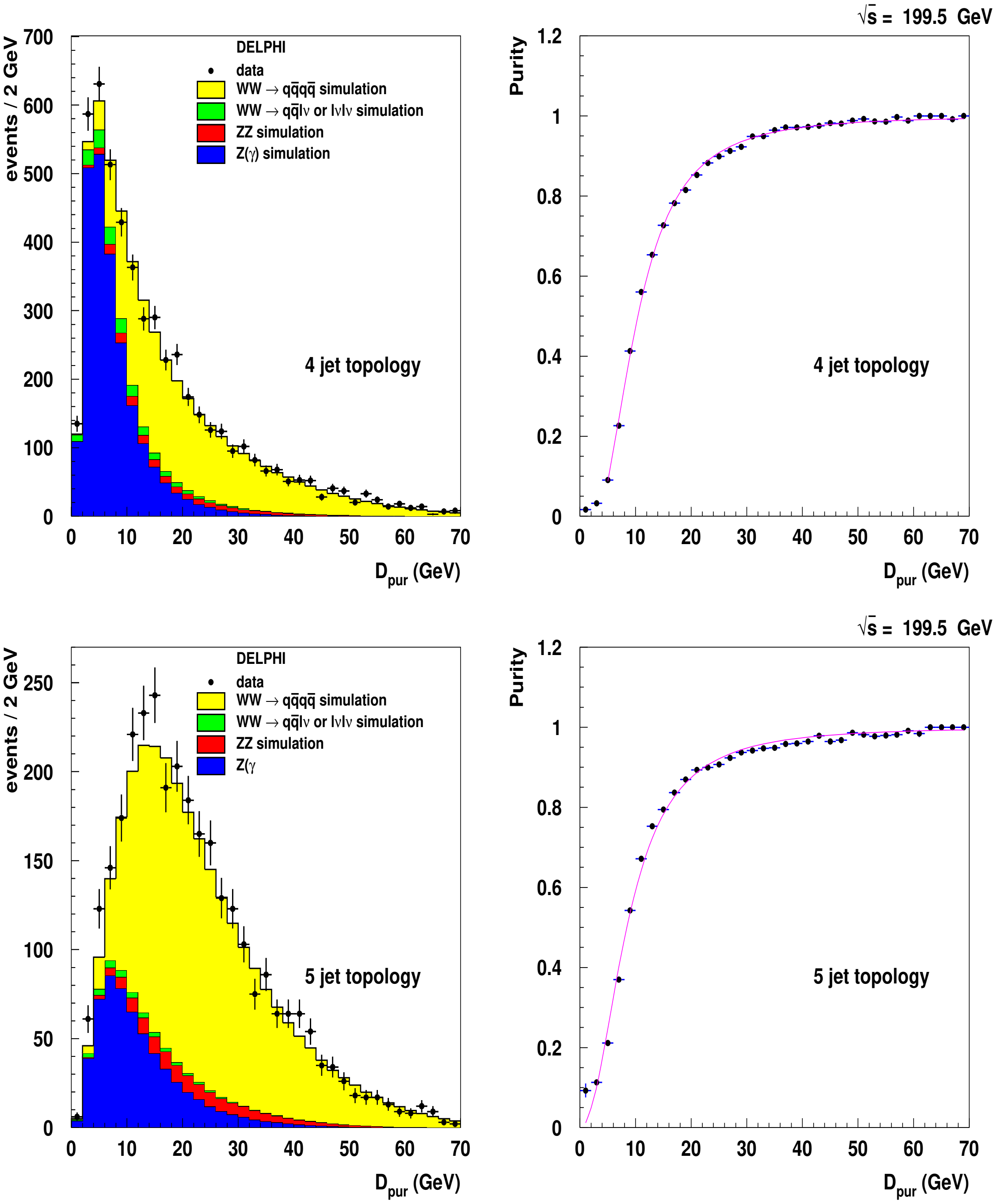

Figure 4: The left hand plots show the distribution of the D_{pur} variable for four jet (top) and five jet (bottom) events from the full LEP2 data sample and the corresponding simulation samples. The right hand plots show the distribution of the four-fermion event purity with this variable at a centre-of-mass energy of 199.5 GeV extracted from simulation events. The fitted parameterisation of this distribution is given by the line.

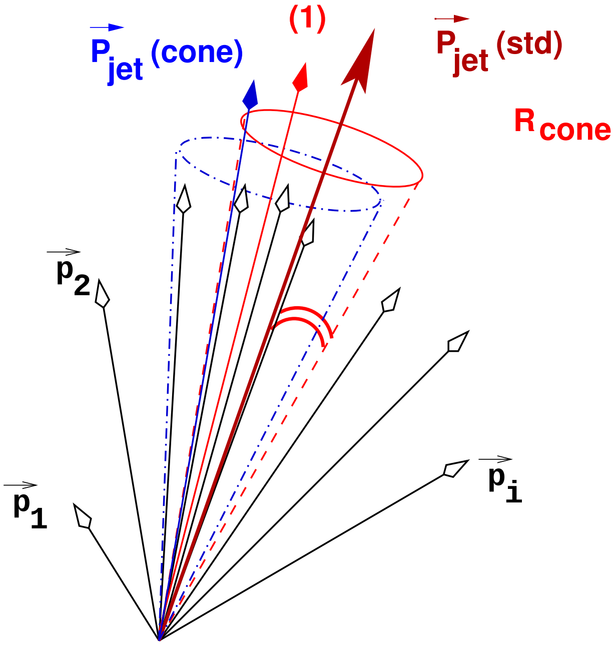

Figure 5: Illustration of the iterative cone jet reconstruction algorithm used for the fully-hadronic W mass analysis as discussed in the text.

technique is referred to in this paper as the standard reconstruction method and provides the optimal statistical sensitivity.

In the alternative reconstruction algorithm discussed here the effect of particles in the inter-jet regions on the reconstructed jet direction is reduced. This is achieved by using a cone algorithm. The initial jet direction $\vec{p}^{jet}$ is defined by the standard clustering algorithms (`DURHAM` [27], `CAMBRIDGE` [28] or `DICLUS` [29]) and a cone of opening angle R_{cone} defined around this as in figure 5. The jet direction is recalculated (direction (1) on the figure) using those particles which lie inside the cone. This process is iterated by constructing a cone (of the same opening angle R_{cone}) around this new jet direction and the jet direction is recalculated again. The iteration is continued until a stable jet direction $\vec{p}^{jet}_{cone}$ is found. Only the jet direction is changed in this procedure, the magnitude of the momentum and the jet energy are rescaled to compensate for the lost energy of particles outside the stable cone. The value of the cone opening angle R_{cone} is set to 0.5 rad, a value optimised for the measurement of the colour reconnection effect as reported in [30].

This cone jet reconstruction technique reduces the sensitivity to the colour reconnection effect (see section 6.12) at the expense of some statistical sensitivity. The expected statistical uncertainty increases by approximately 14%. This technique has been applied only to the W mass and not to the W width analysis.

This technique of jet reconstruction should not be confused with the alternative jet clustering algorithms (`DURHAM`, `CAMBRIDGE` or `DICLUS`) used in the analysis (see below). The alternative jet clustering algorithms are used as the starting point for the cone jet reconstruction in order to improve the statistical sensitivity of the analysis rather than to reduce the sensitivity to colour reconnection effects.

5.3.3 Likelihood Function

Event Ideograms

Each of the selected events is analysed through the use of a likelihood ratio function, which we will label here as the event ideogram. The final ideogram for each event consists of the weighted sum of the ideograms produced using a range of event reconstruction hypotheses h_i. These reconstruction hypotheses, including for example the possible different associations of the jets to their parent W bosons, are discussed below. The details of how these hypotheses are combined is then described below under the heading of 'Ideogram Sum'.

The ideogram reflects the relative compatibility of the kinematics of the event with the premise that two heavy objects, with masses m_x and m_y, were produced. The ideogram is based on the least-square, χ^2_{4C}, of the energy and momentum constrained fit of the observed set of jet kinematics, $\{\bar{p}_j\}$, of the reconstructed final state.

Thus, for each pair of test masses $\vec{m} = (m_x, m_y)$, we can obtain the $\chi^2_{4C}(\{\bar{p}_j\}|\vec{m}, h_i)$. As the calculation of the χ^2 over the full mass $\vec{m}$ plane is computationally intensive we apply the following approximation in the analysis. The χ^2 is only calculated once per hypothesis h_i at the minimum of the $\chi^2_{4C}(\vec{m})$ in the full $\vec{m}$-space. The probability in all other points $\vec{m} = (m_x, m_y)$ is calculated using a Gaussian approximation for the $\chi^2(\vec{m})$ given by:

$$\chi^2_i(m_x, m_y) \simeq \chi^2_{4C} + (\mathbf{m} - \mathbf{m}^{\rm fit})^T \mathbf{V}^{-1} (\mathbf{m} - \mathbf{m}^{\rm fit}),$$

with

$$\begin{aligned} \mathbf{m} &= \begin{pmatrix} m_x \\ m_y \end{pmatrix}, \\ \mathbf{m}^{\rm fit} &= \begin{pmatrix} m_x^{\rm fit} \\ m_y^{\rm fit} \end{pmatrix}. \end{aligned}$$

The masses m_x^{fit}, m_y^{fit}, and the covariance matrix $\mathbf{V}$ are taken from the 4C kinematic fit. When the χ^2_{4C} is larger than the number of degrees of freedom (NDF=4), the $\chi^2_i(m_x, m_y)$ is rescaled with a factor NDF/χ^2_{4C} in order to compensate for non-Gaussian resolution effects.

This procedure decreases the computing time taken by an order of magnitude compared with the full six constraint fit [3], while resulting in only a minimal reduction in the W mass precision obtained ($2 \pm 1\%$).

We denote the ideogram of the event under hypothesis h_i as $P(\{\bar{p}_j\}|\vec{m}, h_i)$. Assuming a Gaussian form, this is calculated from the χ^2 as follows:

$$P(\{\bar{p}_j\}|\vec{m}, h_i)\, d\vec{m} \;=\; \exp\left(-\frac{1}{2} \cdot \chi^2_{4C}(\{\bar{p}_j\}|\vec{m}, h_i)\right) d\vec{m}.$$

Example ideograms are shown in figure 6. These ideograms show the weighted sum of the reconstruction hypothesis ideogram terms for an individual event. The reconstruction hypotheses, which we will discuss in the following sections, include a range of options for the jet clustering algorithms that assign particles to jets, the possible associations of jets to W bosons, and a treatment for events that may have significant initial state radiation.

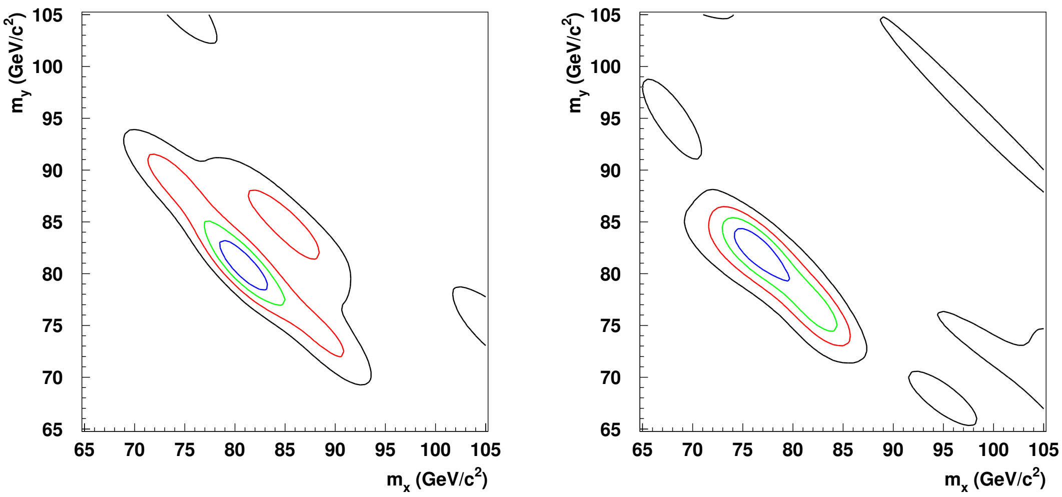

Figure 6: Examples of a reconstruction hypothesis weighted sum of two-dimensional probability ideograms (see text) for a four-jet (left) and five-jet (right) hadronic event. The ideograms include terms from each potential jet-pairing, three jet clustering algorithms and possible ISR emission. The 1,2,3 and 4-sigma contours are shown.

Jet Pairings

As discussed in section 5.3.1, the reconstructed particles in the event were clustered into four or five jets. These jets can then be associated to their parent W bosons. For events clustered into four (five) jets there are three (ten) combinatorial possibilities for the jet pairing into W bosons. The relative probability of each of these jet pairings to be the correct jet association is estimated.

This jet to W boson association weight, w_k, is estimated as a function of the reconstructed polar angle of the W boson and the estimated charge difference between the two reconstructed W bosons in the event. For the five jet events the transverse momentum of the gluon jet is also used.

The production angle θ_W of the W^+ (W^-) boson is correlated with the flight direction of the incoming e^+ (e^-) beam. For each jet pairing the W boson polar angle was calculated and its probability $P_\theta(\theta_W)$ assessed from a centre-of-mass dependent parameterisation of correctly paired simulation events.

The jet charge Q^i_{jet} for jet i in the clustered event can be measured as:

$$Q^i_{jet} = \frac{\sum_{n=1}^{n_{jet}} |\vec{p}_n|^{0.5} \cdot q_n}{\sum_{n=1}^{n_{jet}} |\vec{p}_n|^{0.5}}$$

where n_{jet} are all charged particles in jet i, while q_n and $\vec{p}_n$ are their charge and momentum. For each association k of the jets to their parent W bosons the charge difference $\Delta Q_k = Q_k^{\mathrm{W}_1} - Q_k^{\mathrm{W}_2}$ is obtained. Again, the probability of this being the correct jet assignment is assessed using a Monte Carlo simulation-derived parameterisation. The relative weight for each jet pairing k can be expressed as:

$$w_k^W = P_{W^+}(\Delta\ Q_k) \cdot P_\theta(\theta^k_{W_1}) + (1 - P_{W^+}(\Delta\ Q_k)) \cdot P_\theta(\pi - \theta^k_{W_1}).$$

In five jet events, a two jet and a three jet system are considered. The three jet system is considered as comprising a $q\bar{q}$ pair and a gluon jet. The probability of emission of a gluon from a $q\bar{q}$ pair is approximately inversely proportional to the transverse momentum of the gluon with respect to the original quarks. Hence, the most probable gluon jet in the three jet system is the jet with the smallest transverse momentum (k_T) with respect to the two other jets in the candidate W boson rest frame. Each of the ten possible jet associations, in this five jet event, is then given a relative weight from its most probable gluon jet of $w_k^{gluon} = 1/k_T$.

The combined relative jet pairing weight of each combination is given by multiplying the jet pairing weights w_k^W and, for five jet events, also multiplying by the w_k^{gluon} weight. The relative weights are then normalised so that the sum of the weights for all the jet-paring combinations of the event is 1, giving combination weights w_k. The use of all the jet pairings, rather than simply picking the best one, improves the statistical precision of this analysis by 4%.

Jet Clustering Algorithms

Several standard jet clustering algorithms are used in this analysis. Whilst the overall performances of the algorithms are similar, the reconstruction of an individual event can differ significantly. In this analysis, the event ideograms were reconstructed with three clustering algorithms `DURHAM`, `CAMBRIDGE` and `DICLUS`. The ideograms resulting from each clustering algorithm are summed with fixed optimised relative weights, w_c, determined from simulation events. The sum of the three jet clustering weights for one event is normalised to 1.

The use of a range of jet clustering algorithms, rather than taking only one, improves the statistical precision of this analysis by 5%.

Initial State Radiation Hypotheses

A kinematic fit (see section 5.1) is performed with modified constraints and an extra free parameter p_z^{fit} to account for the possible emission of an ISR photon of momentum p_z inside the beam pipe. The modified constraints are:

$$\sum_{i=1}^{n_{\text{objects}}} (E, p_x, p_y, p_z)_i = (\sqrt{s} - |p_z^{\text{fit}}|, 0, 0, p_z^{\text{fit}}).$$

The probability that the missing momentum in the z direction is indeed due to an unseen ISR photon was extracted from the simulation as a function of $|p_z^{\text{fit}}|/\sigma_{p_z}$, where σ_{p_z} is the estimated error on the fitted z momentum component; only events with this ratio greater than 1.5 are treated with the mechanism described below.

Additional ideograms are then calculated for these events, with a relative weight factor derived from the ISR hypothesis probability. The ideogram obtained without the ISR hypothesis is given a relative weight 1, while the other ideograms obtained from this procedure are given relative weight factors according to the distribution shown in figure 7. The weights are then normalised such that the sum of the ISR and no ISR hypotheses for an event sum to 1, giving ISR weights w_{isr}.

This treatment is applied to 15% of the events and results in an improvement of the expected W mass error for these events of 15%.

Ideogram Sum

An ideogram is produced for each event under each of the possible reconstruction hypotheses. For four jet events there are three jet association hypotheses to be performed with three clustering algorithms and maximally two ISR hypotheses, giving a total of eighteen ideograms. For five jet events there are sixty possible ideograms. The final ideogram for each event is produced as a weighted sum of these:

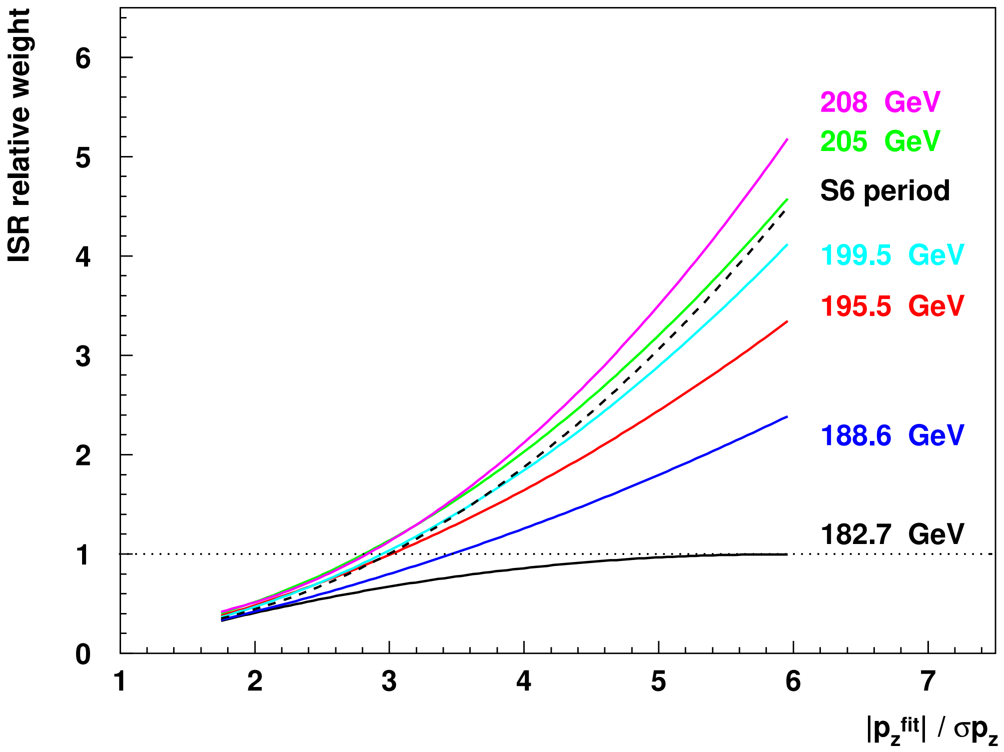

Figure 7: Parameterised weight given to the ISR solution of the kinematic fit, relative to the unity weight of the no ISR solution, as a function of the $|p_z^{\rm fit}|/\sigma_{p_z}$ value of the event for different centre-of-mass energies. The period with a damaged TPC sector (S6) is indicated with a dashed line.

$$P(\{\bar{p}_j\}|\vec{m},\{h_i\}) \;=\; \sum_{k=1}^{3\ \text{or}\ 10}\ \sum_{isr=1}^{2}\ \sum_{c=1}^{3} w_k\cdot w_{isr}\cdot w_c\cdot P(\{\bar{p}_j\}|\vec{m},h_{k,isr,c}),$$

where the sum over k takes into account the three or ten possible jet pairings in the event, the sum over isr the two different initial state radiation hypotheses used in the kinematic fit and the sum over c the three jet clustering algorithms. The sum of all weights for each event is fixed to unity, so that while possible reconstruction hypotheses within an individual event have different weights the overall weight for each event is the same.

Likelihood

To obtain information about $\mathrm{M_W}$ and Γ_W a theoretical probability distribution function, $P(\vec{m}|\mathrm{M_W},\Gamma_\mathrm{W})$, is required predicting the population density in the $\vec{m}$-plane of the event ideogram. The ideogram in $\vec{m}$-space can then be transformed into a likelihood, $\mathcal{L}_e(\mathrm{M_W},\Gamma_\mathrm{W})$, in the ($\mathrm{M_W}$,$\Gamma_\mathrm{W}$)-space by convoluting it with this expected distribution $P(\vec{m}|\mathrm{M_W},\Gamma_\mathrm{W})$:

$$\mathcal{L}_e(\mathrm{M_W},\Gamma_\mathrm{W}) = \int_{m_{\rm min}}^{m_{\rm max}}\int_{m_{\rm min}}^{m_{\rm max}} P(\{\bar{p}_j\}|\vec{m},\{h_i\})\cdot P(\vec{m}|\mathrm{M_W},\Gamma_\mathrm{W})\; d\vec{m}, \tag{6}$$

where the two-dimensional integral is over the relevant kinematic region in the $\vec{m}$-space. This region is taken to be $m_{\min} = 60$ GeV$/c^2$ and $m_{\max} = 110$ GeV$/c^2$, and the combined ideogram is normalized to unity in the same region:

$$\int_{m_{\min}}^{m_{\max}} \int_{m_{\min}}^{m_{\max}} P(\{\bar{p}_j\}|\vec{m}, \{h_i\}) \; d\vec{m} \;=\; 1.$$

Theoretical Distribution Function

The theoretical probability distribution function, $P(\vec{m}|\mathrm{M_W}, \Gamma_\mathrm{W})$, predicts the population density in the $\vec{m}$-plane of the event ideogram for a given $\mathrm{M_W}$ and Γ_W. To provide an accurate description of the data the form assumed for $P(\vec{m}|\mathrm{M_W}, \Gamma_\mathrm{W})$ must take into account not only the expected distribution for the $\mathrm{W^+W^-} \rightarrow \mathrm{q\bar{q}'\bar{q}q'}$ signal events but also that of the background events in the selected sample. The two principal components of the background, $\mathrm{Z} \rightarrow q\bar{q}(\gamma)$ and $\mathrm{ZZ} \rightarrow \mathrm{q\bar{q}'\bar{q}q'}$, are considered.

The background process $\mathrm{Z} \rightarrow q\bar{q}(\gamma)$ does not have a doubly resonant structure and a uniform population of these events is expected in the $\vec{m}$-space independent of the values of the parameters ($\mathrm{M_W}$,Γ_W). Therefore, the probability density function from this background source is assumed to be a constant denoted B. The probability (P^{4f}) that a given event is a $\mathrm{q\bar{q}'\bar{q}q'}$ event was calculated from the event topology as described in section 5.3.1.

The $\mathrm{W^+W^-} \rightarrow \mathrm{q\bar{q}'\bar{q}q'}$ and $\mathrm{ZZ} \rightarrow \mathrm{q\bar{q}'\bar{q}q'}$ events both have a doubly resonant Breit-Wigner structure in the $\vec{m}$-plane, modulated by a phase-space correction factor $PS(\vec{m}|\sqrt{s})$ due to the nearby kinematic limit $m_{W^+} + m_{W^-} \leq \sqrt{s}$. The probability density function component used to model four-fermion events is given by:

$$S(\vec{m}|\mathrm{M_W}, \Gamma_\mathrm{W}) = PS(\vec{m}|\sqrt{s})\cdot \\ \cdot\left[\frac{\tilde{\sigma}_s^{\mathrm{WW}}}{\tilde{\sigma}_s^{\mathrm{WW}}+\tilde{\sigma}_s^{\mathrm{ZZ}}} \cdot BW_{\mathrm{WW}}(\vec{m}|\mathrm{M_W}, \Gamma_\mathrm{W}) + \frac{\tilde{\sigma}_s^{\mathrm{ZZ}}}{\tilde{\sigma}_s^{\mathrm{WW}}+\tilde{\sigma}_s^{\mathrm{ZZ}}} \cdot BW_{\mathrm{ZZ}}(\vec{m}|\mathrm{M_Z}, \Gamma_\mathrm{Z})\right],$$

where $\tilde{\sigma}_s^{\mathrm{WW}}$ and $\tilde{\sigma}_s^{\mathrm{ZZ}}$ reflect the accepted cross-sections, calculated from simulation, of respectively the $\mathrm{W^+W^-}$ and the ZZ final states. These cross-sections are centre-of-mass energy dependent but are independent of the reconstructed event topology.

The two-dimensional Breit-Wigner distribution is approximated as the product of two one-dimensional Breit-Wigners:

$$BW_{\mathrm{WW}}(\vec{m}|\mathrm{M_W}, \Gamma_\mathrm{W}) = BW_\mathrm{W}(m_{W^+}|\mathrm{M_W}, \Gamma_\mathrm{W}) \cdot BW_\mathrm{W}(m_{W^-}|\mathrm{M_W}, \Gamma_\mathrm{W}),$$

with BW_W given by the expression in equation 5 of section 5.2.3. An expression of the same form is assumed for the ZZ component.

A dependence on the centre-of-mass energy is also introduced into $S(\vec{m}|\mathrm{M_W}, \Gamma_\mathrm{W})$ through the phase space correction factor $PS(\vec{m}|\sqrt{s})$:

$$PS(\vec{m}|\sqrt{s}) = \frac{1}{s}\sqrt{(s - m_{W^+}^2 - m_{W^-}^2)^2 - 4m_{W^+}^2 m_{W^-}^2}.$$

The combined density function is then constructed from the signal and background terms:

$$P(\vec{m}|\mathrm{M_W}, \Gamma_\mathrm{W}, \sqrt{s}) = P^{4f} \cdot S(\vec{m}|\mathrm{M_W}, \Gamma_\mathrm{W}, \sqrt{s}) + (1 - P^{4f}) \cdot B.$$

Utilising this probability density function, and the event ideogram, equation 6 may be used to calculate the event likelihood function. The extraction of the parameters of interest, $\mathrm{M_W}$ and Γ_W, from the event likelihood functions are discussed below.

5.4 Mass and Width Extraction

The mass and width of the W boson are extracted from maximum likelihood fits to data samples. This section describes this procedure, the calibration applied and the cross-checks of this method that have been performed.

The distribution of the reconstructed invariant masses of the selected events after applying a kinematic fit, imposing four-momentum conservation and the equality of the two di-jet masses, are shown in figure 8. This figure is provided for illustrative purposes only, the mass and width fitting procedure is described below.

The combined likelihood of the data can be obtained from the product of the event likelihoods described above. In practice this is achieved by performing the sum of the logarithms of the individual event likelihoods. The fitted data samples are divided by data taking year and applied event selection. For the mass fit the data from the fully-hadronic event selection and the electron, muon and tau semi-leptonic selections are all fitted separately. In the determination of the W width, where the relative precision is much worse, the data are divided only into fully-hadronic and semi-leptonic selection samples. The procedure for combining the results from each of these fits is discussed in section 7.

The W mass and width are extracted from maximum likelihood fits. The W mass fit is performed assuming the Standard Model value for the W width (2.11 GeV/c^2). The W width was obtained assuming a mass of 80.4 GeV/c^2. The correlation between $\mathrm{M_W}$ and Γ_W was found to have a negligible impact on the extracted mass and width value: the current uncertainty of 44 MeV/c^2 on Γ_W [32] gives rise to a 0.6 MeV/c^2 uncertainty in the extracted $\mathrm{M_W}$.

The terms used in the likelihood and described above are functions which approximate a description of the underlying physics and detector response. Hence, this approach necessitates a calibration of the analysis procedure. The calibration is performed using signal and background simulation events for which the true mass and width values are known. Rather than regenerating the events at a range of mass and width values, the calibration of the analysis uses reweighted events. The reweighting was performed using the extracted matrix element of the `WPHACT` and `YFSWW` generators. The reweighting procedure is cross-checked using independent simulation events generated at three W mass and width values. In the fully-hadronic channel where both the standard method and the cone-jet reconstruction technique are applied to the W Mass measurement, both analyses are calibrated separately: the illustrative values reported in this section are for the standard analysis.

A high statistics simulation sample is used to calibrate the analysis, comprised of an appropriate mixture of signal and background events. The result of the likelihood fit as a function of the simulated W mass is shown in figure 9 for the $\mu\overline{\nu}_\mu \mathrm{q\bar{q}'}$ channel analysis at $\sqrt{s} = 189$ GeV. The analysis has a linear behaviour in the mass window of interest, and the calibration curves are defined by two parameters :

- the slope of the generated mass against fitted mass line;
- the offset defined at a fixed reference point. This point is chosen to be the value used in our simulation; 80.4 GeV/c^2 for the mass and 2.11 GeV/c^2 for the width.

The slopes at different energies are found to be compatible, and their mean values are respectively 0.984 ± 0.013, 0.993 ± 0.006 and 0.963 ± 0.013 in the $\mathrm{e}\overline{\nu}_\mathrm{e}\mathrm{q\bar{q}'}$, $\mu\overline{\nu}_\mu\mathrm{q\bar{q}'}$ and $\tau\overline{\nu}_\tau\mathrm{q\bar{q}'}$ analyses. In the $\mathrm{q\bar{q}'\bar{q}q'}$ analysis the slope was compatible with unity to within 2% at all centre-of-mass energies and no slope calibration was applied.

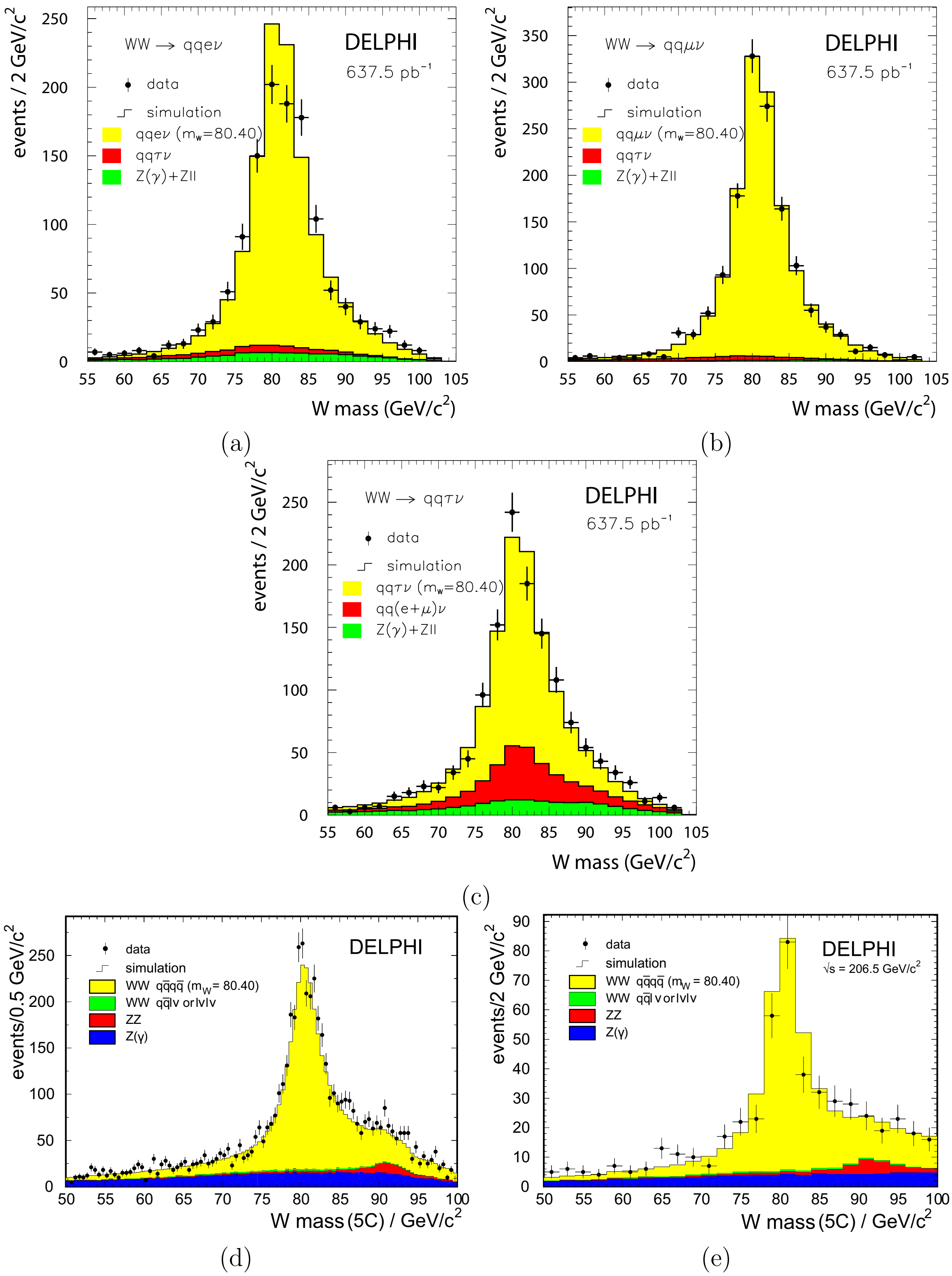

Figure 8: The distribution of the reconstructed W masses from a kinematic fit with five constraints imposed in the (a) $\mathrm{e}\overline{\nu}_\mathrm{e}\mathrm{q}\bar{\mathrm{q}}'$, (b) $\mu\overline{\nu}_\mu\mathrm{q}\bar{\mathrm{q}}'$, (c) $\tau\overline{\nu}_\tau\mathrm{q}\bar{\mathrm{q}}'$ and (d) and (e) $\mathrm{q}\bar{\mathrm{q}}'\bar{\mathrm{q}}\mathrm{q}'$ analysis channels at all energies. (d) shows the data sample taken at all energies until September 2000, the data taken after that with a damaged TPC sector is shown in (e). In (d) and (e) only the jet pairing with the highest probability is included in the figures. The simulation samples have been normalised to the same integrated luminosity as the data.

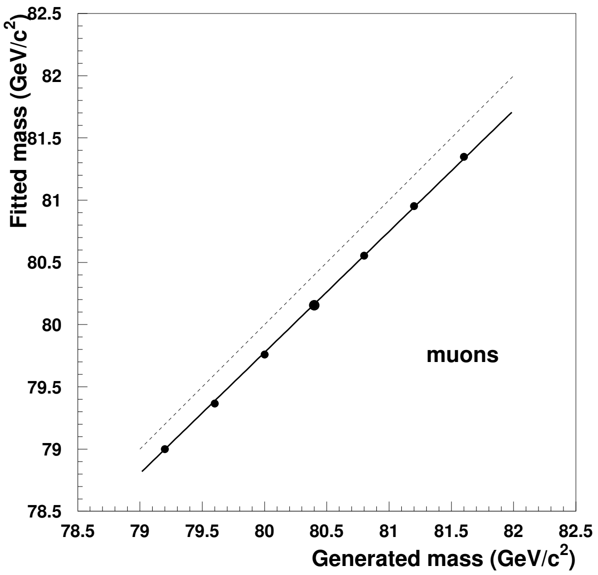

Figure 9: W mass calibration curve in the $\mu\overline{\nu}_\mu q\bar{q}'$ channel at $\sqrt{s} = 189$ GeV. The dashed line indicates the result that would be obtained without any analysis bias.

The highly linear behavior, with a value of the slope close to unity is an *a posteriori* justification of the fitting functions used in the likelihood fit and described in section 5.3.3. The remaining effects not taken into account by these fitting functions give rise to the offset. As an example, the calibration offsets at $\sqrt{s} = 189$ GeV are respectively -0.108 ± 0.012, -0.215 ± 0.010, -0.252 ± 0.015 and -0.222 ± 0.006 GeV$/c^2$ in the $e\overline{\nu}_e q\bar{q}'$, $\mu\overline{\nu}_\mu q\bar{q}'$, $\tau\overline{\nu}_\tau q\bar{q}'$ and $q\bar{q}'\bar{q}q'$ analyses for the mass. The offsets vary slightly with the centre-of-mass energy.

The same procedure is also applied for the W width analyses. In the $\ell\overline{\nu}_\ell q\bar{q}'$ channel a slope of 0.894 ± 0.008 is obtained independent of the centre-of-mass energy and the offset at $\sqrt{s} = 189$ GeV was $+0.065 \pm 0.015$ GeV$/c^2$. However, in the $q\bar{q}'\bar{q}q'$ analysis the slope is found to be dependent on the centre-of-mass energy, the slopes at $\sqrt{s} = 189$ GeV and 205 GeV are approximately 1.1 and 1.2 respectively and furthermore the relation between the reconstructed and generated Γ_W is not perfectly linear. Hence the offset is parameterised as a function of the generated W width and the centre-of-mass energy. The calibration offset at $\sqrt{s} = 189$ GeV is 183 ± 13 MeV$/c^2$ at the reference width.

The analyses are corrected with these calibration results, and the statistical error on the offset is included in the systematic error (see below).

After applying the calibration procedure, the consistency of the analyses is checked. Sets of simulation events, with a sample size the same as the data, containing the expected mixture of signal and background events were used to test the analyses. Figure 10 shows error and pull plots from analysing 20000 or more such samples, where the pull is defined as

$$\text{pull} = \frac{(M_{W\text{fit}} - M_{W\text{gen}})}{\sigma_{\text{fit}}},$$

here the subscript 'fit' and 'gen' distinguish the result from the calibrated analysis fit and the generated parameter in the simulation respectively. The σ_{fit} is the error estimated by the analysis. This error has been scaled in the analysis to obtain a Gaussian width of one for the pull distributions, as shown in the plots. These plots were produced at all centre-of-mass energies for both parameters. The error distributions in figure 10 also demonstrate that this quantity is in good agreement with the value obtained from the data.

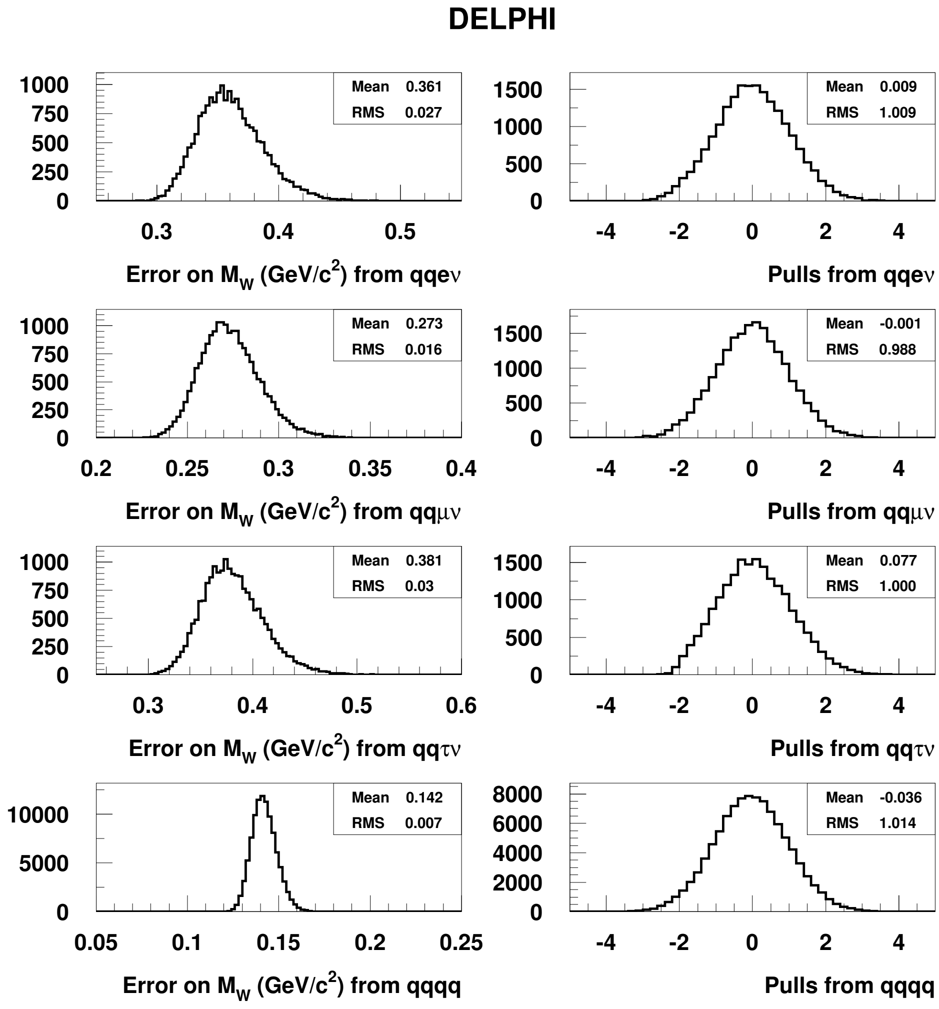

Figure 10: The errors (left) and pulls (right) of the W mass fits for each semi-leptonic analysis channel and the fully-hadronic channel. These plots were obtained using simulated event samples with the same statistics as the data sample collected at 200 GeV. The errors obtained on the fits to the data samples were 365 MeV$/c^2$ for the $\mathrm{e}\overline{\nu}_\mathrm{e}\mathrm{q}\bar{\mathrm{q}}'$ analysis, 282 MeV$/c^2$ for $\mu\overline{\nu}_\mu\mathrm{q}\bar{\mathrm{q}}'$, 438 MeV$/c^2$ for $\tau\overline{\nu}_\tau\mathrm{q}\bar{\mathrm{q}}'$ and 149 MeV$/c^2$ for the standard $\mathrm{q}\bar{\mathrm{q}}'\bar{\mathrm{q}}\mathrm{q}'$ analysis.

6 Systematic Uncertainties

The sources of systematic error that have been considered for the W mass and width determinations are described in the subsections below. The results of these studies at example centre-of-mass energies are summarised in tables 14, 15 and 16. In the fully-hadronic channel the standard method and the cone jet reconstruction technique have been applied as described in section 5.3.2. The systematic uncertainties are in agreement between these two techniques except for the error sources from final state interactions (FSI), where separate values for the two techniques are given.

6.1 Calibration

The analysis calibration procedure is described above in section 5.4. The accuracy with which the offset of the analyses can be determined is limited by the size of the generated simulation samples. Sufficient events were generated to limit this error to 5% or less of the statistical error on the mass or width determination in any given channel.

6.2 Detector Effects - Muons

Contributions to the systematic error on the W mass and width due to the reconstruction of muons are considered in this section. These were evaluated using the $Z \to \mu^+\mu^-$ events collected at the Z peak during the LEP2 period. The systematic uncertainties determined by these studies for the W mass analysis are presented in table 3.

Inverse Momentum Scale

The primary sources of systematic error on the muon momentum scale are the detector alignment or possible reconstruction distortions (particularly in the TPC). As a result of these effects, we may also anticipate an opposite bias on the measured track curvature for positive and negative muons.

Corrections to the inverse momentum scale, $1/p$, are calculated from the selected $\mu^+\mu^-$ samples. The mean inverse momentum, $< 1/p >$, is calculated separately for positive and negative muons in different bins of the polar angle, and a correction for the positive muons is defined as

$$\frac{1}{2}(< \frac{1}{p-} > - < \frac{1}{p+} >), \tag{7}$$

with the opposite sign correction applied to negative muons. These corrections are typically of the order 1 to 2×10^{-4} GeV^{-1}c, except in the polar angle regions at the junction between the barrel and endcaps where the correction can reach 10^{-3} GeV^{-1}c in the worst case. In the simulation this correction is, as expected, compatible with zero. After applying the corrections $< 1/p >_{data}$ and $< 1/p >_{simulation}$ are found to be in agreement within 0.2%, and this value is used to calculate the systematic on the muon inverse momentum scale. The systematic uncertainty on the positive and negative muon inverse momentum scale difference is estimated by varying the correction by $\pm 50\%$ of its value.

Inverse Momentum Resolution

The momentum resolution (typically 0.001 GeV^{-1}c in $1/p$) was found to be commonly around 10% better in simulation events than in the data. This discrepancy, determined for all years of LEP2 and polar angle regions, is corrected by smearing the simulation with a Gaussian. An additional smearing of ± 0.0003 GeV^{-1}c in $1/p$ is used to estimate the systematic error resulting from this correction. This systematic does not affect the M_W

determination but is a small component of the Γ_W measurement uncertainty for events containing muons.

6.3 Detector Effects - Electrons

Contributions to the systematic error on the W mass and width due to the reconstruction of electrons are considered in this section. These were evaluated using the Bhabha and Compton events collected at the Z peak and high energies during the LEP2 period. The systematic uncertainties determined by these studies for the W mass analysis are presented in table 3.

Energy Scale

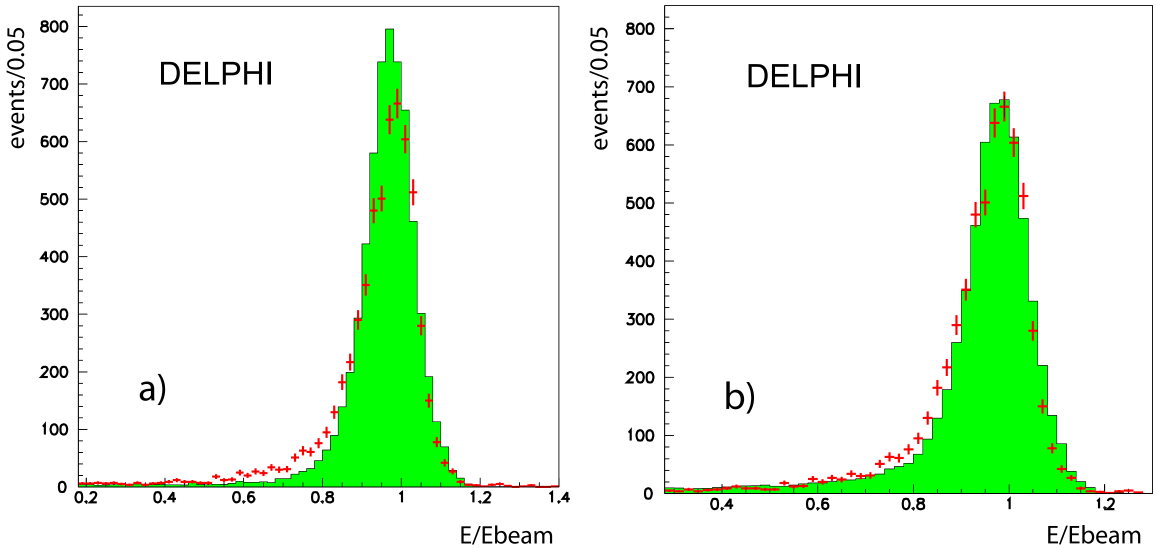

Figure 11: The ratio E/E_{beam} for electrons in the endcaps from Bhabha events recorded at the Z peak in 1998. The shaded histogram is the simulation and the points are the data. Plot (a) shows the raw distribution, while plot (b) gives this after the bremsstrahlung correction discussed in the text. The resolution correction (see text) has also been applied.

The reconstructed energy of electrons was compared between data collected at the Z peak and fully simulated samples of Bhabha events. In the barrel region of the detector the data and simulation are in good agreement. However, in the forward directions a slight difference is observed between the data and simulation (see figure 11) and attributed to an under-estimation of the quantity of material in the simulation before the electromagnetic calorimeter in the DELPHI endcaps. A correction is applied to the simulation by introducing the effect of extra bremsstrahlung emission corresponding to an additional 3% of a radiation length. Following [33], the probability w that an electron of initial energy E_0 has an observed energy between E and E+dE after traversing a thickness of t radiation lengths is

$$w(E_0, E, t)dE = \frac{dE}{E_0}\frac{[ln(E_0/E)]^{(t/ln2)-1}}{\Gamma(t/ln2)}. \quad (8)$$

For each event, the corrected energy E is chosen randomly according to the distribution w. The optimal value of the parameter t was adjusted from the data and simulation comparison.

After the endcap correction was applied, good agreement between data and simulation was obtained throughout the detector. The residual systematic error on this absolute energy scale is estimated to be ±0.3% of the measured energy and is estimated from the selection cut stability and statistical precision of the data and simulation comparison.

Energy Resolution

The resolution on the reconstructed electron energies was also compared between the data and simulation Bhabha samples. The agreement is improved by applying a Gaussian smearing to the simulation with a width varying between 1 and 2% of the measured electron energy in the barrel, and 2 to 4% in the endcaps, depending on the year of data taking. The systematic error on this smearing Gaussian width is estimated to be ±1% of the measured energy. This systematic does not affect the M_W determination but is a small component of the Γ_W measurement uncertainty for events containing electrons.

Energy Linearity

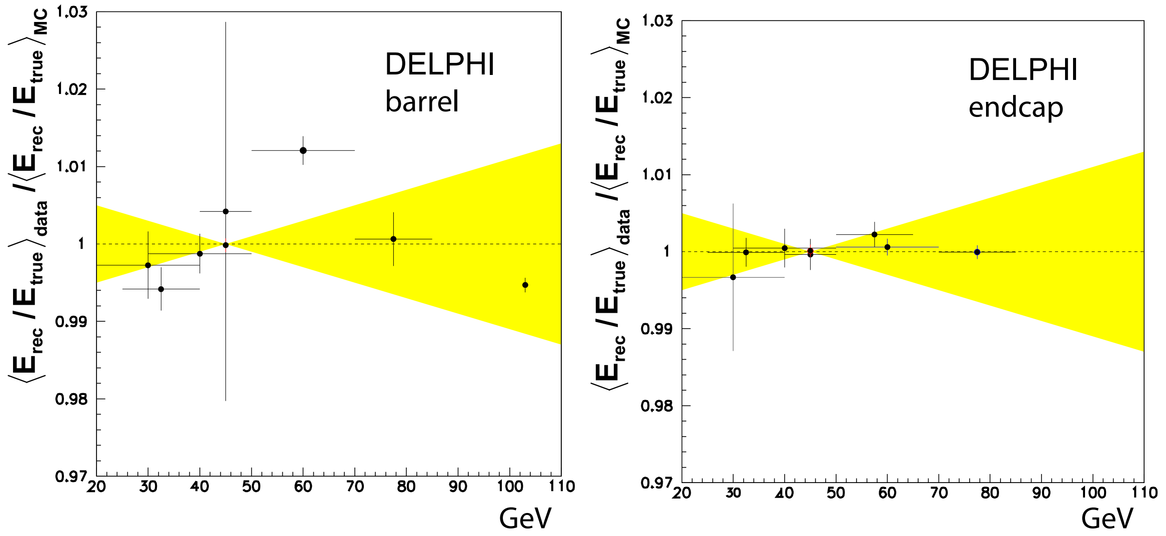

Figure 12: The double ratio of reconstructed and true average energy values in data and simulation, $\langle E_{rec}/E_{true} \rangle_{data}/\langle E_{rec}/E_{true} \rangle_{MC}$, for data taken in 2000. The shaded area represents the quoted systematics due to a possible dependence of the energy calibration with the electron energy. The left hand plot is for electrons observed in the barrel electromagnetic calorimeter and the right hand plot for electrons in the endcap. Note that, by construction, the Bhabha point at 45 GeV is at one.

The reconstructed electron energy was also studied as a function of the true energy. The Z peak and high energy running provided high statistic Bhabha samples with which to study electrons of 45 GeV and above 100 GeV energy. For these samples the "true" electron energy is taken from the beam energy. The reconstructed electron energy was also checked using low energy electrons from Compton events at the Z peak, and high energy electrons from radiative Bhabha scattering at high centre-of-mass energy. In these cases the true energy of the lepton is deduced from 3-body kinematics using only the angular information and assuming that the unseen particle was along the beam axis. Figure 12 shows the compatibility of the reconstructed electron energy in data and simulation, only statistical errors are shown. One of the three points measured for radiative Bhabhas in the Barrel shows a discrepancy but this effect is not confirmed by the better measured high energy (non-radiative) Bhabha point, whereas physical calibration problems such as threshold effects or leakage in the calorimeter would be expected to increase in size with energy. Hence, no additional corrections are applied. A systematic error is estimated assuming a deviation of the energy calibration slope $E_{data}/E_{simulation}$ versus $E_{simulation}$ of 1% over the range 25 to 70 GeV. These values approximately correspond to the relevant energy range for the observed electrons in the analysis.

6.4 Detector Effects - Taus

The $\tau\overline{\nu}_\tau q\bar{q}'$ channel differs from the other W^+W^- semi-leptonic decay channels as these events contain two (or three for leptonic tau decays) neutrinos in the final state. Thus, the mass of the event can be determined only from the decay products of the other W. As a result the lepton systematics described in the preceding sections are not relevant to the $\tau\overline{\nu}_\tau q\bar{q}'$ channel. The only relevant systematic involving the tau decay products arises from uncertainties in the assignment of the reconstructed tracks between the tau product and the hadronically decaying W. This effect is small compared with the overall uncertainty on the jet energy and direction, the systematic on which is considered in the sections below.

M_W Lepton Correction Systematic Errors (MeV/c^2)		
Sources of Systematic Error	$e\overline{\nu}_e q\bar{q}'$ 189 GeV	$e\overline{\nu}_e q\bar{q}'$ 205 GeV
Electron Energy Scale	18	22
Electron Energy Resolution	-	-
Electron Energy Linearity	16	11
	$\mu\overline{\nu}_\mu q\bar{q}'$ 189 GeV	$\mu\overline{\nu}_\mu q\bar{q}'$ 205 GeV
Muon 1/p Scale	16	21
μ^+ μ^- 1/p Difference	1	4
Muon 1/p Resolution	-	-

Table 3: Contributions to the systematic error on the W mass measurement at 189 and 205 GeV related to the lepton reconstruction. The uncertainties on each of these numbers is typically 3 MeV/c^2.

6.5 Jet Description

Jets are composite objects, and the detector and analysis response to them can be dependent on their internal structure. Therefore it is not straightforward to separate in a clean way uncertainties arising from the modelling of the detector in the simulation from those due to the theoretical description of the jet structure.

Moreover this description is not based on exact calculations, whose uncertainty can be in principle reasonably well estimated, but on phenomenological models tuned to best reproduce the data at the Z peak: the Lund model as implemented in `PYTHIA` is the standard choice for this analysis. In this situation the comparison of different models may be a useful tool to understand which parts of the fragmentation description the measurement is sensitive to, but only a direct comparison of the chosen model with well understood data samples, in particular Z hadronic decays, can give the ultimate estimate of the uncertainty from the observed data-simulation disagreements.

The jet studies performed are described in the text below and the corresponding jet correction systematic errors are provided in table 4. The most relevant jet characteristics were calibrated on real data control samples, and uncertainties on these calibrations are propagated through the analysis.

Energy Scale

The absolute jet energy scale was studied in on-peak Z $\rightarrow q\bar{q}$ decays, by comparing the reconstructed energies, E_{rec}, in data and simulation in selected two jets events. The $b-$tagging technique is used to remove b quark jets which are essentially not present in W^+W^- decays. The true jet energy in these events is assumed to be the beam energy E_{beam}, under the assumption that the bias introduced by QED ISR is described with negligible error in the simulation (the `KK2f` generator was used for these events). The double ratio of average values $\langle\ E_{rec}/E_{beam}\ \rangle_{data}/\langle\ E_{rec}/E_{beam}\ \rangle_{MC}$ was evaluated as a function of the jet polar angle and applied as a scale factor correction to the four-momentum components of the jet in simulated events. The correction value depends on the year as well as the angular region, with the deviation from unity ranging typically from a few per mille up to 3-4% in the most forward region.

The systematic uncertainty on this correction is determined by the limited on-peak Z statistics, and it is estimated to be $\pm 0.3\%$.

Energy Resolution

The same event sample used to study the jet absolute energy scale was also used to calibrate the jet energy resolution in the simulation. A Gaussian smearing was determined from the data and is applied to the simulated jet energy with a magnitude dependent on the ratio of the reconstructed and true jet energies. This procedure takes into account the asymmetric shape of the jet energy observable. When applying the correction to the simulated W^+W^- events an estimate of the true jet energy is required. When the event is reconstructed with two jets from each hadronically decaying W, the generated quark energies are used. However, when gluon radiation has given rise to an additional jet the true jet energy estimate is determined by applying the same clustering algorithm as used in the analysis to the simulated partons prior to the detector simulation. In both cases the association of the true and reconstructed jets is performed according to geometric criteria.

The average resolution correction ranges from 4.5% of the jet energy in the barrel to 6.6% in the endcaps. The correction is also dependent on the year. The systematic uncertainty on the correction is estimated to be $\pm 2\%$ of the jet energy.

Energy Linearity

The dependence of the energy calibration as a function of the jet energy was checked using low energy jets from $q\bar{q}$ + gluon events at the Z peak and high energy jets from $e^+e^- \rightarrow q\bar{q}$ decays at high energy.

In the first case, the true jet energy is determined using three-body massless kinematics. The jet energy range used in this study is restricted to the region where the data and simulation true energy distributions do not show sizeable discrepancies. This energy selection avoids introducing an unnecessary sensitivity in this analysis to the modelling of hard gluon radiation in the simulation.

In the second high-energy jet case the effective hadronic mass $\sqrt{s'}$ is required to be such that $\sqrt{s'/s} > 0.95$. The true jet energy is then again determined using three-body massless kinematics but now the third object is an hypothetical ISR photon emitted along the beam pipe. The difference between the estimated jet energy and the nominal beam energy is constrained to be smaller than 10 GeV.

A jet energy linearity slope in $E_{data}/E_{simulation}$ versus $E_{simulation}$ is then determined. The study was performed separately in the barrel and endcap regions of the detector and for each data taking year. The results from the different data taking years are compatible within statistical errors. The study showed agreement in the slope at typically the 0.5% level over the range 25 to 75 GeV, and this deviation value is used to determine the systematic uncertainty.

Angular Bias

As reported in [9], the reprocessing of data and simulation used for this analysis has a noticeable excess of tracks at low polar angles (forward tracks) in data as compared to the simulation. The most likely cause of this effect is an underestimation in the simulation of the track reconstruction efficiency for low-momentum particles at low polar angle.

This effect introduces a small bias in the distribution of the jets' reconstructed polar angle in the simulation compared with data. In order to evaluate the effect of such a bias, a systematic shift of the jets' polar angle is applied to the simulation. The shift as a function of the polar angle itself has been determined using on-resonance Z hadronic decays, and is found to have the form $0.008\cos{\theta_j}^{5.3}$ where $0 < \theta_j < \pi/2$ is the polar angle of the jet. The corresponding W mass and width shifts have been evaluated and symmetric systematic errors of these values applied. The W mass uncertainty is reported in table 4.

Angular Resolution

A study of the acollinearity of jets in on-peak $Z \rightarrow q\bar{q}$ events was performed and appropriate smearings to the simulation of the jet angular direction, dependent on the polar angle of the jet, were estimated. The smearings on the polar angle are typically 5 mrads. A systematic error is estimated by applying an extra 5 mrad angular smearing.

Jet Mass

The jet mass is known not to be exactly described in the simulation; both inaccuracies in the fragmentation description (related to the jet breadth due to soft and hard gluon radiation) and imperfections in the modelling of the detector response (reconstruction efficiencies and noise) are responsible for these discrepancies. However, only those data-simulation differences in the jet mass which are not compensated by differences in the inter-jet angle are relevant for the systematic uncertainty, since these cause systematic biases in the reconstructed W mass.

For this reason the fragmentation-induced differences are only marginally relevant for the mass measurement. Furthermore, the calibration procedure adopted, in particular for the energy and angular smearing, corrects for most of the effects given by the differences in jet breadth. The jet breadth is relevant as broader jets are worse reconstructed: they are detected with larger uncertainties on the jet direction; are likely to lose more energy due to the imperfect hermeticity of the detector; and cause more confusion in the jet clustering.

The jet correction procedure described above, as well as the constrained kinematic fit, modifies all the four-momentum components of the jet but leaves unchanged the jet boost, i.e. the E/m ratio. It is therefore useful to study this observable, instead of the simple jet mass.

Detector noise is a source of data-simulation discrepancy which clearly biases the reconstructed boson mass, since it changes the mass and boost of the jets while leaving, on average, the inter-jet angle unchanged. Significant data-simulation differences in low energy neutral clusters, both in the electromagnetic and hadronic calorimeters, are attributed primarily to an imperfect noise description, while the discrepancies in the charged particles of jets are considered to be almost entirely due to the modelling of the fragmentation.

The average effect of removing low energy neutrals below 2 GeV on the jet m/E was evaluated as a function of the polar angle and of the m/E of the jet itself, since the impact of the noise depends on the breadth of the jet. The expected effect on the neutrals from fragmentation was subtracted. The fragmentation effect was obtained from charged particles, suitably scaled for the relative neutral and charged particle multiplicity.

This m/E effect was then propagated in the full analysis chain to extract the relative systematic uncertainty on the full mass and width measurements.

M_W Jet Correction Systematic Errors (MeV/c^2)				
Sources of Systematic Error	189 GeV			
	$e\overline{\nu}_e q\bar{q}'$	$\mu\overline{\nu}_\mu q\bar{q}'$	$\tau\overline{\nu}_\tau q\bar{q}'$	$q\bar{q}'\bar{q}q'$
Energy Scale	8	6	11	8
Energy Resolution	3	3	5	9
Energy Linearity	12	9	12	16
Angular Bias	3	5	5	2
Angular Resolution	-	-	-	8
Jet Mass	9	8	8	10
	205 GeV			
	$e\overline{\nu}_e q\bar{q}'$	$\mu\overline{\nu}_\mu q\bar{q}'$	$\tau\overline{\nu}_\tau q\bar{q}'$	$q\bar{q}'\bar{q}q'$
Energy Scale	11	9	16	8
Energy Resolution	8	5	8	10
Energy Linearity	15	11	20	8
Angular Bias	9	8	7	19
Angular Resolution	-	-	-	1
Jet Mass	13	12	17	13

Table 4: Contributions to the systematic error on the W mass measurement at 189 and 205 GeV related to jet reconstruction. The uncertainties on each of these numbers is typically 6 MeV/c^2.

Fragmentation Model

The effect of using different hadronisation models on the analysis was studied by replacing the standard choice, `PYTHIA`, with both the `ARIADNE` and `HERWIG` models, each tuned by DELPHI to best match experimental data. The mass and width shifts were evaluated at 189 GeV and 207 GeV centre-of-mass energies and are reported in tables 5 and 6. Detailed studies performed at the Z peak showed that for several observables all the models showed disagreements with the data and that these disagreements were all in the same direction: the jet mass variable, discussed in the previous paragraph, is a clear example. Hence the results of the hadronisation model comparison were used only to investigate the sensitivity of the analysis to specific features of the models, and not used directly as an evaluation of the systematic uncertainty due to the choice of model.

	ΔM_W MeV/c^2			
	$e\overline{\nu}_e q\bar{q}'$	$\mu\overline{\nu}_\mu q\bar{q}'$	$\tau\overline{\nu}_\tau q\bar{q}'$	$q\bar{q}'\bar{q}q'$
HERWIG - PYTHIA	-7 ± 10	-16 ± 9	-17 ± 13	-9 ± 5
ARIADNE - PYTHIA	-11 ± 9	-12 ± 9	-10 ± 12	-15 ± 5

Table 5: Effect of different fragmentation models on the W mass determination.

	$\Delta\Gamma_W$ MeV/c^2	
	$\ell\overline{\nu}_\ell q\bar{q}'$	$q\bar{q}'\bar{q}q'$
HERWIG - PYTHIA	$+46 \pm 13$	-2 ± 11
ARIADNE - PYTHIA	-9 ± 15	$+1 \pm 11$

Table 6: Effect of different fragmentation models on the W width determination.

The biggest difference was found to be between `PYTHIA` and `HERWIG`, and was shown to be largely due to the different production rates of heavy particles, mainly kaons, protons and neutrons. At parton level these differences modify not only the jet masses but also change the jet-jet angles accordingly, leaving the bosons invariant masses unchanged. However, the reconstruction and analysis procedure breaks this compensation since in the fully-hadronic event reconstruction all charged particle tracks are assigned the pion mass, and all neutrals are assumed to be massless (photon-like). In the semi-leptonic analysis, the nominal masses are used in the jet reconstruction for those particles with a positive identification, i.e. for charged kaons and protons identified by the RICH and for K^0_S and Lambdas reconstructed as secondary vertexes from their decay products [10].

The `HERWIG` version used, although tuned to best reproduce the Z peak DELPHI data, is known to describe the particle production rates poorly. This is especially the case for baryons, therefore using `HERWIG` accentuates this particle mass assignment effect. Generally the measured particle rates are closer to those in `PYTHIA` and `ARIADNE`. Reweighting in the models the production rates of the most abundant heavy particles species, kaons and protons, reduces the disagreement among the different models, bringing it to the level of the statistical uncertainty of the fit. Tables 7 and 8 show the residual discrepancies obtained between the models after they have been reweighted to the `PYTHIA` values. The component of the fragmentation systematic error which is not due to the heavy particle multiplicity effect is obtained from these numbers. The largest value - either the central value or its uncertainty - from either model is taken as the systematic error estimate.

The component of the fragmentation error that is due to the heavy particle rate was also evaluated for the W mass analysis; this small component of the error is neglected for the W width analysis. The W mass shift was evaluated between the DELPHI tune of `PYTHIA` and the same events reweighting to the measured particle rates $\pm 1\sigma$ of their uncertainty. The average of the modulus of the two shifts is reported in table 9 and is taken as the estimate of the fragmentation error due to the heavy particle multiplicity.

The combined fragmentation error was evaluated for the W mass by adding the particle reweighting effects and the model variation uncertainty in quadrature. This fragmentation error is listed separately from the other jet description uncertainties in the systematic uncertainty summary tables 14, 15 and 16.

	ΔM_W MeV/c^2			
	$e\overline{\nu}_e q\bar{q}'$	$\mu\overline{\nu}_\mu q\bar{q}'$	$\tau\overline{\nu}_\tau q\bar{q}'$	$q\bar{q}'\bar{q}q'$
HERWIG Rew. - PYTHIA	-2 ± 10	-8 ± 9	-5 ± 13	-11 ± 6
ARIADNE Rew. - PYTHIA	-10 ± 9	-10 ± 9	-10 ± 12	-1 ± 4

Table 7: Effect of different fragmentation models on the W mass determination, after reweighting the heavy particle species rates in the Monte Carlo simulations to the measured rates.

	$\Delta\Gamma_W$ MeV/c^2	
	$\ell\overline{\nu}_\ell q\bar{q}'$	$q\bar{q}'\bar{q}q'$
HERWIG Rew. - PYTHIA Rew.	$+29 \pm 13$	$+3 \pm 8$
ARIADNE Rew. - PYTHIA Rew.	-11 ± 15	-1 ± 8

Table 8: Effect of different fragmentation models on the W width determination, after reweighting the heavy particle species rates in the Monte Carlo simulations to the measured rates.

6.6 Mixed Lorentz Boosted Zs

An alternative method of evaluating the jet description systematic is to use the technique of mixed Lorentz boosted Zs (MLBZ). This method attempts to emulate W^+W^- events using two on-peak Z events. The emulated W^+W^- events are constructed both from simulated events and the large statistics sample of Z peak data events. Standard W mass and W width analyses can then be performed on these event samples. Hence, the MLBZ method provides a direct comparison between data and the simulation model of choice. The difference between the measurements made from the data and simulation MLBZs can be interpreted as primarily providing a statistically sensitive cross-check of the fragmentation systematic assigned to the W mass and width measurements. This method would also identify some sources of detector modelling error.

	ΔM_W MeV/c^2			
Particle Type	$e\overline{\nu}_e q\bar{q}'$	$\mu\overline{\nu}_\mu q\bar{q}'$	$\tau\overline{\nu}_\tau q\bar{q}'$	$q\bar{q}'\bar{q}q'$
$K^\pm$	0.1 ± 0.3	0.9 ± 0.3	1.5 ± 0.4	0.2 ± 0.5
Proton	2.0 ± 0.4	1.5 ± 0.3	3.2 ± 0.5	3.5 ± 0.5

Table 9: Effect on the W mass of reweighting the heavy particle species rates in the Monte Carlo simulations. The mass shifts were evaluated between the DELPHI tune of PYTHIA and versions reweighted to 1 sigma above and below the measured particle rates. The shift value reported is the average of the modulus of these two shifts. The measured charged multiplicity in a Z peak event for kaons is 2.242 ± 0.063 [32], whereas for protons the measured multiplicity is 1.048 ± 0.045 [32].

A $W^+W^- \rightarrow f\bar{f}'\bar{f}f'$ event is emulated by selecting two Z events and rotating and Lorentz boosting them so that their superposition reflects a true W^+W^- event. The mixture of quark species will not be the same as in true W^+W^- events, it will however be the same between the data and simulated Z samples that are used in the comparison. To emulate a $q\bar{q}'\bar{q}q'$ event two hadronically decaying Z events were used. To emulate a $\ell\overline{\nu}_\ell q\bar{q}'$ event one Z decaying into hadrons and one Z decaying into charged leptons was used. One hemisphere of the $Z\rightarrow l^+l^-$ decay is removed to represent the $W\rightarrow\ell\overline{\nu}_\ell$ decay. The emulation process is performed by manipulating the reconstructed tracks and calorimeter energy clusters.

A realistic distribution of W^+W^- events is obtained by using event templates. The four momenta of the four primary fermions in a WPHACT W^+W^- event are used as the event template. The Z events are chosen such that they have a thrust axis direction close to the polar angle of one of the W fermions. This ensures that the distribution in the detector of the tracks and energy clusters selected in the Z event follows that expected in W^+W^- events. Each of the template Ws is then boosted to its rest frame. The particles in a final state of a selected Z event are rotated to match the rest-frame direction of the fermions from the template W. The energy and momentum of the Z events are then rescaled to match the kinematic properties of the W boson decay. The two Z events are then each boosted into the lab frame of the template W^+W^- event and mixed together. The same W^+W^- event templates are used for the construction of both the data and Monte Carlo simulation MLBZ events, thus increasing the correlation between both emulated samples.

Tests were performed to confirm the reliability of the MLBZ method in assessing systematic errors. MLBZs were produced using Zs with the PYTHIA, HERWIG and ARIADNE models and the observed mass shifts were compared and found to agree with the statistically limited mass shifts observed in W^+W^- simulation events. A significant mass shift (300 MeV/c^2) was introduced by using the cone rejection algorithm (discussed in section 5.3.2) for the W mass measurement in the $q\bar{q}'\bar{q}q'$ channel. The real and simulated MLBZs and W^+W^- events agreed on the estimated size of the mass shift between the standard and cone estimators at the 15% level.

The MLBZ method was used to create emulated W^+W^- event samples. The Z events were selected from data recorded during the LEP2 calibration runs of the same year or from the corresponding Monte Carlo simulation samples. Values for the M_W and Γ_W estimators were determined separately for the data and simulation samples. This method has been applied on a cross-check analysis in the semi-leptonic channels and to the standard fully-hadronic analysis. The results from the fully-hadronic analysis are shown in Table 10. The semi-leptonic cross-check analysis applied the MLBZ procedure to the W mass determination separately in the electron, muon, and tau channels with uncertainties of around 8 MeV/c^2 being obtained and the results being compatible with the systematic uncertainties quoted in this paper. The MLBZ method provides a useful cross-check of the size of the systematic uncertainty arising from fragmentation and other jet description errors reported in the previous section. From the values obtained from the MLBZ method we conclude that the systematic uncertainties have not been significantly underestimated.

6.7 Electroweak Radiative Corrections

The measurements of the W mass and width described in this paper rely upon the accuracy of the event description provided by the simulation. Hence, the modelling

	$\sqrt{s}$ GeV	ΔM$_W$ MeV/c^2	$\Delta\Gamma_W$ MeV/c^2
MLBZ			
$q\bar{q}'\bar{q}q'$ Data - PYTHIA	206.5	-7.9 $\pm$ 4.9	20.1 $\pm$ 10.5

Table 10: Results obtained with the MLBZ method (see text).

accuracy of the electroweak radiative corrections implemented in the event generator is a source of systematic uncertainty.

The radiative corrections for 4-fermion events are described in [13] and in section 4.2. For W^+W^- (CC03) events, the signal used in this analysis, the corrections are based on YFSWW [17] and the effect of the theoretical uncertainties in it on the W mass measurement were initially studied in [34] at pure event generator level.

In [35] this study has been performed in the context of the full DELPHI simulation and analysis procedure; furthermore the main uncertainties due to non-CC03 4-fermion background events have been studied. Radiative corrections uncertainties on non 4-fermion background events are included in the uncertainty estimated on the background.

Several categories of uncertainty sources have been studied, which are considered here in turn.

W^+W^- Production: Initial State Radiation (ISR)

ISR plays a key role in the W mass analysis as it is one of the main sources of the bias on the fitted result with respect to the true value. This bias, which is removed by calibrating the fits with the simulation, is due to the energy-momentum conservation constraint used in the kinematical constrained fits. The ISR is computed in the YFS exponentiation approach, using a leading logarithm (LL) $\mathcal{O}(\alpha^3)$ matrix element.

The difference between the best result, obtained from implementing the $\mathcal{O}(\alpha^3)$ ISR matrix element, and the $\mathcal{O}(\alpha^2)$ one provides an estimate of the effect of missing the matrix element for higher orders. The missing higher orders lead to the use of a wrong description for events with more than three hard photons or more than one photon with high p_t.

The difference between the best result and the $\mathcal{O}(\alpha)$ result includes the previous study, and can be used as an estimate of the upper limit of the effect of missing the non-leading logarithm (NLL) terms at $\mathcal{O}(\alpha^2)$; this effect of missing NLL terms is expected to be smaller than the effect from the LL terms given by this $\mathcal{O}(\alpha^3)$ to $\mathcal{O}(\alpha)$ difference.

Also taking into account the study performed in [34], the ISR related uncertainty can be conservatively estimated at 1 MeV/c^2 for the mass and 2 MeV/c^2 on the width.

W Decay: Final State Radiation (FSR)

The FSR description and uncertainty is tightly linked to the final state considered. QED FSR from quarks is embedded in the parton shower describing the first phase of the hadronisation process. It is therefore essentially impossible to separate it from the rest of the hadronisation process, and the related uncertainty is considered as included in the jet and fragmentation related systematics.

FSR from leptons is described by PHOTOS. The difference between the best result, based on the NLL treatment, and the LL one can give an estimate of the effect of the missing part of the $\mathcal{O}(\alpha)$ FSR correction. While the result depends on the semi-leptonic channel, the difference is always less than 1 MeV/c^2.

In [34] the effect of the missing higher orders beyond $\mathcal{O}(\alpha^2)$ has been found to be negligible at generator level. Simple perturbative QED considerations suggest that the size of the effect should not exceed the size of the effect from the missing part of the $\mathcal{O}(\alpha)$ FSR correction; therefore conservatively the 1 MeV/c^2 can be doubled to take into account both of these components of the uncertainty.

Non-factorizable QED Interference: NF $\mathcal{O}(\alpha)$ Corrections

Non-factorizable $\mathcal{O}(\alpha)$ QED interference between Ws is effectively implemented through the so-called Khoze-Chapovsky [36] (KC) ansatz.

The effect of using the KC ansatz with respect to the Born calculation, where this interference is not described, can be considered as an upper limit of the missing part of the full $\mathcal{O}(\alpha)$ calculation and of the higher order terms. A dedicated study shows that the effect is less than 2 MeV/c^2 for all the measurements.

Ambiguities in Leading Pole Approximation (LPA) definition: Non Leading (NL) $\mathcal{O}(\alpha)$ Corrections

Two sources of uncertainties are considered, following the study in [34]. The effect of missing higher orders can be, at least partly, evaluated by changing the electroweak scheme used in the $\mathcal{O}(\alpha)$ calculation. This essentially means changing the definition of the QED fine structure constant used in the $\mathcal{O}(\alpha)$ matrix element. The effect is very small, at the limit of the fit sensitivity, both for the mass and the width.

The second, more relevant, source of uncertainty connected to the LPA is in its possible definitions, i.e. the ambiguity present in the way of expanding the amplitude around the double resonant W pole. The standard `YFSWW` uses the so called LPA$_A$ definition; a comparison with the LPA$_B$ one can give an estimate of the effect from the intrinsic ambiguity in the LPA definition. A dedicated study has been performed evaluating the difference:

$$\Delta\mathcal{O}(\alpha)(\mathrm{LPA}_A - \mathrm{LPA}_B) = \Delta(\mathrm{Best\ LPA}_A - \mathrm{no\ NL\ LPA}_A) - \Delta(\mathrm{Best\ LPA}_B - \mathrm{no\ NL\ LPA}_B)$$

in order to evaluate only the effect of the different scheme on the radiative corrections (and not at Born level). The size of the effect is less than 1 MeV/c^2 for the mass and less than 4 MeV/c^2 for the width.

Radiative Corrections on 4-f Background Diagrams: Single W

The Double Pole Approximation (DPA) is known to be valid within a few W widths of the double resonant pole. The DPA correction is applied only to the `CC03` part of the matrix element (and partly to the interference, see [13]); non-`CC03` diagrams contributions are not directly affected by the DPA uncertainty (except for possible effects in the interference term which is relevant for the electron channel).

It is clear that this procedure still leaves the problem of the approximated radiative corrections treatment for the non-`CC03` part of the matrix element (and the interference). The ISR studies previously discussed can reasonably cover the most relevant part of the electroweak radiative corrections uncertainties present also for the $\mathrm{W}^+\mathrm{W}^-$-like 4-f background diagrams, e.g. the non-`CC03` part. There is, however, a notable exception: the so called single W diagrams for the $q\bar{q}'e\nu$ final state.

The bulk of single W events are rejected in the W mass and width analysis, since the electron in these events is lost in the beam pipe. But the `CC03` - single W interference is sizeable, and it has a strong impact on the W mass result in the electron channel. The situation is different in the W width analysis, where in $e\overline{\nu}_e q\bar{q}'$ events reconstructed by the electron analysis the effects of non-`CC03` diagrams and the `CC03` - non-`CC03` interference are opposite in sign and almost completely cancel.

The situation is made even more complex by the cross-talk between channels, e.g. events belonging in reality to one channel but reconstructed as belonging to another one. This cross-talk is particularly relevant between semi-leptonic electron and tau decays, and this explains why the τ channel analysis is also sensitive to this uncertainty source.

The effect of this uncertainty has been studied in two ways. Firstly, since the uncertainty on the single W rate associated to radiative corrections is known in literature to be about 4%, the non-`CC03` part of the matrix element, assumed to be dominated by the single W contribution, has been varied by 4% for $q\bar{q}'e\nu$ final states. Another possible source of uncertainty related to 4-f background is estimated by partly applying the DPA correction to the interference term (see the discussion in [13]). The effect of this way of computing the corrections can be considered as another estimate of the uncertainty related to the 4-f background presence.

The maximal size of these effects is about 6 MeV/c^2 (for the mass in $qqe\nu$ and the width in $qq\tau\nu$).

Total Uncertainty

The results of all the studies presented are combined in a single uncertainty for each channel. Tables 11 and 12 present the estimates for the mass and width from the different sources of uncertainties discussed above.

M_W Electroweak Correction Systematic Errors (MeV/c^2)				
Uncertainty Source	$e\overline{\nu}_e q\bar{q}'$	$\mu\overline{\nu}_\mu q\bar{q}'$	$\tau\overline{\nu}_\tau q\bar{q}'$	$q\bar{q}'\bar{q}q'$
ISR	1.0	1.0	1.0	1.0
FSR	0.5	0.5	1.0	-
NF $\mathcal{O}(\alpha)$	1.0	1.0	1.0	2.0
NL $\mathcal{O}(\alpha)$	1.0	1.0	1.0	1.0
4-f Background	5.5	0.5	1.0	0.5
Total	9	4	5	4.5

Table 11: Summary of the systematic uncertainties on the W mass due to electroweak corrections. The total is computed adding linearly the absolute values of all the contributions.

Γ_W Electroweak Correction Systematic Errors (MeV/c^2)				
Uncertainty Source	$e\overline{\nu}_e q\bar{q}'$	$\mu\overline{\nu}_\mu q\bar{q}'$	$\tau\overline{\nu}_\tau q\bar{q}'$	$q\bar{q}'\bar{q}q'$
ISR	2.0	2.0	2.0	2.0
FSR	1.0	1.0	2.0	-
NF $\mathcal{O}(\alpha)$	2.0	2.0	2.0	2.0
NL $\mathcal{O}(\alpha)$	4.0	4.0	4.0	4.0
4-f Background	2.0	1.0	6.0	1.0
Total	11	10	16	9

Table 12: Summary of the systematic uncertainties on the W width due to electroweak corrections. The total is computed adding linearly the values of all the contributions.

	$\sqrt{s}$ Nominal [GeV]									
	161	172	183	189	192	196	200	202	205	207
E_{cm} Error [MeV]	25.4	27.4	20.3	21.6	21.6	23.2	23.7	23.7	36.9	41.7

Table 13: Uncertainties on the LEP energies for the different centre-of-mass energy points.

The total uncertainty per channel is conservatively computed summing linearly the values of the contributions. All the numbers have been rounded to 0.5 MeV/c^2.

Reference [13] also reports a comparison of `YFSWW` with the other completely independent Monte Carlo generator `RacoonWW` [37] which implements radiative corrections in the DPA. This study has not been directly used in the error estimation presented here due to the limitations in the treatment of non-collinear radiation in `RacoonWW`. However, this study does provide additional confidence in the validity of the `YFSWW` calculation.

As can be seen, the uncertainty on the W mass associated with the electroweak radiative corrections is found to be less than 10 MeV/c^2.

6.8 LEP Collision Energy

The average LEP collision energy is evaluated at 15 minute intervals of running or after significant changes in the beam energy. The measured centre-of-mass energy is imposed as a constraint in the kinematic fit, and hence the relative error on the collision energy translates to approximately the same fractional error on the W mass determination. The effect of the uncertainty on the W width determination is negligible.

The beam energy is estimated using the LEP energy model, discussed in section 2 based on 16 NMR probes in dipole magnets around the LEP ring calibrated with the RDP technique. The compatibility of three cross-check methods with this determination was used to determine a set of small energy offsets. The relative size of this offset was energy dependent, rising to a maximum of 1.6×10^{-5} at 207 GeV centre-of-mass energy.

The LEP energy working group also assessed the uncertainties in the collision energies and supplied these in the form of a 10×10 correlation matrix. The uncertainties increase as the collision energy increases, due to the fact that higher energies are further from the RDP normalisation region. The errors are given in table 13. At 183 GeV centre-of-mass energy the uncertainty on the collision energy is 20.3 MeV. This rises to 23.7 MeV at 202 GeV. For the energy points at values of 205 and 207 GeV, taken in the year 2000, there is an additional uncertainty due to the 'Bending Field Spreading' strategy, in which the corrector magnets were powered in a coherent manner to increase the overall dipole field and thus the LEP energy [7] . This leads to a larger error for the year 2000. For the energy points at 161 and 172 GeV, taken in the year 1996, there is also a small increase in the error, compared to 183 GeV, due to increased uncertainties in the NMR calibration for this year.

The mean energy difference between the electron and positron beams is less than 4 MeV at all energies and hence the effect on the W mass or width determination is negligible. The momentum spread of the electrons or positrons in a bunch gives rise to a variation in the centre-of-mass energy of the collisions and boost of the centre of mass frame with respect to the laboratory frame. The spreads in centre-of-mass collision energies have been evaluated by the LEP energy working group [7] and range from 144 to 265 MeV. The corresponding effects for the W mass and width analyses are negligible.

6.9 Aspect Ratio

The aspect ratio is defined as the ratio of the length to the width of the detector. As all the sub-detectors of DELPHI are aligned with respect to the Vertex Detector, the knowledge of the aspect ratio is limited by the precision to which the position and dimensions of the Vertex Detector can be measured. The effect of a mismeasurement of the aspect ratio is to introduce a bias on the measurement of the polar angle, θ. As the W boson production polar angle is not isotropic but forward peaked, a mismeasurement of the aspect ratio would result in a small bias on the average opening angle of the W decay products, and hence induce a small bias on the reconstructed W mass.

The correspondence of hits in the overlapping silicon modules is sensitive to a misalignment of the Vertex Detector. In fact the study of these overlaps constitutes an essential part of the procedure for the alignment of the Vertex Detector. From this study, discussed further in [9], it is concluded that a reasonable estimate of the aspect ratio uncertainty is 3×10^{-4}. Such a bias would result in a shift in W mass below 1 MeV/c^2 for the semi-leptonic channel, and of 2 MeV/c^2 for the fully-hadronic one. The effect on the W width is negligible.

6.10 Background Description

The background events for the W-pair selection are from four-fermion or hadronic two fermion processes.

The four-fermion background uncertainty is studied and described in the electroweak corrections uncertainties (section 6.7) and in the jet description studies (section 6.5) parts of this paper.

The dominant source of background to W pair production, both in the semi-leptonic and in the fully-hadronic channel, is from Z $\rightarrow q\bar{q}(\gamma)$ events.

In the semi-leptonic channel the 2-fermion background is relatively small with the main uncertainty in its rate arising from the discrepancy between data and simulation in the rate of misidentification of energetic photons (from radiative return to the Z peak events) as electrons. This misidentification is mainly due to the electron-positron conversion of photons and the spurious associations of forward vertex detectors hits to an electromagnetic cluster in the calorimeter. A data-simulation comparison shows that a 10% fluctuation of the background is possible without significantly degrading the agreement between the data and simulation. The theory uncertainty on the 2-fermion cross-section is generally small, in the worst case at the 2% level [38].

In the fully-hadronic channel the 2-fermion background is more important, and the major contribution to the uncertainty is from the four-jet final state production mechanism. The study performed in [39] has shown that the maximal difference in the estimated 2-fermion background rate is 10% coming from changing from `PYTHIA` to `HERWIG` as the hadronisation model, with the `ARIADNE` model giving intermediate results. The effect on the W mass is 13 MeV/c^2 at $\sqrt{s} = 189$ GeV, and 4 MeV/c^2 at $\sqrt{s} = 206.5$ GeV, while the effect on the W width is 40 MeV/c^2 over the whole range of centre-of-mass energies.

In summary, applying a variation of $\pm 10\%$ on the Z $\rightarrow q\bar{q}(\gamma)$ event rate is used to provide an estimate of the systematic uncertainty on the background level for both the semi-leptonic and fully-hadronic channel mass and width measurements. This variation also covers any discrepancies seen in the data and simulation comparison plots shown in this paper.

The importance of the background event mass distribution has also been investigated. In the semi-leptonic analyses the mass distribution taken from the simulation has been replaced with a constant level and half of the variation in the result has been taken as a systematic. In the fully-hadronic channel this systematic was assessed by changing the generator used for the background between `PYTHIA`, `HERWIG` and `ARIADNE`.

The background level and background shape uncertainties were added in quadrature and the resulting errors are reported in tables 14, 15 and 16 below.

6.11 Bose-Einstein Correlations

Correlations between final state hadronic particles are dominated by Bose-Einstein Correlations (BEC), a quantum mechanical effect which enhances the production of identical bosons close in phase space. The net effect is that multiplets of identical bosons are produced with smaller energy-momentum differences than non-identical ones.

BEC for particles produced from the same W boson affect the normal fragmentation and are therefore treated implicitly in the fragmentation uncertainties which are constrained by the large amount of Z-data. BEC for pairs of particles coming from different Ws cannot be constrained or safely predicted by the information from single hadronically decaying vector bosons.

A dedicated and model-independent measurement of the BEC effect was performed by the DELPHI collaboration in [40] while other LEP experiments have made similar measurements [41]. Comparing these results with Monte Carlo models constitutes the only way to estimate potential systematic uncertainties from BEC. The `LUBOEI` model BE_{32} [42] was found to give the largest shift in the measured value of $\mathrm{M_W}$ for a given amount of BEC. Other models give smaller shifts and some models predict no appreciable BEC shifts at all. It was decided not to apply any corrections due to BEC and evaluate the systematic error as the largest predicted shift consistent with the DELPHI data. The predicted shift plus one standard deviation of its error is used as the estimator of the systematic error.

The DELPHI result for BEC is a 2.4 standard deviation evidence for BEC between different Ws and a correlation strength, Λ, which can be compared to the BE_{32} prediction at the same effective correlation length scale:

$$\Lambda_{\mathrm{data}}\Big/\Lambda_{\mathrm{BE}_{32}} = 0.55 \pm 0.20(\mathrm{Stat.}) \pm 0.11(\mathrm{Syst.}). \tag{9}$$

The predicted mass shift, BEC inside Ws only − BEC inside and between Ws, using BE_{32} (with model parameters PARJ(92) = 1.35 and PARJ(93) = 0.34) is 40 ± 10 MeV/c^2 for the standard mass analysis, 33 ± 11 MeV/c^2 for the cone jet mass reconstruction analysis and -17 ± 20 MeV/c^2 for the W width analysis. The observed mass shift in BE_{32} is linear in the observed correlation, $\Lambda_{\mathrm{BE}_{32}}$. Applying the one standard deviation upper bound of the correlation parameter this translates into a systematic error of 31 MeV/c^2 from BEC for the standard analysis and 26 MeV/c^2 for the cone analysis. A systematic error of 20 MeV/c^2 is applied for the W width. The mass and width shifts were evaluated with the simulation model over the full range of centre-of-mass energies and no energy dependence was observed. The shifts reported are the average values. Conservatively, these errors are applied as symmetric uncertainties.

The combined DELPHI BEC measurements of the correlation strength and effective correlation length scale suggest that the between-W BEC occur with an effective correlation length scale which is larger that the one predicted by BE_{32}. If this is the case, the number of pairs effectively affected by the BEC is reduced and also the effect per pair is diminished. Furthermore, the other LEP experiments have reported smaller values of

$\Lambda_{\text{data}}/\Lambda_{\text{BE}_{32}}$ than that observed by DELPHI. Hence the systematic uncertainties applied in this analysis are considered conservative.

6.12 Colour Reconnection

In the reaction $e^+e^- \to \mathrm{W}^+\mathrm{W}^- \to (q_1\bar{q}_2)(q_3\bar{q}_4)$ the hadronisation models used for this analysis treat the colour singlets $q_1\bar{q}_2$ and $q_3\bar{q}_4$ coming from each W boson independently. However, interconnection effects between the products of the two W bosons may be expected since the lifetime of the W bosons ($\tau_\mathrm{W} \simeq \hbar/\Gamma_\mathrm{W} \simeq 0.1$ fm/c) is an order of magnitude smaller than the typical hadronisation times.

The exchange of coloured gluons between partons from hadronic systems from different W bosons can induce the so-called colour reconnection (CR) effect in the development of the parton shower. This effect can in principle distort the properties of the final hadronic system and therefore affect the W mass measurement, if not properly accounted for in the simulation.

At perturbative level the effects are expected to be small [43], and the impact on the reconstructed W mass has been evaluated to be at most 5 MeV/c^2. However, CR effects can be large at hadronisation level, due to the large numbers of soft gluons sharing the space-time region. These effects have been studied by introducing CR effects into hadronisation models and comparing with DELPHI data and are reported in [30].

The most studied model, and the one used for the evaluation of the systematic uncertainty on the W mass and width measurement, is the Sjöstrand-Khoze "Type 1" model (`SK-I`) [44]. This model of CR is based on the Lund string fragmentation phenomenology: the strings are considered as colour flux tubes with some volume, and reconnection occurs when these tubes overlap. The probability of reconnection in an event,P_{reco}, is parameterised by the value κ, according to the volume of overlap between the two strings $V_{overlap}$:

$$P_{reco} = 1 - e^{-\kappa V_{overlap}}. \tag{10}$$

The parameter κ determines the reconnection probability. By comparing the data with the model predictions evaluated at several κ values it is possible to determine the value most consistent with the data and extract the corresponding reconnection probability.

Another model has been developed by the same authors (`SK-II`') and also implemented in `PYTHIA` but is found to predict a smaller shift on the reconstructed W mass than `SK-I` for the same reconnection probability.

Further CR models are available in the `HERWIG` and `ARIADNE` Monte Carlo programs. In `ARIADNE`, which implements an adapted version of the Gustafson-Häkkinen model [45], the model used [46] allows for reconnections between partons originating in the same W boson, or from different W bosons if they have an energy smaller than the width of the W boson. The mass shift from CR is evaluated from the difference between the shift when the reconnections are made only in the same W boson and when the full reconnections are made. In the standard DELPHI analysis, the shift was found to be 11 ± 11 MeV/c^2.

In `HERWIG` the partons are reconnected, with a reconnection probability of 1/9, if the reconnection results in a smaller total cluster mass. The shift in the reconstructed W mass at 189 GeV centre-of-mass energy was found to be 29 ± 7 MeV/c^2, the same shift as obtained from a κ value of 0.29 in the `SK-I` model.

DELPHI has performed two analyses to compare these simulation models with data which are described in detail in [30].

The first one is based on the measurement of the particle flow between the jets in a four jets $\mathrm{W}^+\mathrm{W}^-$ event. On a subsample of strictly four-jet events two regions can be defined, the region between jets from the same W (called inside-W regions) and the region between jets from different W bosons (called between-W regions). The ratio R of the particle fluxes in the inside-W and between-W regions (limiting the analysis to the central part of these regions) is an observable sensitive to CR effects. The comparison of the flux measured in real data with the prediction of the SK-I model as a function of κ allows the value to be determined which is most consistent with data, and its uncertainty.

The second method used exploits the observation that in the direct reconstruction analysis of the W mass, different W mass estimators have different sensitivities to CR effects. As discussed in section 5.3.2 removing particles from the inter-jet regions reduces the sensitivity to CR effects and hence can be used to measure the CR effect. The correlation between the measurement of the mass shift (using the standard or cone jet reconstruction techniques) and the measurement of the mass from these techniques is only 11%.

From the combination of these two analyses and in the framework of the SK-I model, the value of the κ parameter most compatible with the data is found to be [30]:

$$\kappa = 2.2 \pm^{2.5}_{1.3} .$$

The CR shift in the reconstructed W mass as a function of the SK-I κ parameter is provided as figure 13, the results of the standard and cone jet reconstruction techniques are indicated. Figure 14 shows the CR shift for the W width reconstruction analysis.

The systematic uncertainty on the W mass and width is calculated using the one standard deviation upper bound of κ of 4.7. As reported above, this systematic error is considerably larger than that which would be evaluated from the ARIADNE or HERWIG CR models. Furthermore, this value of κ is larger than that reported by the other LEP experiments [31]. The CR W mass shift is dependent on the centre-of-mass energy in the SK-I model as shown in figures 13 and 14. However, we prefer not to rely on the centre-of-mass energy evolution of the SK-I CR shift (leading to a change in relative weights when averaging the results from different centre-of-mass energies) and instead choose to quote the systematic errors at 200 GeV (close to the average centre-of-mass energy of the data). In light of the significant range of CR effect estimates no correction is made to the W mass or width results and for simplicity a symmetric systematic uncertainty is applied. The corresponding systematics uncertainties on the W mass are 212 MeV/c^2 (standard), 116 MeV/c^2 (cone jet reconstruction) and 247 MeV/c^2 for the W width analysis.

7 Results

The results of the analyses and the final combinations of these results are presented in this section. The results are obtained at a range of nominal centre-of-mass energies and in the four event selection channels. Combined results are obtained from an average of these results and also an average with the previously published DELPHI data [1,2] that have not been reanalysed in this paper.

Subdividing the results by data-taking years and nominal centre-of-mass energies enables a proper treatment of the correlated systematic uncertainty from the LEP collision energy and other dependences on the centre-of-mass energy or data-taking period. A detailed breakdown of the sources of systematic uncertainty, as shown in tables 14,15 and 16, is provided for each result and the correlations specified.

The combination is performed and the evaluation of the components of the total error assessed using the Best Linear Unbiased Estimate (BLUE) technique [47].

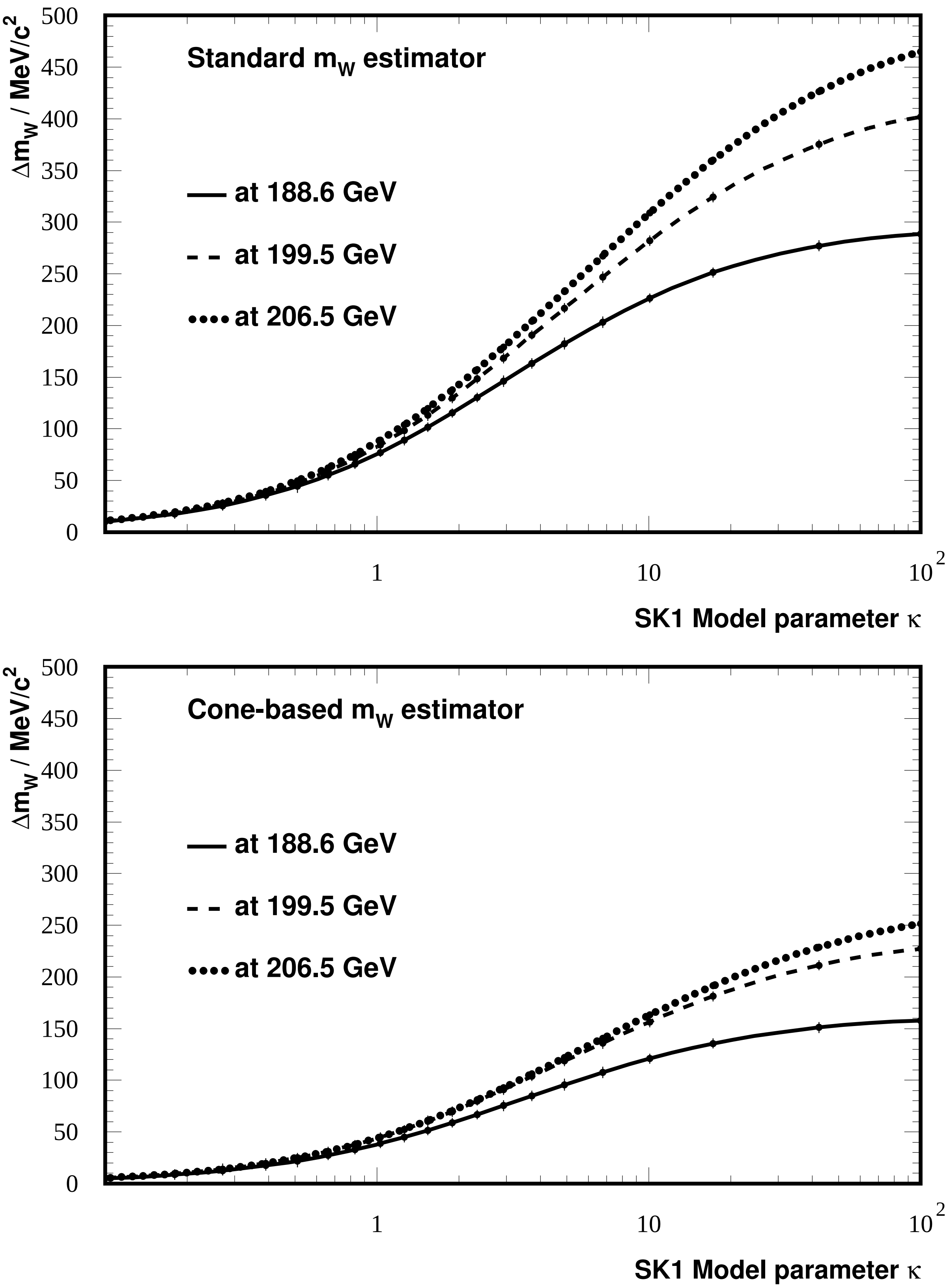

Figure 13: W mass shift caused by the colour reconnection effect as described in the SK-I model plotted as a function of the model parameter κ which controls the fraction of reconnected events. The upper plot is for the standard W mass analysis and the lower plot when the cone jet reconstruction technique is applied.

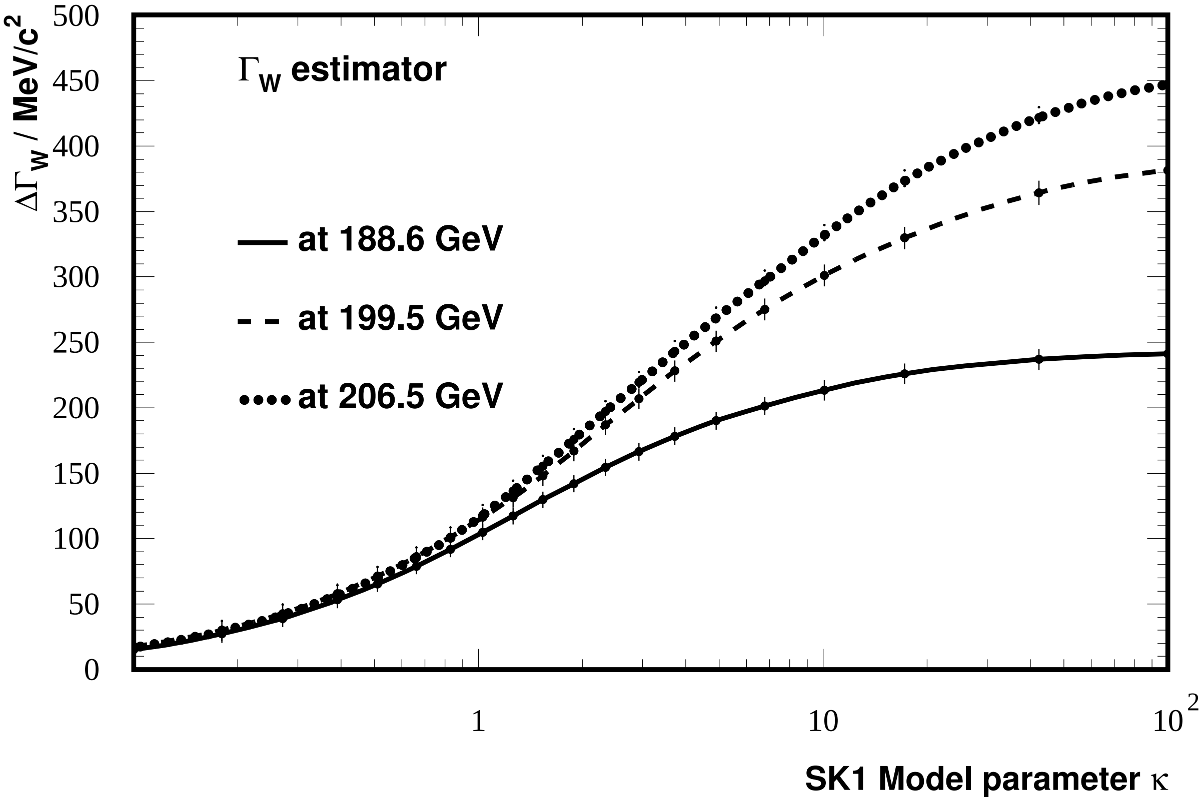

Figure 14: W width shift caused by the colour reconnection effect as described in the SK-I model plotted as a function of the model parameter κ which controls the fraction of reconnected events.

M_W Systematic Errors (MeV/c^2) at 189 GeV				
Sources of Systematic Error	$e\bar{\nu}_e q\bar{q}'$	$\mu\bar{\nu}_\mu q\bar{q}'$	$\tau\bar{\nu}_\tau q\bar{q}'$	$q\bar{q}'\bar{q}q'$
Statistical Error on Calibration	12	10	15	4
Lepton Corrections	24	16	-	-
Jet Corrections	18	15	19	24
Fragmentation	10	10	13	12
Electroweak Corrections	9	4	5	5
Background	5	1	12	17
LEP Energy	9	9	9	9
Bose-Einstein Correlations	-	-	-	31/26
Colour Reconnection	-	-	-	212/116

Table 14: Contributions to the systematic error on the W mass measurement for data taken at a nominal centre-of-mass energy of 189 GeV. Where two uncertainties are reported in the $q\bar{q}'\bar{q}q'$ analysis column the first corresponds to the standard analysis and the second to the cone jet reconstruction analysis.

7.1 W Mass

The W mass is extracted separately in the analyses designed to select the $e\bar{\nu}_e q\bar{q}'$, $\mu\bar{\nu}_\mu q\bar{q}'$ and $\tau\bar{\nu}_\tau q\bar{q}'$ decay channels. The values obtained are given in table 17 for the analysed centre-of-mass collision energies. The semi-leptonic channel analysis results are combined into a single $\ell\bar{\nu}_\ell q\bar{q}'$ value for each year of data taking. When performing these combinations the following sources of systematic uncertainty are taken as fully-correlated between lepton channels and between years: electroweak corrections, fragmentation, jet corrections, lepton corrections, background. The LEP energy measurement correlations are taken from the matrix supplied in [7]. The simulation calibration statistics are taken as uncorrelated.

The W mass is also obtained from the $q\bar{q}'\bar{q}q'$ channel using both the standard and cone jet reconstruction technique. The results obtained from these analyses are given in table 18.

In addition to the analyses presented in this paper, measurements of the W mass have also been made using the data collected in 1996.

7.1.1 W Mass from the W^+W^- Cross-section

The DELPHI collaboration has measured the total `CC03` W^+W^- cross-section, as a function of centre-of-mass energy, using the full data sample collected by the collaboration during LEP2 operations [39]. Assuming the validity of the cross-section dependence predicted by the Standard Model these measurements can be translated into a measurement of the W mass. Only the cross-section measurements close to the W^+W^- threshold have significant sensitivity to the W mass.

The Standard Model cross-section dependence on the W mass is obtained from the `WPHACT` and `YFSWW` generator setup, as discussed in section 4.2, and cross-checked with the improved Born approximation calculation. The theoretical error on the total W^+W^- cross-section near threshold was estimated as 2% decreasing with increasing collision energy to 0.5% in the DPA-valid region [48], the corresponding error on the W mass is marked below as Theor. The sources of experimental systematic error have not been

M_W Systematic Errors (MeV/c^2) at 205 GeV				
Sources of Systematic Error	$e\overline{\nu}_e q\overline{q}'$	$\mu\overline{\nu}_\mu q\overline{q}'$	$\tau\overline{\nu}_\tau q\overline{q}'$	$q\overline{q}'\overline{q}q'$
Statistical Error on Calibration	15	10	17	4
Lepton Corrections	25	21	-	-
Jet Corrections	26	21	33	28
Fragmentation	10	10	13	12
Electroweak Corrections	9	4	5	5
Background	4	6	19	5
LEP Energy	15	15	15	15
Bose-Einstein Correlations	-	-	-	31/26
Colour Reconnection	-	-	-	212/116

Table 15: Contributions to the systematic error on the W mass measurement for data taken at a nominal centre-of-mass energy of 205 GeV. Where two uncertainties are reported in the $q\overline{q}'\overline{q}q'$ analysis column the first corresponds to the standard analysis and the second to the cone jet reconstruction analysis.

Γ_W Systematic Errors (MeV/c^2) at 205 GeV		
Sources of Systematic Error	$\ell\overline{\nu}_\ell q\overline{q}'$	$q\overline{q}'\overline{q}q'$
Statistical Error on Calibration	15	9
Lepton Corrections	48	-
Jet Corrections	38	169
Fragmentation	29	8
Electroweak Corrections	11	9
Background	43	51
Bose-Einstein Correlations	-	20
Colour Reconnection	-	247

Table 16: Contributions to the systematic error on the W width measurement for data taken at a nominal centre-of-mass energy of 205 GeV.

reevaluated and are as reported in [1], apart from use of the revised collision energy uncertainty.

From a χ^2 fit of the measured cross-sections at centre-of-mass energies of 161.31, 172.14 and 182.65 GeV the mass has been determined to be

$$M_W = 80.448 \pm 0.434(\text{Stat.}) \pm 0.090(\text{Syst.}) \pm 0.043(\text{Theor.}) \pm 0.013(\text{LEP})\ \text{GeV}/c^2.$$

7.1.2 W Mass from Direct Reconstruction at $\sqrt{s} = 172$ GeV

For completeness, we also report here on the relatively small data sample (10 pb^{-1}) recorded in 1996 at $\sqrt{s} = 172$ GeV. This sample was analysed and W mass results published using the $e\overline{\nu}_e q\overline{q}'$, $\mu\overline{\nu}_\mu q\overline{q}'$ and $q\overline{q}'\overline{q}q'$ decay channels in [2]. The $q\overline{q}'\overline{q}q'$ analysis was performed using a standard analysis rather than a cone jet reconstruction based analysis.

This data sample has not been reprocessed, nor have W width results been produced with this sample. The estimates of systematic uncertainties are retained from the original paper except for the uncertainties arising from colour reconnection and Bose-Einstein

Correlations in the $q\bar{q}'\bar{q}q'$ channel, where the errors reported above for the standard analysis are used, and the use of the final LEP collision energy uncertainty. The revised values are

$$M_W = 80.51 \pm 0.57(\text{Stat.}) \pm 0.05(\text{Syst.}) \pm 0.01(\text{LEP})\ \text{GeV}/c^2,$$

for the combined semi-leptonic channels, and

$$M_W = 79.90 \pm 0.59(\text{Stat.}) \pm 0.05(\text{Syst.}) \pm 0.21(\text{FSI.}) \pm 0.01(\text{LEP})\ \text{GeV}/c^2,$$

for the fully-hadronic decay channel. These values have been included in tables 17 and 18.

7.1.3 Combined Results

The combinations of the results are performed, assuming that the following components of the error are fully-correlated between years (and energy points) and between the fully-hadronic and semi-leptonic channels: electroweak corrections, fragmentation and jet correction. The lepton-related detector systematic in the semi-leptonic channel is also assumed to be fully correlated between years. The colour reconnection and Bose-Einstein effect in the fully-hadronic channel is assumed to be fully correlated between years. The error arising from calibration statistics is uncorrelated between years in the semi-leptonic analysis, as it was determined from independent Monte Carlo simulation samples, but this error is correlated in the fully-hadronic channel as the values were obtained from an overall fit to the samples at all centre-of-mass energies. This error source is uncorrelated in the combination of the semi-leptonic and fully-hadronic channel. The background-related systematic is assumed to be fully correlated between years in both the fully-hadronic and semi-leptonic analyses but uncorrelated between the two channels. The LEP centre-of-mass energy uncertainty is, of course, fully correlated between the semi-leptonic and fully-hadronic decay channels but is only partially correlated between years. The inter-year correlations were assessed by the LEP energy working group [7] and this correlation matrix was applied when performing the combinations reported here.

The results from the semi-leptonic W mass analyses in each year of data taking (1996-2000) have been combined. The result for the analysis aimed at selecting events in the $e\bar{\nu}_e q\bar{q}'$ decay channel is:

$$M_W = 80.388 \pm 0.133(\text{Stat.}) \pm 0.036(\text{Syst.}) \pm 0.010(\text{LEP})\ \text{GeV}/c^2,$$

the combination has a χ^2 probability of 25%.

The result for the analysis aimed at selecting events in the $\mu\bar{\nu}_\mu q\bar{q}'$ decay channel is:

$$M_W = 80.294 \pm 0.098(\text{Stat.}) \pm 0.028(\text{Syst.}) \pm 0.010(\text{LEP})\ \text{GeV}/c^2,$$

the combination has a χ^2 probability of 96%.

The $\tau\bar{\nu}_\tau q\bar{q}'$ selection includes significant cross-talk from events in other decay channels (see table 2) and a result from the 1996 data is not available. The result for the analysis aimed at selecting events in the $\tau\bar{\nu}_\tau q\bar{q}'$ decay channel (in the years 1997-2000) is:

$$M_W = 80.387 \pm 0.144(\text{Stat.}) \pm 0.033(\text{Syst.}) \pm 0.010(\text{LEP})\ \text{GeV}/c^2,$$

the combination has a χ^2 probability of 56%.

The result for the combined semi-leptonic W mass analyses is:

$$M_W = 80.339 \pm 0.069(\text{Stat.}) \pm 0.029(\text{Syst.}) \pm 0.009(\text{LEP})\ \text{GeV}/c^2,$$

the combination has a χ^2 probability of 16%.

Similarly, the results on the W mass extracted from the fully-hadronic event analysis have also been combined. The value from 1996 uses the standard reconstruction technique; the results of the cone-jet reconstruction technique are used for the other data taking years (1997-2000). The combined result is:

$$\mathrm{M_W} \;=\; 80.311 \pm 0.059(\mathrm{Stat.}) \pm 0.032(\mathrm{Syst.}) \pm 0.119(\mathrm{FSI}) \pm 0.010(\mathrm{LEP})\ \mathrm{GeV}/c^2,$$

the combination also has a χ^2 probability of 16%.

The mass difference between the W boson mass measurements obtained from the fully-hadronic and semi-leptonic channels $\Delta\mathrm{M_W}(\mathrm{q\bar{q}'\bar{q}q'} - \ell\overline{\nu}_\ell\mathrm{q\bar{q}'})$, has been determined. A significant non-zero value for $\Delta\mathrm{M_W}$ could indicate that Bose-Einstein or colour reconnection effects are biasing the value of $\mathrm{M_W}$ determined from $\mathrm{q\bar{q}'\bar{q}q'}$ events. Since $\Delta\mathrm{M_W}$ is primarily of interest as a cross-check of the possible effects of final state interactions, the errors from CR and BEC are set to zero in its determination and the results of the standard reconstruction technique, rather than the FSI effect-reducing cone-jet reconstruction technique, are used for the $\mathrm{q\bar{q}'\bar{q}q'}$ analysis. The result provides no evidence for FSI effects:

$$\Delta\mathrm{M_W}(\mathrm{q\bar{q}'\bar{q}q'} - \ell\overline{\nu}_\ell\mathrm{q\bar{q}'}) \;= 0.024 \pm 0.090\ \mathrm{GeV}/c^2,$$

the combination has a χ^2 probability of 20%.

The final DELPHI result for the W mass for the full LEP2 data sample is obtained by combining the values obtained from the direct reconstruction method in the $\ell\overline{\nu}_\ell\mathrm{q\bar{q}'}$ analysis and cone jet reconstruction technique $\mathrm{q\bar{q}'\bar{q}q'}$ analysis in each data taking year. The value obtained from the threshold cross-section is also included in this average. The combined result is:

$$\mathrm{M_W} \;=\; 80.336 \pm 0.055(\mathrm{Stat.}) \pm 0.028(\mathrm{Syst.})\ \pm 0.025(\mathrm{FSI}) \pm 0.009(\mathrm{LEP})\ \mathrm{GeV}/c^2,$$

the combination has a χ^2 probability of 15%.

Although the statistical error in the $\ell\overline{\nu}_\ell\mathrm{q\bar{q}'}$ and $\mathrm{q\bar{q}'\bar{q}q'}$ channels is similar, owing to the large systematic error attributed to final state cross-talk effects the weight of the fully-hadronic channel results in this average is 21%. The weight of the threshold cross-section measurement of the W mass is only 2% due to the small data sample collected at 161 GeV centre-of-mass energy. The full error breakdown of the averages is provided in table 19.

The DELPHI measurement of the colour reconnection effect is reported in [30]. This measurement places relatively loose constraints on the size of the W mass uncertainty from CR effects, and thus leads to the small impact of the fully-hadronic mass in the DELPHI average. For comparison the value of the combined DELPHI W mass as a function of the CR uncertainty is shown in table 20. All other errors, including that arising from Bose-Einstein correlations, have been kept constant in these results.

7.2 W **Width**

The W width has been measured from the semi-leptonic and the fully-hadronic decay channel events. As the analysis is less sensitive to the W width than the W mass, the width is extracted by performing a combined fit of the three semi-leptonic channels rather than from each channel individually. The results are given in table 21. The correlations assumed for the combinations are identical to those reported above for the W mass.

The results from the semi-leptonic W width analyses in each year of data taking (1997-2000) have been combined, the result obtained is:

$$\Gamma_W = 2.452 \pm 0.184(\text{Stat.}) \pm 0.073(\text{Syst.})\ \text{GeV}/c^2,$$

the combination has a χ^2 probability of 9%.

Similarly, the results on the W width extracted from the fully-hadronic event analysis have also been combined, the result obtained is:

$$\Gamma_W = 2.237 \pm 0.137(\text{Stat.}) \pm 0.139(\text{Syst.})\ \pm 0.248(\text{FSI})\ \text{GeV}/c^2,$$

the combination has a χ^2 probability of 62%.

The final DELPHI result for the W width for the full LEP2 data sample is obtained by combining the values obtained from the direct reconstruction method in the $\ell\overline{\nu}_\ell q\bar{q}'$ analysis and $q\bar{q}'\bar{q}q'$ analysis in each data taking year. The combined result is:

$$\Gamma_W = 2.404 \pm 0.140(\text{Stat.}) \pm 0.077(\text{Syst.})\ \pm 0.065(\text{FSI})\ \text{GeV}/c^2,$$

the combination has a χ^2 probability of 27%.

Although the statistical error in the $\ell\overline{\nu}_\ell q\bar{q}'$ and $q\bar{q}'\bar{q}q'$ channels is similar, owing to the large systematic error attributed to final state cross-talk effects the weight of the fully-hadronic channel results in this average is 26%. The full error breakdown of the averages is provided in table 22.

8 Conclusions

The mass and width of the W boson have been measured using the reconstructed masses in $e^+e^- \to W^+W^-$ events decaying to $q\bar{q}'\bar{q}q'$ and $\ell\overline{\nu}_\ell q\bar{q}'$ states. The W Mass was also extracted from the dependence of the W^+W^- cross-section close to the production threshold. The full LEP2 data sample of 660 pb^{-1} collected by the DELPHI experiment at centre-of-mass energies from 161 to 209 GeV has been used. The final results are:

$$M_W = 80.336 \pm 0.055(\text{Stat.}) \pm 0.028(\text{Syst.})\ \pm 0.025(\text{FSI}) \pm 0.009(\text{LEP})\ \text{GeV}/c^2,$$

$$\Gamma_W = 2.404 \pm 0.140(\text{Stat.}) \pm 0.077(\text{Syst.})\ \pm 0.065(\text{FSI})\ \text{GeV}/c^2.$$

These results supersede the previously published DELPHI results [1–4].

Acknowledgements

We are greatly indebted to our technical collaborators, to the members of the CERN-SL Division for the excellent performance of the Lep collider, and to the funding agencies for their support in building and operating the Delphi detector. We also wish to offer our thanks to the Lep energy working group for their measurement of the Lep collision energy which plays an important role in the analysis presented in this paper.
We acknowledge in particular the support of
Austrian Federal Ministry of Education, Science and Culture, GZ 616.364/2-III/2a/98,
FNRS–FWO, Flanders Institute to encourage scientific and technological research in the industry (IWT) and Belgian Federal Office for Scientific, Technical and Cultural affairs (OSTC), Belgium,
FINEP, CNPq, CAPES, FUJB and FAPERJ, Brazil,
Ministry of Education of the Czech Republic, project LC527,
Academy of Sciences of the Czech Republic, project AV0Z10100502,
Commission of the European Communities (DG XII),
Direction des Sciences de la Matière, CEA, France,
Bundesministerium für Bildung, Wissenschaft, Forschung und Technologie, Germany,
General Secretariat for Research and Technology, Greece,
National Science Foundation (NWO) and Foundation for Research on Matter (FOM), The Netherlands,
Norwegian Research Council,
State Committee for Scientific Research, Poland, SPUB-M/CERN/PO3/DZ296/2000, SPUB-M/CERN/PO3/DZ297/2000, 2P03B 104 19 and 2P03B 69 23(2002-2004),
FCT - Fundação para a Ciência e Tecnologia, Portugal,
Vedecka grantova agentura MS SR, Slovakia, Nr. 95/5195/134,
Ministry of Science and Technology of the Republic of Slovenia,
CICYT, Spain, AEN99-0950 and AEN99-0761,
The Swedish Research Council,
Particle Physics and Astronomy Research Council, UK,
Department of Energy, USA, DE-FG02-01ER41155,
EEC RTN contract HPRN-CT-00292-2002.

References

[1] DELPHI Collaboration, P. Abreu *et al.*, Phys. Lett. **B397**(1997) 158

[2] DELPHI Collaboration, P. Abreu *et al.*, Eur. Phys. J. **C2**(1998) 581

[3] DELPHI Collaboration, P. Abreu *et al.*, Phys. Lett. **B462**(1999) 410

[4] DELPHI Collaboration, P. Abreu *et al.*, Phys. Lett. **B511**(2001) 159

[5] ALEPH Collaboration, S. Schael *et al.*, Eur. Phys. J. **C47**(2006) 309;
L3 Collaboration, P. Achard *et al.*, Eur. Phys. J. **C45**(2006) 569;
OPAL Collaboration, G. Abbiendi *et al.*, Eur. Phys. J. **C45**(2006) 307

[6] CDF Collaboration, D0 Collaboration and Tevatron Electroweak Working Group, V.M. Abazov *et al.*, Phys. Rev. **D70**(2004) 092008

[7] LEP Energy Working Group, R. Assmann *et al.*, Eur. Phys. J. **C39**(2005) 253

[8] ALEPH Collaboration, R. Barate *et al.*, Phys. Lett. **B464**(1999) 339;
L3 Collaboration, P. Achard *et al.*, Phys. Lett. **B585**(2004) 42;
OPAL Collaboration, G. Abbiendi *et al.*, Phys. Lett. **B604**(2004) 31

[9] DELPHI Collaboration, J. Abdallah *et al.*, Eur. Phys. J. **C46**(2006) 295

[10] DELPHI Collaboration, P. Aarnio *et al.*, Nucl. Instr. and Meth. **A303**(1991) 233
DELPHI Collaboration, P. Abreu *et al.*, Nucl. Instr. and Meth. **A378**(1996) 57

[11] The DELPHI Silicon Tracker Group, P. Chochula *et al.*, Nucl. Instr. and Meth. **A412**(1998) 304

[12] S. J. Alvsvaag *et al.*, Nucl. Instr. and Meth. **A425**(1999) 106

[13] A. Ballestrero, R. Chierici, F. Cossutti and E. Migliore, Comput. Phys. Commun. **152**(2003) 175

[14] E. Accomando and A. Ballestrero, Comput. Phys. Commun. **99**(1997) 270
E. Accomando, A. Ballestrero and E. Maina, Comput. Phys. Commun. **150**(2003) 166

[15] T. Sjöstrand *et al.*, Comput. Phys. Commun. **135**(2001) 238

[16] S. Jadach, Z. Was, R. Decker and J.H. Kuehn, Comput. Phys. Commun. **76**(1993) 361

[17] S. Jadach, W. Placzek, M. Skrzypek, B. F. L. Ward and Z. Was, Phys. Lett. **B417**(1998) 326;
S. Jadach, W. Placzek, M. Skrzypek, B. F. L. Ward and Z. Was, Comput. Phys. Commun. **140**(2001) 432

[18] E. Barberio and Z. Was, Comput. Phys. Commun. **79**(1994) 291

[19] L. Lönnblad, Comput. Phys. Commun. **71**(1992) 15

[20] G. Corcella *et al.*, JHEP **0101** (2001) 010

[21] DELPHI Collaboration, P. Abreu *et al.*, Zeit. Phys. **C73**(1996) 11

[22] S. Jadach, B. F. L. Ward and Z. Was, Comput. Phys. Commun. **130**(2000) 260

[23] T. Sjöstrand, *PYTHIA 5.7 and JETSET 7.4: Physics and manual*, CERN-TH-7112-93-REV (1995)

[24] Code kindly provided by J. Schwindling and B. Mansoulie

[25] P. Abreu *et al.*, Nucl. Instr. and Meth. **A427**(1999) 487

[26] G. Borisov, Nucl. Instr. and Meth. **A417**(1998) 384;
DELPHI Collaboration, P. Abreu *et al.*, Eur. Phys. J. **C10**(1999) 415

[27] S. Catani, Yu.L. Dokshitzer, M. Olsson, G. Turnock and B.R. Webber, Phys. Lett. **B269**(1991) 432;
N. Brown, W. Stirling, Zeit. Phys. **C53**(1992) 629

[28] Yu.L. Dokshitzer, G.D. Leder, S. Moretti, B.R. Webber, JHEP **9708** (1997) 001

[29] L. Lönnblad, Zeit. Phys. **C58**(1993) 471

[30] DELPHI Collaboration, J. Abdallah *et al.*, Eur. Phys. J. **C51**(2007) 249
[31] L3 Collaboration, P. Achard *et al.*, Phys. Lett. **B561**(2003) 202;
OPAL Collaboration, G. Abbiendi *et al.*, Eur. Phys. J. **C45**(2006) 291;
ALEPH Collaboration, S. Schael *et al.*, Eur. Phys. J. **C47**(2006) 309
[32] Particle Data Group, S. Eidelman *et al.* Phys. Lett. **B592**(2004) 1
[33] H. A. Bethe and W. Heitler, Proc. Roy. Soc. **A146**(1934) 83
[34] S. Jadach, W. Placzek, M. Skrzypek, B. F. L. Ward and Z. Was, Phys. Lett. **B523** (2001) 117
[35] F. Cossutti, Eur. Phys. J. **C44**(2005) 383
[36] A.P.Chapovsky and V.A.Khoze, Eur. Phys. J. **C9**(1999) 449
[37] A. Denner, S. Dittmaier, M. Roth and D. Wackeroth, Nucl. Phys. **B560**(1999) 33;
A. Denner, S. Dittmaier, M. Roth and D. Wackeroth, Nucl. Phys. **B587**(2000) 67
[38] F. Boudjema, B. Mele *et al.*, *Standard Model Process*, Physics at LEP2, eds. G. Altarelli, T. Sjöstrand and F. Zwirner, CERN 96-01 (1996) Vol. 1, 207
[39] DELPHI Collaboration, J. Abdallah *et al.*, Eur. Phys. J. **C34**(2004) 127
[40] DELPHI Collaboration, J. Abdallah *et al.*, Eur. Phys. J. **C44**(2005) 161
[41] ALEPH Collaboration, S. Schael *et al.*, Phys. Lett. **B606**(2005) 265;
OPAL Collaboration, G. Abbiendi *et al.*, Eur. Phys. J. **C36**(2004) 297;
L3 Collaboration, P. Achard *et al.*, Phys. Lett. **B547**(2002) 139
[42] L. Lönnblad and T. Sjöstrand, Eur. Phys. J. **C2**(1998) 165
[43] V. Khoze *et al.*, *Colour Reconnection*, Physics at LEP2, eds. G. Altarelli, T. Sjöstrand and F. Zwirner, CERN 96-01 (1996) Vol.1, 191
[44] T. Sjöstrand and V. Khoze, Zeit. Phys. **C62**(1994) 281;
T. Sjöstrand and V. Khoze, Phys. Rev. Lett. **72**(1994) 28
[45] G. Gustafson and J. Häkkinen, Zeit. Phys. **C64**(1994) 659
[46] L. Lönnblad, Zeit. Phys. **C70**(1996) 107
[47] L. Lyons, D. Gibaut and P. Clifford, Nucl. Instr. and Meth. **A270**(1988) 110
[48] *LEP2 Monte Carlo Workshop : Report of the Working Groups on Precision Calculations for LEP2 Physics* eds. G. Passarino, R. Pittau, S. Jadach, CERN-2000-009 (2000)

Year	Energy	Channel	M_W GeV/c^2
1996	172	$e\overline{\nu}_e q\bar{q}'$	80.450 ± 0.870(Stat.) ± 0.085(Syst.) ± 0.013(LEP)
1996	172	$\mu\overline{\nu}_\mu q\bar{q}'$	80.560 ± 0.760(Stat.) ± 0.062(Syst.) ± 0.013(LEP)
1996	172	$\ell\overline{\nu}_\ell q\bar{q}'$	80.510 ± 0.570(Stat.) ± 0.051(Syst.) ± 0.013(LEP)
1997	183	$e\overline{\nu}_e q\bar{q}'$	80.852 ± 0.411(Stat.) ± 0.034(Syst.) ± 0.009(LEP)
		$\mu\overline{\nu}_\mu q\bar{q}'$	80.573 ± 0.331(Stat.) ± 0.024(Syst.) ± 0.009(LEP)
		$\tau\overline{\nu}_\tau q\bar{q}'$	80.233 ± 0.396(Stat.) ± 0.025(Syst.) ± 0.009(LEP)
		$\ell\overline{\nu}_\ell q\bar{q}'$	80.548 ± 0.216(Stat.) ± 0.024(Syst.) ± 0.009(LEP)
1998	189	$e\overline{\nu}_e q\bar{q}'$	79.848 ± 0.275(Stat.) ± 0.035(Syst.) ± 0.009(LEP)
1998		$\mu\overline{\nu}_\mu q\bar{q}'$	80.238 ± 0.195(Stat.) ± 0.026(Syst.) ± 0.009(LEP)
1998		$\tau\overline{\nu}_\tau q\bar{q}'$	80.055 ± 0.288(Stat.) ± 0.030(Syst.) ± 0.009(LEP)
1998		$\ell\overline{\nu}_\ell q\bar{q}'$	80.096 ± 0.139(Stat.) ± 0.026(Syst.) ± 0.009(LEP)
1999	192	$e\overline{\nu}_e q\bar{q}'$	80.025 ± 0.789(Stat.) ± 0.036(Syst.) ± 0.009(LEP)
		$\mu\overline{\nu}_\mu q\bar{q}'$	80.604 ± 0.467(Stat.) ± 0.028(Syst.) ± 0.009(LEP)
		$\tau\overline{\nu}_\tau q\bar{q}'$	80.161 ± 0.664(Stat.) ± 0.033(Syst.) ± 0.009(LEP)
	196	$e\overline{\nu}_e q\bar{q}'$	80.391 ± 0.349(Stat.) ± 0.037(Syst.) ± 0.010(LEP)
		$\mu\overline{\nu}_\mu q\bar{q}'$	80.024 ± 0.270(Stat.) ± 0.031(Syst.) ± 0.010(LEP)
		$\tau\overline{\nu}_\tau q\bar{q}'$	80.269 ± 0.417(Stat.) ± 0.036(Syst.) ± 0.010(LEP)
	200	$e\overline{\nu}_e q\bar{q}'$	80.383 ± 0.365(Stat.) ± 0.037(Syst.) ± 0.010(LEP)
		$\mu\overline{\nu}_\mu q\bar{q}'$	80.374 ± 0.282(Stat.) ± 0.032(Syst.) ± 0.010(LEP)
		$\tau\overline{\nu}_\tau q\bar{q}'$	80.197 ± 0.438(Stat.) ± 0.040(Syst.) ± 0.010(LEP)
	202	$e\overline{\nu}_e q\bar{q}'$	80.193 ± 0.453(Stat.) ± 0.039(Syst.) ± 0.010(LEP)
		$\mu\overline{\nu}_\mu q\bar{q}'$	80.120 ± 0.341(Stat.) ± 0.033(Syst.) ± 0.010(LEP)
		$\tau\overline{\nu}_\tau q\bar{q}'$	81.399 ± 0.574(Stat.) ± 0.042(Syst.) ± 0.010(LEP)
	192-202	$\ell\overline{\nu}_\ell q\bar{q}'$	80.296 ± 0.113(Stat.) ± 0.030(Syst.) ± 0.009(LEP)
2000	206	$e\overline{\nu}_e q\bar{q}'$	80.814 ± 0.267(Stat.) ± 0.040(Syst.) ± 0.016(LEP)
		$\mu\overline{\nu}_\mu q\bar{q}'$	80.340 ± 0.193(Stat.) ± 0.032(Syst.) ± 0.016(LEP)
		$\tau\overline{\nu}_\tau q\bar{q}'$	80.701 ± 0.272(Stat.) ± 0.042(Syst.) ± 0.016(LEP)
		$\ell\overline{\nu}_\ell q\bar{q}'$	80.551 ± 0.136(Stat.) ± 0.034(Syst.) ± 0.016(LEP)

Table 17: Measured W mass (in GeV/c^2) from the semi-leptonic decay channel analyses with the nominal centre-of-mass energies (in GeV) of each data sample indicated. The values marked $\ell\overline{\nu}_\ell q\bar{q}'$ are the combined values of the three semi-leptonic channel analyses. The values obtained from the data recorded in 1996 and analysed in [2] are also included.

Year	Energy	Analysis	M_W GeV/c^2
1996	172	std	79.900 ± 0.590(Stat.) ± 0.050(Syst.) ± 0.214(FSI) ± 0.013(LEP)
1997	183	std	80.137 ± 0.185(Stat.) ± 0.046(Syst.) ± 0.214(FSI) ± 0.009(LEP)
		cone	80.100 ± 0.191(Stat.) ± 0.046(Syst.) ± 0.119(FSI) ± 0.009(LEP)
1998	189	std	80.519 ± 0.107(Stat.) ± 0.032(Syst.) ± 0.214(FSI) ± 0.009(LEP)
		cone	80.533 ± 0.119(Stat.) ± 0.032(Syst.) ± 0.119(FSI) ± 0.009(LEP)
1999	192	std	80.711 ± 0.281(Stat.) ± 0.032(Syst.) ± 0.214(FSI) ± 0.009(LEP)
		cone	81.076 ± 0.294(Stat.) ± 0.032(Syst.) ± 0.119(FSI) ± 0.009(LEP)
	196	std	80.248 ± 0.159(Stat.) ± 0.032(Syst.) ± 0.214(FSI) ± 0.010(LEP)
		cone	80.240 ± 0.192(Stat.) ± 0.032(Syst.) ± 0.119(FSI) ± 0.010(LEP)
	200	std	80.274 ± 0.149(Stat.) ± 0.032(Syst.) ± 0.214(FSI) ± 0.010(LEP)
		cone	80.227 ± 0.164(Stat.) ± 0.032(Syst.) ± 0.119(FSI) ± 0.010(LEP)
	202	std	80.537 ± 0.199(Stat.) ± 0.031(Syst.) ± 0.214(FSI) ± 0.010(LEP)
		cone	80.248 ± 0.231(Stat.) ± 0.031(Syst.) ± 0.119(FSI) ± 0.010(LEP)
	192-202	std	80.365 ± 0.090(Stat.) ± 0.032(Syst.) ± 0.214(FSI) ± 0.010(LEP)
		cone	80.339 ± 0.103(Stat.) ± 0.032(Syst.) ± 0.119(FSI) ± 0.010(LEP)
2000	206	std	80.318 ± 0.092(Stat.) ± 0.032(Syst.) ± 0.214(FSI) ± 0.015(LEP)
		cone	80.171 ± 0.104(Stat.) ± 0.032(Syst.) ± 0.119(FSI) ± 0.015(LEP)

Table 18: Measured W mass (in GeV/c^2) from the fully-hadronic decay channel analysis with the nominal centre-of-mass energies (in GeV) of each data sample indicated. Results are provided for both the standard (std) and cone jet reconstruction techniques applied. The value obtained from the data recorded in 1996 and analysed in [2] is also included.

	$\ell\overline{\nu}_\ell q\bar{q}'$	$q\bar{q}'\bar{q}q'$	All
Value	80.339	80.311	80.336
Statistical Error	.069	.059	.055
Statistical Error on Calibration	.003	.004	.002
Lepton Corrections	.015	-	.012
Jet Corrections	.020	.026	.021
Fragmentation	.011	.012	.011
Background	.007	.013	.006
Threshold Systematics	-	-	.002
Electroweak Corrections	.006	.005	.006
LEP Energy	.009	.010	.009
Bose-Einstein Correlations	-	.026	.005
Colour Reconnection	-	.116	.024

Table 19: The final results (in GeV/c^2) of the W mass analyses and the breakdown of the uncertainty into its component categories. The $\ell\overline{\nu}_\ell q\bar{q}'$ and $q\bar{q}'\bar{q}q'$ results use the values obtained in these analysis channels from the direct reconstruction method. The column marked 'All' uses the full direct reconstruction analyses and the threshold cross-section measurement. The $q\bar{q}'\bar{q}q'$ results are taken from the cone jet reconstruction analysis, for all data except 1996 where the standard analysis was used.

CR MeV/c^2	$\kappa_{\texttt{SK-I}}$	M_W GeV/c^2
0	0.00	80.326 ± 0.045(Stat.) ± 0.028(Syst.) ± 0.013(FSI) ± 0.010(LEP)
20	0.40	80.326 ± 0.045(Stat.) ± 0.028(Syst.) ± 0.016(FSI) ± 0.010(LEP)
40	0.89	80.328 ± 0.046(Stat.) ± 0.028(Syst.) ± 0.021(FSI) ± 0.010(LEP)
60	1.51	80.330 ± 0.048(Stat.) ± 0.028(Syst.) ± 0.024(FSI) ± 0.010(LEP)
80	2.30	80.333 ± 0.051(Stat.) ± 0.028(Syst.) ± 0.026(FSI) ± 0.010(LEP)
100	3.36	80.335 ± 0.054(Stat.) ± 0.028(Syst.) ± 0.026(FSI) ± 0.009(LEP)

Table 20: The combined DELPHI W Mass value as a function of the uncertainty ascribed to colour reconnection effects in the fully-hadronic decay channel. The values of the $\kappa_{\texttt{SK-I}}$ parameter that give rise to this shift in the $q\bar{q}'\bar{q}q'$ W mass at a centre-of-mass energy of 200 GeV are also given.

Year	Energy	Channel	Γ_W GeV/c^2
1997	183	$\ell\overline{\nu}_\ell q\bar{q}'$	2.495 ± 0.590(Stat.) ± 0.069(Syst.)
		$q\bar{q}'\bar{q}q'$	2.572 ± 0.460(Stat.) ± 0.092(Syst.) ± 0.248(FSI)
1998	189	$\ell\overline{\nu}_\ell q\bar{q}'$	3.056 ± 0.401(Stat.) ± 0.071(Syst.)
		$q\bar{q}'\bar{q}q'$	2.337 ± 0.260(Stat.) ± 0.114(Syst.) ± 0.248(FSI)
1999	192	$\ell\overline{\nu}_\ell q\bar{q}'$	2.342 ± 0.953(Stat.) ± 0.071(Syst.)
		$q\bar{q}'\bar{q}q'$	2.390 ± 0.756(Stat.) ± 0.126(Syst.) ± 0.248(FSI)
	196	$\ell\overline{\nu}_\ell q\bar{q}'$	1.805 ± 0.440(Stat.) ± 0.072(Syst.)
		$q\bar{q}'\bar{q}q'$	2.545 ± 0.508(Stat.) ± 0.142(Syst.) ± 0.248(FSI)
	200	$\ell\overline{\nu}_\ell q\bar{q}'$	2.153 ± 0.477(Stat.) ± 0.073(Syst.)
		$q\bar{q}'\bar{q}q'$	2.210 ± 0.376(Stat.) ± 0.157(Syst.) ± 0.248(FSI)
	202	$\ell\overline{\nu}_\ell q\bar{q}'$	1.707 ± 0.649(Stat.) ± 0.076(Syst.)
		$q\bar{q}'\bar{q}q'$	1.797 ± 0.488(Stat.) ± 0.165(Syst.) ± 0.248(FSI)
	192-202	$\ell\overline{\nu}_\ell q\bar{q}'$	1.950 ± 0.277(Stat.) ± 0.072(Syst.)
		$q\bar{q}'\bar{q}q'$	2.210 ± 0.243(Stat.) ± 0.152(Syst.) ± 0.248(FSI)
2000	206	$\ell\overline{\nu}_\ell q\bar{q}'$	2.814 ± 0.364(Stat.) ± 0.083(Syst.)
		$q\bar{q}'\bar{q}q'$	1.979 ± 0.225(Stat.) ± 0.183(Syst.) ± 0.248(FSI)

Table 21: Measured W widths (in GeV/c^2) from the semi-leptonic decay and fully-hadronic decay channel analyses with the nominal centre-of-mass energies (in GeV) of each data sample indicated.

	$\ell\overline{\nu}_\ell \mathrm{q}\bar{\mathrm{q}}'$	$\mathrm{q}\bar{\mathrm{q}}'\bar{\mathrm{q}}\mathrm{q}'$	All
Value	2.452	2.237	2.404
Statistical Error	.184	.137	.140
Statistical Error on Calibration	.006	.009	.005
Lepton Corrections	.041	-	.030
Jet Corrections	.036	.129	.059
Fragmentation	.029	.008	.024
Electroweak Corrections	.011	.009	.010
Background	.037	.051	.031
Bose-Einstein Correlations	-	.020	.005
Colour Reconnection	-	.247	.065

Table 22: The final results (in GeV/c^2) of the W width analyses and the breakdown of the uncertainty into its component categories. The $\ell\overline{\nu}_\ell \mathrm{q}\bar{\mathrm{q}}'$ and $\mathrm{q}\bar{\mathrm{q}}'\bar{\mathrm{q}}\mathrm{q}'$ results use the values obtained in these analysis channels from the direct reconstruction method. The column marked 'All' provides the result from combining the measurements made in both channels.